Università degli Studi di Padova

Dipartimento di Astronomia

SCUOLA DI DOTTORATO DI RICERCA IN ASTRONOMIA
XXIII ciclo
Sede amministrativa: Università degli Studi di Padova

Study of the Exospheres of the Solar System Bodies

Supervisore: Ch.mo Prof. Cesare Barbieri
Co-Supervisore: Prof. Nicholas M. Schneider
(University of Colorado)
Direttore della Scuola: Ch.mo Prof. Giampaolo Piotto

DOTTORANDO: Cesare Grava

July 28, 2011

Ad Amarilli

Abstract (italiano)

L'esosfera è quella parte di un'atmosfera planetaria (o anche stellare) caratterizzata da una bassa pressione, per cui il libero cammino medio delle particelle è maggiore o comparabile all'altezza di scala. Atomi e molecole con sufficiente energia da vincere l'attrazione gravitazionale fuggono nello spazio interplanetario e sono perduti dall'atmosfera. Particelle quindi si muovono su orbite balistiche, senza collidere tra di loro. Per questa ragione, varie specie presenti nell'esosfera non interagiscono tra di loro, ed è possibile scegliere un elemento come tracciante per studiare la dinamica dell'intera atmosfera. Ecco perché, per osservatori al suolo, la scelta naturale è il sodio, perché è l'elemento più facilmente rilevabile grazie alla sua alta sezione d'urto per *resonant scattering* della luce solare, per di più in una regione dove l'assorbimento tellurico non disturba molto.

Le esosfere (o corone, come sono spesso chiamate) si trovano quasi dappertutto nel Sistema Solare, visto che sono state scoperte in tutti i pianeti e in quasi tutti i satelliti maggiori. Anzi, esse sono state scoperte pure negli esopianeti. Esse sono regioni di confine tra l'ambiente planetario (sia esso la superficie, come Mercurio, o un'atmosfera collisionalmente spessa, come Io e la Terra, o ancora crosta di ghiaccio su Europa) e lo spazio interplanetario, che è rappresentato dal campo magnetico intrinseco laddove è presente (Mercurio e Terra), dal vento solare (Lutetia), o ancora la magnetosfera del primario (Io e la Luna). Per queste ragioni, le esosfere sono elementi chiave nella comprensione dell'evoluzione e formazione planetaria, e non stupisce che siano oggetto di studi approfonditi da parte di sonde spaziali e osservatori, come pure di teorici.

Io ho dedicato i tre anni di dottorato allo studio di differenti tipi di esosfere, con approcci differenti. Dopo un'introduzione alla teoria delle atmosfere planetarie (capitolo 1), necessaria per capire l'argomento trattato da questa tesi, dedicherò la maggior parte della mia tesi di dottorato alla corona di Io (capitolo 2). Il mio lavoro è stato quello di testare l'affascinante ipotesi che essa condensi durante le eclissi da parte di Giove. Lo scopo finale è di controllare il ruolo che l'esosfera gioca nel rifornimento e nel trasporto di atomi dalla superficie alla nube neutra più estesa. Le osservazioni sono state condotte al telescopio TNG, con lo spettrografo ad alta risoluzione SARG. I risultati preliminari sono stati pubblicati in Grava et al.

(2010), mentre quelli definitivi vengono riportati in sezione 2.8. Essi scartano l'ipotesi che la condensazione non avvenga durante le eclissi, e questo significa the le molecole contenenti sodio sono "intrappolate" in superficie dall'atmosfera condensata durante l'eclisse e nelle ore immediatamente successive all'egresso, finché la sublimazione non riporta l'atmosfera alla sua condizione precedente l'eclisse. Questa è la prima evidenza osservativa di questo fenomeno. Durante questo lavoro, nuovi, inaspettati risultati (sezione 2.9) sono stati scoperti negli spettri prima dell'eclisse. Si tratta di assorbimento e di emissione di sodio rispettivamente dal disco e dalle nubi estese, e si trovano a Doppler shift leggermente diversi. Ciò sembra mettere in evidenza una qualche carenza nella nostra comprensione sui meccanismi di interazione tra il toro di plasma iogenico e la magnetosfera gioviana, e nuovi modelli dovranno essere sviluppati.

Il capitolo 3 è dedicato al pianeta Mercurio, sul quale ho lavorato in due diversi approcci. Da un lato, infatti, ho contribuito alla riduzione dei dati che sono stati pubblicati in Mangano et al. (2009). Un riassunto dei risultati è riportata in sezione 3.9. Abbiamo mostrato che un cambiamento nel campo magnetico interplanetario ha prodotto un aumento nel flusso di ioni che impattano sulla superficie attraverso le "cuspidi magnetosferiche", portando ad un aumento di emissione di atomi attraverso *ion sputtering* e quindi ad un aumento della luminosità del sodio nell'emisfero meridionale.

Dall'altro lato, ho iniziato un modello della coda di sodio di Mercurio in direzione anti-solare (sezione 3.8), visto che gli unici modelli esistenti sono stati sviluppati prima della conferma osservativa, quasi 10 anni fa. Obiettivo è predire, per una data geometria osservativa, l'intensità della coda anti-solare, in modo da avere uno strumento per interpretare le osservazioni. Il modello necessita tuttora di miglioramenti, specialmente riguardo il passaggio da densità numerica a densità di colonna (sezione 3.9). Tuttavia, esso ha mostrato un trend soddisfacente con la densità di colonna osservata, e la conferma che a contribuire di più all'emission di atomi nella coda anti-solare è il processo di *ion sputtering*.

L'ultima parte di questa tesi (capitolo 4) è dedicata ad altri corpi sui quali ho lavorato parzialmente, e cioè Lutetia, Europa e la Luna. La Luna e l'asteoride di fascia principale Lutetia sono stati entrambi visitati recentemente da *fly-by* della sonda Rosetta, nel suo viaggio verso la cometa 67P/Churyumov-Gerasimenko. La camera OSIRIS-WAC a bordo di Rosetta ha un filtro al sodio che permette di studiare l'esosfera di questi corpi. La Luna ha la sua, ben conosciuta, esosfera, e i tre *fly-by* del sistema Terra-Luna offrirono un'irresistibile opportunità per studiare la coda di sodio della Luna in direzione anti-solare. Invece, prima del *fly-by* dell'asteroide Lutetia, ben poco era noto di questo corpo, e io ho creato un modello (sezione 4.1.2) che per la prima volta riproduce la luminosità prevista della sua esosfera. Purtroppo, gravi problemi dovuti a *ghost* e luce diffusa, specialmente

nel filtro del sodio (sezione 4.3.1), hanno impedito ogni tentativo di calibrare le immagini.

Ho infine lavorato a dati acquisiti con TNG-SARG su Europa, la seconda luna di Giove. Queste osservazioni seguirono quelle che hanno rilevato gli inaspettati risultati su Io, e i dati sono stati acquisiti con una modalità non standard, vale a dire senza il filtro del sodio, che impedisce la sovrapposizione degli ordini. Ciò ha però permesso di sfruttare tutte le possibili lunghezze d'onda dello spettrografo, e quindi si studiare più specie. I passi di riduzione sono perciò molto più complessi, quindi sono stati appena completati. I risultati preliminari (Schneider et al. 2010 e sezione 4.2.2) hanno permesso: di misurare il rapporto Na/K su Europa, suggerendo fortemente che il sodio è endogenico piuttosto che portato su Europa da Io e successivamente ri-emesso; di osservare variazioni di luminosità del sodio fino a 5 volte lungo l'orbita ("stagioni"); di rilevare un'emissione all'esatta posizione prevista per la transizione (proibita) dell'ossigeno atomico allo spostamento Doppler di Io. Se confermata, si tratterà della prima rilevazione di ossigeno atomico sia sul disco che nelle nubi esterne.

Abstract (english)

The exosphere is that part of a planetary (or even stellar) atmosphere characterized by a low pressure such that the mean free path of the particles is greater or comparable to the scale height. Atoms and molecules with enough energy to overcome the gravitational attraction of the body escape in the interplanetary space and are lost from the atmosphere. Particles thus move on ballistic orbits, without colliding with each other. For this reason, various species present in the exosphere don't interact with each other, and thus it is possible to choose one element as a tracer to study the dynamics of the whole atmosphere. That's why, for ground-based observers, the natural choice is sodium, because it is the most easily detectable element thanks to its high resonant scattering cross section of sunlight, moreover in a region where telluric absorption doesn't disturb too much.

Exospheres (or corona, as they are often called) are nearly ubiquiotus in the Solar System, having been discovered in all planets and in most of the major satellites. Indeed, they have been discovered also in exoplanets. They are border regions between planetary environment (being it the surface, as Mercury, or a collisonally thick atmosphere, as Io and the Earth, or again water-ice crust on Europa) and the interplanetary space, which is represented by the intrinsic magnetic field where present (i.e. Mercury and Earth), the solar wind (Lutetia), or again the magnetosphere of the primary body (Io and the Moon). For this reasons, exospheres are key elements in the comprehension of planetary evolution and formation, and it is not surprising that they are topics thoroughly studied by spacecrafts and observatories, as well as theoricists.

I have dedicated the three years of my PhD in the study of different kind of exospheres, with different approaches. After an introduction at the theory of planetary atmospheres (chapter 1), necessary to understand the topic this thesis concerns, I will dedicate most part of my PhD thesis to the corona of Io (chapter 2). My work has been the test of the fascinating hypothesis that it condense during elipses behind Jupiter. The final aim is to check the role that the exosphere plays in the supply and transport of atom from the surface to the more extended neutral cloud. Observations have been carried on at TNG telescope, equipped with the high-resolution spectrograph SARG. Preliminary results have been published in

Grava et al. (2010), while those definitive are reported in section 2.8). They discard the null hypothesis that condensation does not occur during eclipses, and this means that sodium-bearing molecules are "trapped" at surface by the condensed exosphere during eclipse and in the hours immediately after the reappearance, until the sublimation brings the atmosphere back to the pre-eclipse condition. This is the first observational evidence of such a result. During this work, new, unexpected features (section 2.9) have been discovered in the pre-eclipse spectra. They are absorption and emission of sodium respectively from the disk and from the extendend clouds, at slightly different Doppler shifts. This seems to suggest some lack in our understanding on the interaction mechanisms between iogenic plasma torus and giovian magnetosphere, and new models will have to be developed.

Chapter 3 is dedicated to the planet Mercury, on which I've worked in a double approach. On one side, I have contributed to the reduction of data that have been published in Mangano et al. (2009). A summary of the results is reported in section 3.9. We showed that a change in the interplanetary magnetic field produced an enhancement in the ion flux impinging the surface through the magnetospheric cusps, leading to an increase of emission of atoms by ion sputtering and thus to a southern enhancement of sodium brightness.

On the other side, I have started a modelization of the anti-sunward sodium tail of Mercury (section 3.8) , since the only models that have been developed so far predate the observational confirmation. The purpose is to predict, for a given observational geometry, the brightness of the anti-sunward tail, to have a tool to compare the observation with. The section The model needs still some improvements especially concerning the conversion from number density to projected column density (section 3.9). However, it showed a satisfactory trend with the observed column densities, and the confirmation that the process that most contributes to sodium atoms in the anti-sunward tail is ion sputtering.

The last part of this thesis (chapter 4) is dedicated to other bodies over which I worked partially, namely Lutetia, Europa and the Moon. The Moon and he Main Belt Asteroid Lutetia have both been visited recently by fly-bys of the Rosetta spacecraft on its journey to the comet 67P/Churyumov-Gerasimenko. The Osiris-WAC camera on board of Rosetta has a sodium filter that allows the study of exospheres of such bodies. Moon has its own, well known exosphere, and the three fly-bys of Earth-Moon system offered a compelling opportunity to study the anti-sunward sodium tail of the Moon. Before the flyby of asteroid Lutetia, instead, little was known about this body, and I created a model (section 4.1.2) that for the first time reproduces the expected brightness of its sodium exosphere. Unfortunately, severe problems due to ghosts and diffuse straylight, especially on the sodium filter (section 4.3.1), prevented any attempt to calibrate the images.

I've also worked on the data aquired with TNG-SARG of Jupiter's second moon

Europa. This observing run followed the one that detected the unexpected features of Io, and data were aquired in a non-standard mode, that is without sodium filter, that helps avoiding order overlapping. Nevertheless, this allowed us to exploit all possible wavelength of the spectrograph, and thus to study more species. Reduction steps are thus more complex, and they have been just completed. Preliminary results (Schneider et al. 2010 and section 4.2.2) allowed us: to measure the Na/K ratio at Europa, strongly suggesting that sodium is endogenic rather that brougth to Europa from Io and then subsequently re-emitted; to observe variations in sodium brightness of up to a factor 5 along the orbit ("seasons"); to detect an emission at the exact position of the forbidden atomic oxygen line at the Doppler shift of Io. If confirmed, this is the first detection of this element both at the disk and in the neutral clouds.

Contents

List of Figures

List of Tables

1

Planetary Atmospheres

Planetary atmospheres are nearly ubiquitous in the Solar System, having been discovered in all planets and in most of the major satellites. Nevertheless, they diplay gross differences between them. Some are extremly dense, and gradually blend into fluid envelopes that constitute the whole planet (gaseous giants) or lie at direct contact with the surface (Venus), while others are billions of times thinner than the one at Earth. Also, the composition of atmospheres varies substantially, going from the solar-like H/He envelopes of the giant planets to atmospheres dominated by nitrogen carbon dioxide, or sulfur dioxide. Anyway, all atmospheres are governed by the same processes. For example, clouds form on most of the atmospheres, gradients in temperature and pressure leads to winds, and photochemistry depending on components and on solar irradiation modifies the upper layer of an atmosphere. Here I will revise briefly what is essential to know about atmospheres in order to understand the topics involved in this thesis.

1.1 Density and Scale Height

The relationship between T, pressure P and density ρ in a planetary atmosphere is governed by a balance between gravity and pressure: the **hydrostatic equilibrium**. This means that:

$$\frac{dP}{dz} = -g_p(z)\rho(z) \tag{1.1}$$

where g_p is the gravitational acceleration and z the height. The **ideal gas law** is:

$$P = NkT = \frac{\rho R_{gas} T}{\mu_a} = \frac{\rho k T}{\mu_a m_{amu}} \tag{1.2}$$

where N is the particle number density, μ the mean molecular mass (in atomic mass units), R_{gas} the universal gas constant ($R_{gas} = N_A k$, where N_A is the Avogadro's

number and k the Boltzmann constant) and $m_{amu} \approx 1.67 \times 10^{24}\ g$ is the atomic mass unit, which is slightly less than the mass of a hydrogen atom. Combining these two formula results in the **barometric law**:

$$P(z) = P(0) \exp\left(- \int_0^z dr/H(r) \right) \tag{1.3}$$

where $P(0)$ is the pressure at altitude $z = 0$. The **pressure scale height** is defined as:

$$H(z) = \frac{kT(z)}{g_p(z)\mu_a(z)m_{amu}} \tag{1.4}$$

Thus H is equal to the distance above which the pressure decreases by a factor e. Small values of H implies a rapid decrease of atmospheric pressure with altitude. Alternatively, the barometric law can be written as follows:

$$\rho(z) = \rho(0) \exp\left(- \int_0^z dr/H^*(r) \right) \tag{1.5}$$

where the **density scale height** H^* is defined as:

$$\frac{1}{H^*(z)} = \frac{1}{T(z)} \frac{dT(z)}{dz} + \frac{g_p(z)\mu_a(z)m_{amu}}{kT(z)} \tag{1.6}$$

Note that in an isothermal region of an atmosphere, $H^*(z) = H(z)$. H is of the order of $\sim 10 \div 25 km$ for most planets, while it is far larger for Mercury ($\lesssim 100 km$).

Eq. 1.5 reveals that density decreases with altitude. An altitude is thus reached above which particles can travel planetary scale distances with a very small probability of making a collison. At such altitudes atoms or molecules that have energies greater than their gravitational binding energy can escape to space provided that their radial velocity is outward. This region of the atmosphere is called the **exosphere**, or corona. Its lower boundary, the **exobase**, is the altitude at which the mean free path is comparable to or greater than the atmospheric scale height. The **Knudsen number**, K_n, is the ratio between the mean free path l and the density scale height. It defines a transition region where a gas that is dominated by collisions and behaves like a fluid becomes a gas that has to been modeled stochastically. Therefore, an alternative definition of the exobase is that altitude at which $K_n \sim 1$. In a gas of randomly moving molecules the mean free path for collisions is

$$l_c \approx 1/(\sqrt{2}\sigma n) \tag{1.7}$$

where n is the molecular number density and σ is the hard sphere cross section which is independent of energy and assumes isotropic scattering. Therefore, from the definition of exobase,

$$\sigma_x n_{exo} H \sim 1 \tag{1.8}$$

The exobase occurs at a column density $N(r_{exo}) \sim [n_{exo}H] \sim 1/\sigma$, where r_{exo} is the exobase radius. $\sigma \sim 1 \div 3 \times 10^{-15}\ cm^2$ if often used (Chamberlain & Hunten 1987).

For a gas in a thermal equilibrium, the velocities follow a Maxwellian distribution function:

$$f(v)dv = N\left(\frac{2}{\pi}\right)^{1/2}\left(\frac{m}{kT}\right)^{3/2} v^2 \exp(-mv^2/(2kT))dv \tag{1.9}$$

with v the particle velocity, m its mass, and N is the local particle (number) density. Below the exobase, collisions between particles drive the velocity distribution into a Maxwellian distribution. Above the exobase, collisions are essentially absent and particles in the tail of the distribution which have $v > v_{esc}$ may escape into space. A Maxwellian distribution formally extends up to infinite velocities, but due to the steep dropoff in the Gaussian distribution, there are practically no particles with velocities larger than about 4 times the mean (or **most probable**) thermal speed:

$$v_{mp} = \sqrt{2kT/m} \tag{1.10}$$

The transition between a collision dominated ($K_n \ll 1$) to the quasi-collisionless exosphere ($K_n > 1$) is gradual, not abrupt. For example, at Titan the "exobase region" may be $\sim 1000\ km$ thick as the atmosphere transitions from N_2 to H_2 domination (Johnson et al. 2008). I will return to the escape from planetary exospheres in section 1.5.

1.2 Thermal Structure

The thermal structure of an atmosphere, dT/dz, is governed by the efficiency of energy transport. This process depends largely on the **optical depth** of the atmosphere, defined as:

$$\tau_\nu \equiv \int_{z_1}^{z_2} \alpha_\nu(z)\rho(z)dz. \tag{1.11}$$

Here $\rho(z)$ is the density and α_ν is the extinction coefficient: $\alpha_\nu = \kappa_\nu + \sigma_\nu$, where κ_ν and σ_ν are the mass absorption and the mass scattering coefficients, respectively. The optical depth is determined by a variety of physical and chemical processes: irradiation by the Sun of the topmost layer of atmosphere; energy from internal heat sources (the giant planets) and reradiation of adsorbed sunlight by a planet's surface or dust; chemical reactions, which change composition, which in turn changes opacity and hence thermal structure; clouds and/or photochemically produced haze layers, which change opacity and temperature via release

(cloud formation) or absorption (evaporation) of latent heat; volcanoes and geysers; chemical interaction between atmosphere and crust or ocean; biochemical and anthropogenic processes (on Earth). The temperature structure of planetary atmospheres is qualitatively similar to that reported for the Earth - see fig. 1.1. Moving upwards from the surface, or, for giant planets, from deep atmosphere, temperature decreases with altitude: this is the *troposphere*. Here condensable gases, usually trace elements, form clouds. The temperature typically reaches a minimum at the tropopause, near pressure level of 0.1 bar. Above this level, the structure is inverted: it is the *stratosphere*. At higher altitudes there is the *mesosphere*, characterized by a negative temperature gradient increasing altitude. Above the mesosphere, there is the *thermosphere*, whose T increases with altitude, up to the *exosphere*, which is the outermost part of an atmosphere.

1.3 Source and Transport of Energy

Unlike stellar atmospheres, which are heated from below, and are so hot that the elements are primarily in atomic form, planetary atmospheres consist of molecular gases and are in part heated from the top through solar irradiation. This acts through absorption of solar photons which heat up upper atmosphere (through Extreme Ultra Violet photons, $10 \div 100\, nm$) or even planetary surface, or layers in the atmosphere where optical depth is moderately large (for photons in the visible wavelength). Upper atmospheres can also be heated by charged particle precipitation (in the auroral zones) and by Joule heating, resulting from electric currents in the ionosphere. Atmospheres can be heated also from below, through re-radiation of sunlight by planetary surface, which occurs primarily in IR, or by energy transport from deeper layers.

The temperature structure in an atmosphere is governed by efficiency of **energy transport**. There are 3 principal mechanisms to transport energy: conduction, radiation and convection. Usually, one of these dominates and determine the thermal profile in a given region, although but in general in a planetary atmosphere we typically encounter all 3 mechanisms. The dominance of a mechanism over the others is determined by the atmospheric temperature gradient, $\mid dT/dz \mid$.

Conduction is important in the very upper part of the thermosphere and in the exosphere, and very near the surface where it exists. Collisions tend to equalize the temperature distribution, resulting in a nearly isothermal profile in the exosphere. **Convection**, the transport of energy through transport of matter, is usually important in the troposphere, and the temperature profile is close to an adiabat. The dry adiabatic lapse rate is:

$$\frac{dT}{dz} = -\frac{g_p}{c_p} = -\frac{\gamma - 1}{\gamma}\frac{g_p \mu_a m_{amu}}{k} \tag{1.12}$$

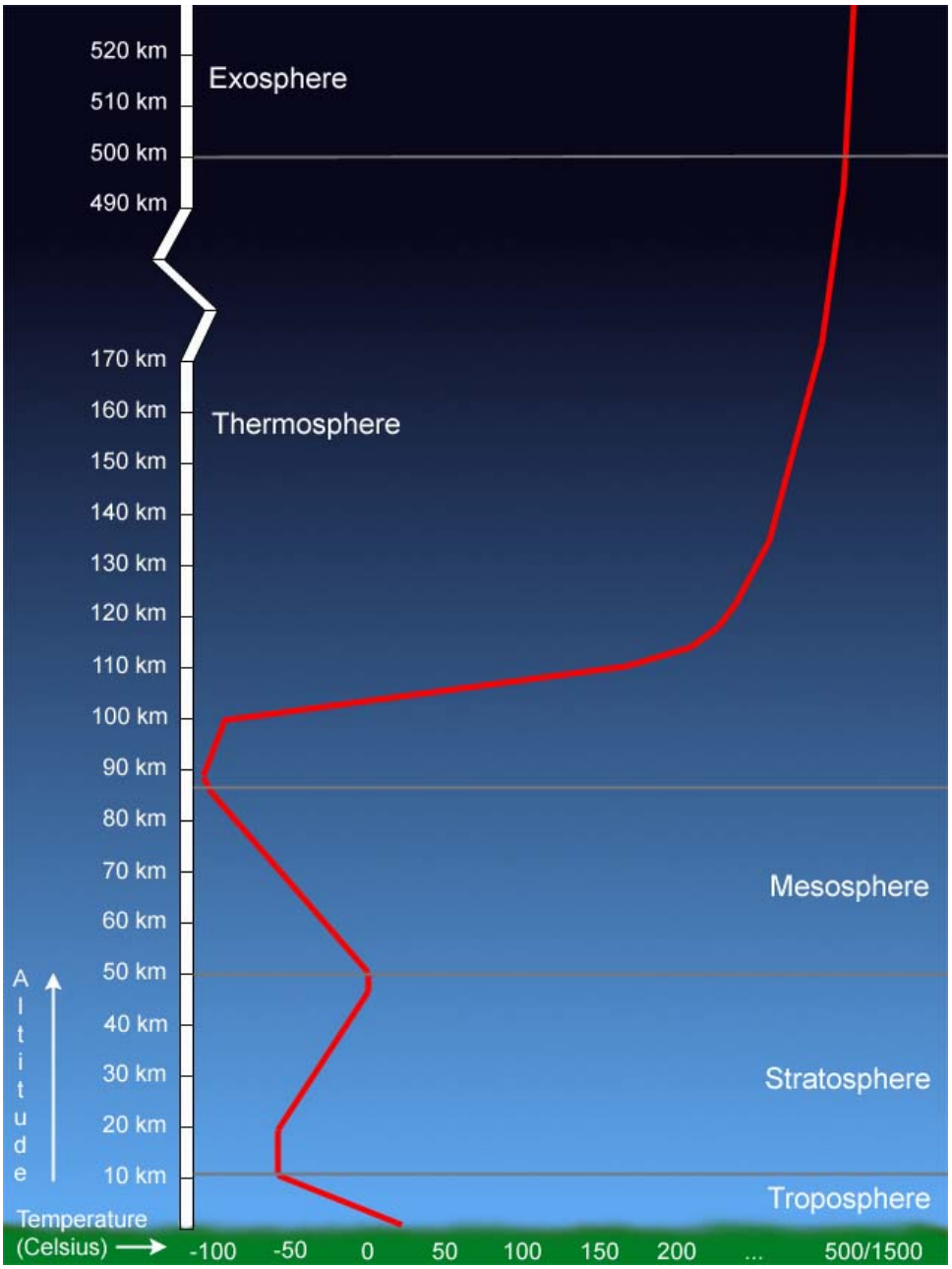

Figure 1.1: Vertical profile of Earth's atmosphere.

where c_p is the specific heat. **Radiation** occurs when the most efficient way for energy transport is via absorption and re-emission of photons. The thermal profile is governed by equation of radiative transfert energy transport:

$$\frac{dT}{dz} = -\frac{3}{16}\frac{\alpha_R \rho}{T^3} T_e^4 \tag{1.13}$$

where α_R is the Rosseland mean absorption coefficient:

$$\frac{1}{\alpha} \equiv \frac{\int_0^\infty \frac{1}{\alpha_\nu}\frac{\partial B_\nu}{\partial T} d\nu}{\int_0^\infty \frac{\partial B_\nu}{\partial T} d\nu} \tag{1.14}$$

The thermal structure of an atmosphere can be determined via observations at different wavelengths, because these probe different depths in a planet's amosphere. At optical and IR wavelengths, the radiative part of an optically thick atmosphere is probed. Convective regions at $P \gtrsim 0.5 \div 1\, bar$ can be investigated at IR and radio wavelengths. The tenuous upper levels, at $P \lesssim 10\, \mu bar$, are typically probed at UV wavelengths, or via stellar occultations at UV, visible and IR wavelengths. At deeper levels in the atmosphere, typically at pressures $P > 1 \div 5\, bar$, where no direct information on the temperature structure can be obtained via remote observations, one usually assumes the temperature to follow an adiabatic lapse rate (eq 1.12).

1.4 Diffusion

The **net vertical flux** for a minor constituent i in an atmosphere in hydrostatic equilibrium is:

$$\Phi_i \equiv -N_i D_i \left(\frac{1}{N_i}\frac{\partial N_i}{\partial z} + \frac{1}{H_i^*} + \frac{\alpha_i}{T(z)}\frac{\partial T(z)}{\partial z} \right) - N\kappa \frac{\partial (N_i/N)}{\partial z} \tag{1.15}$$

where N is the global atmospheric number density, N_i is the number density of consitutent i, D_i is the molecular diffusion coefficient, κ is the Eddy diffusion coefficient (see section 1.4.1), H_i^* is the density scale height for each atmospheric constituent i, α_i is the thermal diffusion parameter and $T(z)$ is the atmospheric temperature at altitude z. The physical interpretation of the three terms in parenthesis is the following:

- $(1/N_i)(\partial N_i/\partial z)$: molecular diffusion caused by a gradient in the density N_i tends to smooth out density gradients, driving the mixing ratio of a constituent towards a constant with altitude.

- $(1/H_i^*)$: molecular buoyancy diffusion, with H_i^* the density scale height for individual constituents i, drives an atmosphere towards a barometric height distribution for each species i. Since the scale height varies with $1/m$, heavy molecules tend to concentrate at lower altitudes. Collisions between particles slow the diffusion process, so this latter is only effective at high altitudes.
- $(\alpha_i/T(z))(\partial T(z)/\partial z)$: thermal molecular diffusion, with α_i the thermal diffusion parameter, is triggered by gradients in temperature.

The molecular diffusion coefficient D_i is inversely proportional to the atmospheric number density: $D_i = b_i/N$, with b_i the binary collision parameter, which can best be determined empirically. The maximum rate of diffusion occurs for complete mixing, $\partial(N_i/N)/\partial z = 0$, which leads to the concept of limiting flux, Φ_l. For an atmosphere with small or no temperature gradient, where a light gas flows through the background atmosphere, the **limiting flux** can be written as:

$$\Phi_l = \frac{N_i D_i}{H}\left(1 - \frac{\mu_{a_i}}{\mu_a}\right) \approx \frac{N_i D_i}{H} \tag{1.16}$$

with H the atmospheric (pressure) scale height. Using $D_i = b_i/N$, we can approximate the limiting flux with:

$$\Phi_l \approx \frac{b_i(N_i/N)}{H}. \tag{1.17}$$

The binary collision parameter is given by:

$$b_i = C_b T^q \, cm^{-1} \, s^{-1} \tag{1.18}$$

where C_b and q are tabulated parameters. The net outward flux is limited by the diffusion rate, and cannot exceed the limiting flux. The limiting flux depends only on the mixing ratio of consitutent i and the pressure scale height.

1.4.1 Eddy diffusion coefficient

The last term on right side in equation 1.15 is the eddy or turbulent diffusion, with κ the Eddy diffusion coefficient. Eddy diffusion may occur if an atmosphere is unstable against turbulence, which occurs when Reynolds number $\Re \equiv \frac{lU}{\nu} > 5000$ (here l and U are characteristic length scale and velocity, and ν is the kinematic viscosity). The product vl gives a rough estimate of the diffusion coefficient κ. Assuming $l \approx H$ and v between 1 and $10^4 \, cm \, s^{-1}$, κ is of the order of $10^6 \div 10^{10} \, cm^2 \, s^{-1}$. Eddy diffusion dominates the atmospheres below the turbopause or homopause, while molecular diffusion dominates above the homopause. The eddy diffusion is usually estimated from observed altitude distributions of trace gases.

1.5 Escape

Escape for a particle occurs if its kinetic energy exceeds the gravitational binding energy and it moves along an upward trajectory withoug intersecting the path of another atom or molecule. There are two main kind of escapes: thermal escape and induced escape.

1.5.1 Thermal (Jeans) escape

Planetary and satellite atmospheres are confined by gravity. This is often characterized by the so-called **Jeans parameter**, the ratio of the potential to kinetic energy:

$$\lambda_{esc} = \frac{GMm}{kTr_{exo}} = \frac{r_{exo}}{H} = \left(\frac{v_{esc}}{v_{mp}}\right)^2 \tag{1.19}$$

where M is the planetary mass, v_{esc} is the escape velocity and v_{mp} is the most probable velocity (eq. 1.10). Integrating the upward flux in a Maxwellian velocity distribution above the exobase results in the **Jeans formula** for the rate of escape by thermal evaporation:

$$\Phi_J = \frac{N_{exo}v_o}{2\sqrt{\pi}}(1+\lambda_{esc})e^{-\lambda_{esc}} \tag{1.20}$$

where λ_{esc} is the escape parameter at the exobase. This is from the Chamberlain model, in which escape is due to tre fraction of upward moving atoms/molecules with velocities exceeding v_{esc} at the exobase. Since the tail of a Maxwellian distribution is depleted by escaping particles, it assumed to be rapidly replenished by collisions. In the Jeans limit, $\lambda \to 0$, the atmosphere is no longer bound and blows away with a flux $n(r_{exo})v_{therm}/4$ where the thermal speed is given by:

$$v_{therm} = \left(\frac{8kT}{\pi m}\right)^{1/2} \tag{1.21}$$

In the limit of large λ, the atmosphere is gravitationally retained and Jeans escape is negligible. In the Solar System, bodies with values of $\lambda \lesssim 50$ at the exobase have extended atmospheres and large values of $r_{exo}/r_p \geq 1.2$, where r_p is the planet radius (Strobel 2002). Given the dependence of Jeans formula from the mass (through the escape parameter), Jeans escape can produce a substantial **isotopic fractionation**. Calculation of Jeans escape can be used to predict whether or not an object has an atmosphere. It can also be used to evaluate which volatile ices one might find on a body, since the presence of such ices depends on both temperature and gravity.

1.5.2 Nonthermal escape

Jeans escape gives a lower limit to the escape flux from a body's atmosphere, but more often nonthermal processes dominate the escape rate. When a molecule is dissociated by UV radiation or an impacting electron, or when an ion dissociates upon recombination, the end products may gain sufficient energy to escape the body's gravitational attraction. Photochemical escape has its origin in the interaction of solar photons with neutrals in the upper thermosphere and exosphere and concerns all processes grouped as **photochemistry**. If the production rate of a particular species created via photochemistry is balanced by its loss rate, there is **photochemical equilibrium**. Indeed, the science of the upper region of the atmosphere where dissociation and ionization are important has been given a name, **Aeronomy** (Chapman 1960).

Photochemistry includes direct interactions of photons and photoelectrons[1] with thermospheric molecules. In such processes neutral particles can gain sufficient energy to escape into space. Typically, absorption of photons at far-infrared and radio wavelengths ($\lambda \gtrsim 100\,\mu m$) induces excitation of a molecule's lowest quantum states, i.e. the rotational levels. Photons at IR wavelengths ($\lambda \sim 2 \div 20\,\mu m$) can excite vibrational levels, while photons at visible and UV wavelengths may exicte electrons to higher quantum states within atoms and molecules. Photons at higher energies, $\lambda \lesssim 100\,nm$, may photoionize atoms and molecules. The penetration depth of any solar photon into an atmosphere depends upon the optical depth at the particular wavelength of radiation. These processes are described shortly.

1.5.2.1 Photochemistry processes

There are several types of dissociation. In the **photodissociation** (or photolysis) the process is triggered by a photon enough energetic ($\lambda \lesssim 1\,\mu m$) to break up molecules, for example:

$$CO + h\nu \rightarrow C^* + O^* \tag{1.22}$$

for photochemical escape of atomic carbon from Mars (Fox & Bakalian 2001), or:

$$O_2 + h\nu \rightarrow O + O \tag{1.23}$$

in icy satellites (Johnson et al. 2008). Here the asterisks denote excess energy. A photon can also ionize an atom and produce fresh ions, in the process called photodissociative ionization, or simply **photoionization**, for example:

$$O_2 + h\nu \rightarrow O_2^+ + e \tag{1.24}$$

[1]photoelectrons are electrons that carry on the excess of energy from the ionization of atmospheric consituents by EUV photons.

(Chamberlain & Hunten 1987) or:

$$N_2 + h\nu \rightarrow N^{+*} + N^* + e \tag{1.25}$$

for nitrogen escape from Mars (Fox & Dalgarno 1983). A similar process is the **photoelectron-impact dissociation**, where this time it is an electron which is responsible for the bond breaking, for example:

$$N_2 + e^* \rightarrow N^* + N^* + e \tag{1.26}$$

which occurs in Mars atmosphere (McElroy et al. 1977). Photodissociation typically takes places at high altitudes, whereas the reverse reaction, recombination, proceeds faster at lower altitudes. Therefore, the balance between dissociation and recombination may be affected by vertical transport. An example of **dissociative recombination** is

$$O_2^+ + e \rightarrow O + O \tag{1.27}$$

or:

$$NO^+ + e \rightarrow N + O \tag{1.28}$$

(Chamberlain & Hunten 1987). Dissociative recombination of molecular ions is one of the most exothermic reactions. An important process is also **electron-impact ionization**, where an electron ionizes an atom, e.g.:

$$Na + e \rightarrow Na^+ \tag{1.29}$$

which is an important source for ions in the Io torus (Schneider & Bagenal 2007 and section 2.1.1). Finally, when a fast ion meets a neutral, **ion-neutral reactions** may take place. In this case, a molecular ion and a fast atom may result, for example:

$$N_2^+ + O \rightarrow NO^+ + N \tag{1.30}$$

for production and escape of nitrogen atoms on Mars (Fox 1993). **Charge-exchange** is another process involving ion and neutrals: the energetic ion loses its charge, but retains its kinetic energy and a fast neutral is formed, for example:

$$O + O^+ \rightarrow O^+ + O^* \tag{1.31}$$

or

$$Na^+ + Na \rightarrow Na^* + Na^+ \tag{1.32}$$

which are both occurring at Io (Schneider & Bagenal 2007). Charge-exchange was first suggested as the dominant mechanism for ejecting sodium at Mercury (McGrath et al. 1986) and it plays an important role for sodium ejection at Io, where fast sodium atoms are created by charge exchange with magnetospheric plasma. See also section 3.3.2.

1.5.2.2 Other non thermal escape processes

When a fast atom or ion hits an atmospheric atom, the atom may gain sufficient energy to escape the body's gravitational attraction: this is the **sputtering**. It is usually caused by fast ions and is usually multiple, involving a cascade of collisions. I will return to sputtering process in section 3.2.3.

In a single collision, the atom is accelerated in the forward direction (conservation of momentum), a process generally referred to as **knock-on collision**.

Even electric fields contained in the ionospheres are responsible for non thermal escape. Such fields accelerate charged particles, which may transfer momentum to a neutral species upon collisions. Molecular diffusion leads to a separation in altitude bewteen heavier ions and lighter electrons, inducing a potential difference of electric field in the upper atmosphere that is directed normal to the surface. Such fields lead to an upward acceleration of ions, which in the polar regions induces the **polar wind**.

Blowoff, or **hydrodynamic escape**, occurs when a planetary wind comprised of a light gas (e.g. H) entrains heavier gas that would not be able otherwise to escape according to Jeans formula. Chamberlain & Hunten (1987) derived an expression for hydrodynamic escape in an atmosphere. They assumed that the light gas moves at high speeds approaching the sonic value, in which case there are large drag forces with other constituents. By ignoring the terms in dT/Dz and in κ in equation 1.15 the outgoing flux of the heavier gas 2 becomes

$$\Phi_2 = \frac{N_2}{N_1}\left(\frac{m_e - m_i}{m_c - m_1}\right)\Phi_1 \tag{1.33}$$

where the subscript 1 refers to the light gas, and m_c is:

$$m_c = m_1 + \frac{NkT\Phi_1}{bg_p} \tag{1.34}$$

with b the binary collision parameter. Escape requires $\Phi_2 > 0$ and thus $m_2 < m_c$. If Φ_1 is equal to the limiting flux, eq. 1.16, $m_c = 2m_l$. To maintain an atmosphere in a blowoff state requires *large* input of energy to the upper atmosphere. Solar energy is usually *not* large enough to mantain any present-day terrestrial-type atmosphere in a blowoff state.

Impact erosion can occur during or immediately following a large impact on a body that has a substantial atmosphere. For an impactor that is smaller than the atmospheric scale height, shock-heated air flows around the impactor and the energy is dispersed over a relatively large volume of the atmosphere. If the impactor is larger than the atmospheric scale height, however, a large fraction of the shock-heated gas can be blown off, since the impact velocity exceeds the

escape velocity from the planet. The atmospheric mass that can escape is the mass intercepted by the impactor multiplied by the enhancement factor ε_e:

$$\varepsilon_e = \frac{v_i^2}{v_e^2(1+\varepsilon_v)} \tag{1.35}$$

where v_i and v_e are the impact and escape velocities, and ε_v is the evaporative loading parameter, which is inversely proportional to the impactor's latent heat of evaporation. A typical value for ε_v is ~ 20 (for meteors). Significant escape occurs for $\varepsilon_e > 1$. If $\varepsilon_e < 1$, evaporative loading is much larger than the energy gained by impact heating, and the gas does not have enough energy left to escape into space. In the case of a colossal cratering event, the ejecta from the crater may also be large enough and contain sufficient energy to accelerate atmospheric gas to escape velocities. Such large impactors can remove all the atmosphere above the horizon at the location of the impact.

1.6 Ionospheres

UV photons at $\lambda \lesssim 100\,nm$ can ionize atoms and molecules. Radiative recombination of atomic ions (e.g. $O^+ + e^- \rightarrow O + h\nu$) is very slow compared to molecular recombination. Atomic ions are usually converted to molecular ions by ion-neutral reactions, and the molecular ions recombine. Photolysis in a tenuous atmosphere therefore leads to the formation of the *ionosphere*, a region characterized by the presence of free electrons. The electron density in the ionosphere is determined by both the ionization rate and how rapidly the ions recombine, whether directly, or indirectly via charge exchange. Each planet with a substantial atmosphere is expected to have an ionosphere.

1.6.1 Electric currents

Charged particles in the ionosphere gyrate around magnetic field lines. Charge separation of electrons and ions leads to electric fields. In the absence of collisions, both ions and electrons move together under influence of electric and magnetic fields, at the **drift velocity**:

$$\vec{v}_{drift} = \frac{\vec{B} \times \nabla \vec{\Phi}_{eff}}{B^2} \tag{1.36}$$

where $\vec{\Phi}_{eff}$ is the effective potential due to the convection and corotational electric fields and to ∇B. At high altitudes where lifetimes of ions are large, this type of transport is important. At lower altitudes, the drift motion of charged particles is

only momentary, until a collision with another particle deviates the electrons/ion's path. The bulk motion thus depends upon the ratio of the collision to cyclotron frequencies.

The relative drift motions of ions and electrons under the influence of magnetic and electric fields induces a current described by **Ohm's law**:

$$\vec{J} = \sigma_0 \left(\vec{E} + \frac{\vec{v} \times \vec{B}}{c} \right) \tag{1.37}$$

where σ_0 is the conductivity of the plasma, $\vec{v}$ the plasma velocity and $\vec{B}$ the interplanetary magnetic field. If collisions between particles are important, there is a finite conductivity, which consists of three components:

- the normal, direct or longitudinal conductivity σ_0, parallel to the magnetic field:
$$\sigma_0 = \left(\frac{n_i}{m_i \nu_i} + \frac{n_e}{m_e \nu_e} \right) q^2 \tag{1.38}$$
- the Pedersen conductivity σ_p, perpendicular to the magnetic field:
$$\sigma_p = \left[\frac{n_i \nu_i}{m_i(\nu_i^2 + \omega_i^2)} + \frac{n_e \nu_e}{m_e(\nu_e^2 + \omega_e^2)} \right] q^2 \tag{1.39}$$
- the Hall conductivity σ_h, perpendicular to both the magnetic and the applied electric field:
$$\sigma_h = \left[\frac{n_e \omega_e}{m_e(\nu_e^2 + \omega_e^2)} - \frac{n_i \omega_i}{m_i(\nu_i^2 + \omega_i^2)} \right] q^2 \tag{1.40}$$

where q is the electric charge, n the number density, ν the collisional frequency, and ω the cyclotron frequency. Subscript i refers to ions, e to electrons. These conductivities induce the **Birkeland**, **Pedersen** and **Hall currents**, respectively. Generally, σ_0, which is parallel to the magnetic field, is much larger than the Pedersen and Hall conductivities.

Electric currents, through the dissipation of electrical energy via charged particle collisions, lead to **Joule heating** of the ionosphere:

$$Q_J = \vec{J_\perp} \cdot \vec{E_\perp} = \frac{J_\perp^2}{\sigma_c} \tag{1.41}$$

with the Cowling conductivity:

$$\sigma_c = \frac{\sigma_p^2 + \sigma_h^2}{\sigma_p} \tag{1.42}$$

1.6.2 Airglow and Aurorae

Ionospheres are responsible for spectacular effects such as airglows and aurorae. Airglows result from emissions by atoms/molecules that have been excited by EUV solar photons or, to a less extent, by cosmic rays. They are confined to high altitudes, and are relatively uniform over the entire globe. Dayglow emissions, seen on a body's sunlit hemisphere and dominated by resonant scattering from atomic hydrogen, have been detected from many planets, as well as from Saturn's rings and a torus enveloping saturn at Titan's orbit. H is the most abundant species at very high altitudes because diffusive separation leaves the lightest element at the highest altitudes. Resonant Lyman-α scattering, therefore, gives a planet an extensive corona. In addition to H, airglow has been detected from other species such as nitric oxide, carbon monoxide and molecular hydrogen, oxygen and nitrogen. Nightglow emissions have beeen detected on Earth, Venus, Mars.

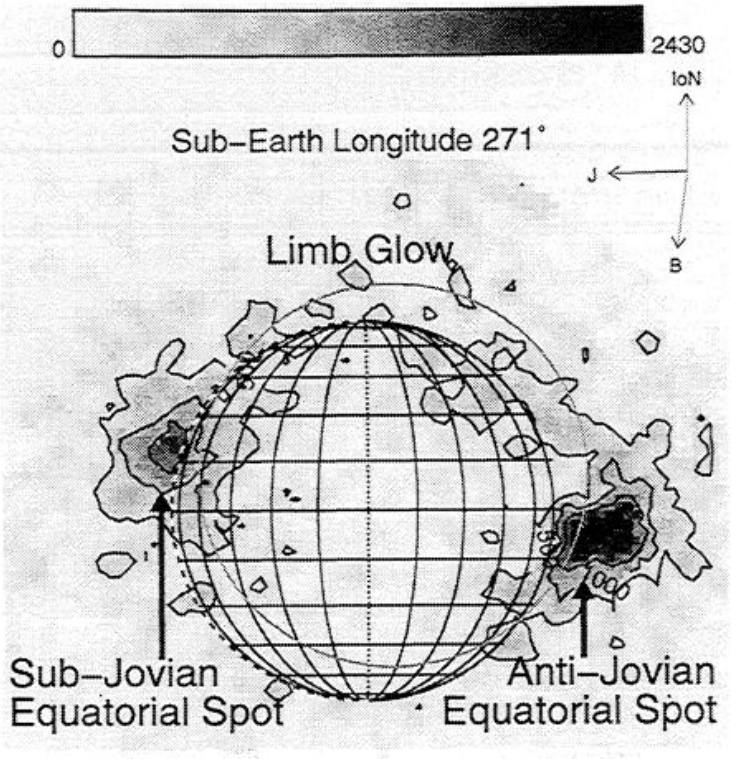

Figure 1.2: HST image of Io in the 135.6 nm of atomic oxygen.

Aurorae are seen as oval-shaped regions roughly centered about the magnetic north and south poles of a planet. In contrast to airglow, auroral emissions are triggered when charged particles from "outer space" excite atmospheric particles

through collisions. These charged particles enter the atmosphere along magnetic field lines. Since the footpoints of field lines form an oval about the magnetic poles, the emissions occur in an oval-shaped regions, referred to as the auroral zones. Atmospheric atoms, molecules and ions are excited through interactions with the precipitating particles, or by photoelectrons produced in the initial "collision" with these particles. Upon deexcitation, the atmospheric species emit photons which can be observed at optical, infrared, UV and, on Jupiter and Earth, at X-ray wavelengths.

Glowing spots of UV emissions are observed in the equatorial plane at the tangent points between field-aligned electrons and Io's atmosphere (Birkeland currents). Collisions between plasma and atmospheric gases creates the aurorae at Io. While aurorae on Earth and other planets are found near their magnetic poles, Io's brightest auroral emissions are found near its equator. Furthermore, the auroral emissions are caused by collisions involving particles trapped not along magnetic field lines intrinsic to Io, but along those of Jupiter. See fig. 1.2 from Retherford et al. (2000). This image has been taken at 135.6 nm line of atomic oxygen. The equatorial emissions result from interaction between electrons flowing along magnetic field lines and Io's atmosphere. The spots wobble up and down about Io's equator, due to the motion of the tilted jovian magnetic field past Io (section 2.1.1). The spot on the anti-jovian hemisphere is brighter than the subjovian spot, which may be caused by an asymmetry in the direction of the electron and ion convection patterns, as a result of the Hall effect, that produce hotter electrons on the antijovian side. A faint glow along the limb and an extended corona are detected as well. For a more detailed discussion of the coupling between Io and Jupiter's magnetosphere, see section 2.1.2.

2

Io

2.1 A complex environment

Io is one of the most fascinating satellites of the Solar System. It is similar in size ($1\,R_{Io} = 1821\,km$) and density ($3.53\,g\,cm^{-3}$) to the Moon but, contrary to this latter, it is not a geologically dead body, due primarily to its intense volcanic activity, which is driven by the internal tidal heating caused by Io's orbital resonance with Europa and Ganymede. At Io not a single impact crater has been identified, suggestive of an extremely young surface ($\lesssim$ few Myrs). Moreover, Io is far richer in moderately volatile elements, such as sodium and sulfur, than is the Moon. Reflectance spectra show that Io's crust is dominated by sulfur-bearing species, in particular SO_2 frost. Escape of the volatile materials extracted from Io's interior by these volcanoes extends Io's influence throughout the Jovian magnetosphere. In fact, effects of iogenic plasma extend to other medicean satellites - and beyond! For example, Europa e Ganimede have oxygen atmosphere created and lit up by impact of iogenic plasma. Moreover, material emitted from Io eventually escape Jovian system, via fast neutrals or via plasma flowing out of Jupiter's magnetotail (which extends beyond Saturn): the glow of fast neutrals can be seen at distances of 1 AU from the system!

Our understanding of Io was revolutionized by the Voyager spacecraft flybys in March and July 1979, that discovered the only known extra-terrestrial volcanism. Years later, the Galileo Jupiter orbiter flew within $\sim 900\,km$ of Io's surface on December 1995, revealing that Io has a large iron core and excluded the presence of a magnetic field. Tidal heating of the interior produces a global heat flux 40 times the terrestrial value, producing intense volcanic activity and a global resurfacing rate averaging perhaps to $1\,cm\,yr^{-1}$. The volcanoes and the frost support a thin, patchy SO_2 atmosphere with peak pressure of about 10^{-8} bars. Ionized gas from Io's ionosphere, corona, and extended clouds is the primary source of plasma in

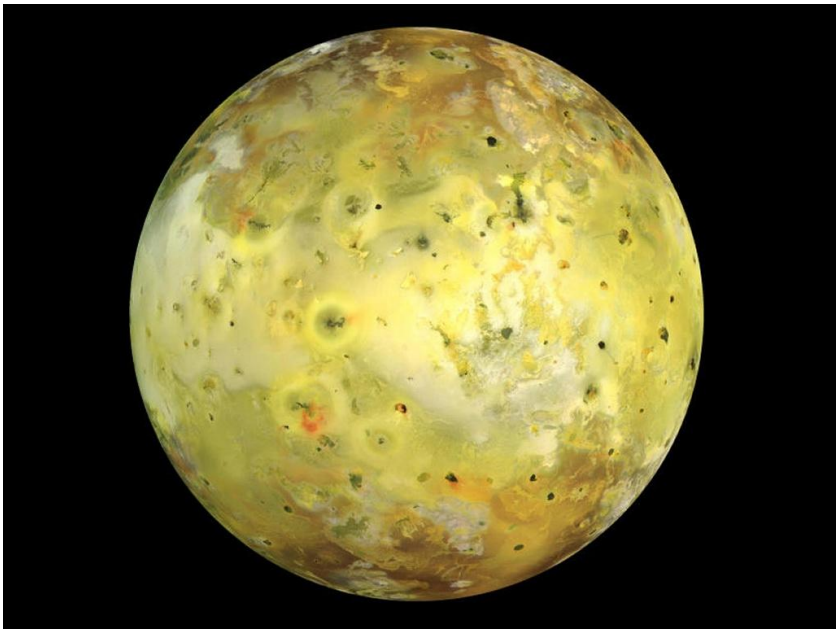

Figure 2.1: Io as seen from Galileo spacecraft.

Jupiter's magnetosphere. This plasma from Io is confined in a torus, which is currently one of the most intensively studied astrophysical plasmas.

2.1.1 The plasma torus

The torus is a region enclosing Io's orbit at 5.9 $R_{♃}$ ($1R_{♃} \sim 70000\,km$) and with a thickness of about $1R_{♃}$. It contains neutral atoms (Na, K, O, S) and a plasma dominated by ions of S and O. In reality, there are three main regions of Io torus: the **outer region** ($6-7\,R_{♃}$) has hot ($\sim 100\,eV$), relatively fresh plasma that moves outward on timescales of tens of days. The **inner cold torus** inside of 5.7 $R_{♃}$ (dropping off sharply inside 5.3 $R_{♃}$) lacks a significant source of fresh ions, and transport is so slow that plasma has time to cool below 1 eV. While emission from the inner, colder torus are confined to the optical wavelength range, both optical and UV emissions have been observed from the hot outer torus. The **narrow ribbon** ($5.6 \div 6\,R_{♃}$) is a stagnated region of modest neutral source and slow transport rates, where the plasma has time to radiate away thermal energy and cool to ion temperatures of 20 eV. It shows up very clearly in some years, while it is nearly absent in other years. Ribbon has different aspects, depending on the component - see fig. 2.2 from Schneider & Bagenal (2007). As it is clear from this image, S^{+} (6731 Å) dominates in the cold torus, whereas S^{++} (685 Å)

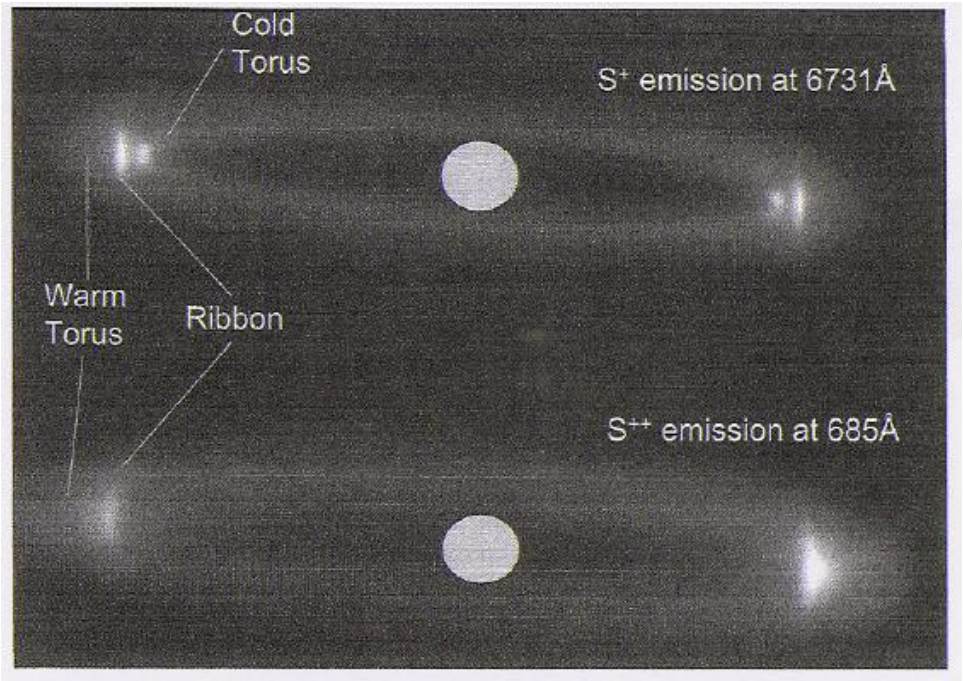

Figure 2.2: Regions of the plasma torus.

dominates in the warm torus. Ribbon appears brighter at the edges because of projection effects. Besides of this, plasma is twice brighter at the dusk side (west, receding) than at the dawn side (east, approaching), because of the electric field imposed across the torus by the plasma flow down Jupiter's magnetotail. This field is generated by the anti-sunward flow of plasma that originates in the Io torus and flows down the tail and accelerates particles causing an inward motion of the dusk end of the torus. The torus brightens there due to adiabatic compression of the electrons that excite the torus emisions.

The plane of symmetry of the torus is the centrifugal equator, the locus of points where the magnetic field lines are farthest from the rotational axis. The basic shape results from Jupiter's tilted magnetic field and its rapid 10-hr rotation. In fact, torus plasma in Jupiter's magnetic field is confined not by magnetic mirroring but by centrifugal forces. The plane of symmetry of the torus makes roughly an angle of 3°with the magnetic equator and 7°with the rotational equator. While rotating around Jupiter, this equator wobbles of ±7°as seen from Earth. A picture of the complex environment around Io is reported in 2.3, from Saur et al. (2004).

The torus **vertical structure** reveals ion temperatures. The vertical extent of the torus depends upon the temperature and mass of the ions. To first approximation the plasma density $N(z)$ decreases exponentially with distance z away from

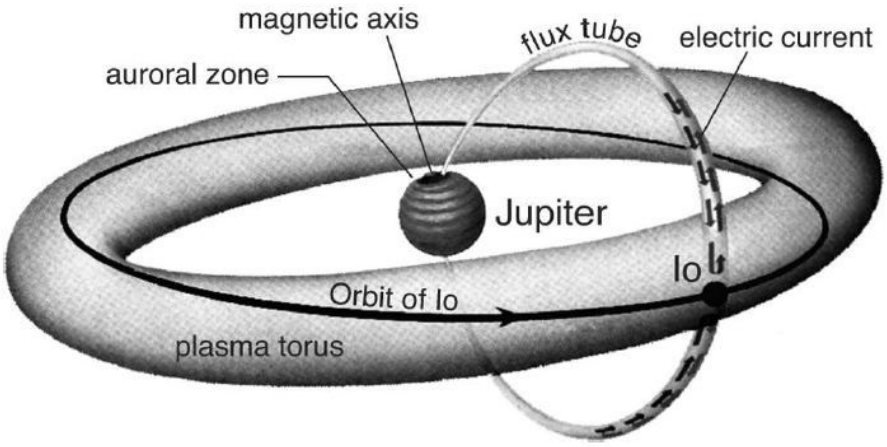

Figure 2.3: The interactions between Io's plasma torus, Jupiter's magnetosphere and ionosphere, and neutral cloud.

the centrifugal equator:

$$N(z) \approx N_0 \exp(-z^2/H^2) \tag{2.1}$$

where the scale height is $H \approx \sqrt{2kT_i/3m_i n^2}$, n is the orbital rotation rate and m_i and T_i are mass and temperature of the ion species i. For H in units of Jovian Radii, $H \sim 0.64 \cdot (T_i/A_i)^{1/2}$, where T_i is in eV and A_i is average ion mass in atomic mass units.

Torus **radial structure**, instead, reveals plasma transport processes. Radial transport can be thought of as a diffusive process that is strongly influenced by centrifugal forces (Thomas et al. 2004): in fact, radial outward transport is faster than inward transport, which is slow enough to allow ions to cool. Thus, outward flow is energetically favoured vs. inward flow and leads to the above-mentioned dawn-to-dusk electric field.

Concerning the formation of the plasma torus, given that Io's orbital corridor is within the torus volume, and that the composition of ions in the torus is the same as neutrals or compounds thought to be on the surface and emanating from Io's volcanoes, there is no doubt that the material in the torus has escaped from Io. Thus, torus is a self-sustaining plasma, since it is the impact of torus ions on Io's surface or atmosphere that causes the sputtering that supplies the clouds in the first place. However, the nature of the process or processes is still obscure.

The rate at which Io supplies mass to the torus has been estimated to be $1000\, kg\, s^{-1}$ (Schneider & Bagenal 2007). Therefore, only 0.1% of the initial mass has been lost throughout geologic time to the Jovian magnetosphere (Dessler 1980). Both forbidden (at optical wavelengths) and allowed transitions have been ob-

served, and used to determine the electron density and temperature in the torus. Typical maximum electron densities are a few thousand cm^{-3}. The electron temperature is $T_e \sim 4\,eV$ or $50000\,K$, with a hotter, minor component at $\sim 600\,eV$. Fresh pickup ions gyrate with a speed of $57\,km\,s^{-1}$ in a plane perpendicular to the local magnetic field. Estimates to maintain the plasma torus as observed suggest a production rate of $\sim 10^{28} \div 10^{29}\,ions\,s^{-1}$.

Electron-impact ionization is important in the creation of torus ions. This process (see formula 1.29) creates a fresh ion with a high energy relative to the corotating plasma. This pick up ion is picked up in the fields that causes corotation, and spirals around its field line with a velocity equal to its initial motion. Depending on plasma density, elastic collisions and charge-exchange can also contribute to the ionization. An oxygen atom is more likely to be ionized by charge exchange (typical lifetime 18 hours) or an elastic collision (13 hours) than by electron impact ionization (55 hours). In an elastic collision, a fast ion impinges on a slow neutral, sending it off at a high velocity nearly perpendicular to the plasma flow. In a charge-exchange reaction (formula 1.32) the corotating ion strips off an electron from a neutral. The neutral is ionized and accelerated to corotational speed, while the former ion becomes a fast neutral, flying out through the magnetosphere. These create jets, fans and loops. A giant disk-shaped Na cloud extends out to a few hundreds Jovian Radii, formed by fast neutrals flung out from magnetosphere via charge exchange or elastic collisions between particles in the Io plasma torus and neutral clouds.

2.1.2 Io's atmosphere and its interaction with the plasma torus

The corona, or exosphere, is the region within $\sim 6\,R_{Io}$ consisting of bound and escaping atoms which are still in the region where Io's gravity dominates over Jupiter's. Contrary to the case of Mercury, its exobase is not the satellite's surface. Indeed, exosphere and surface are separated by a collisionally thick layer: Io's atmosphere. Volcanos are the ultimate source of material for Io's atmosphere and surface, but the transport of this material between them is not yet fully understood. Escape from Io occurs through intermediary of the collisionally thick atmosphere, with little or no direct ejection from the surface (Wilson et al. 2002). Direct volcanism is also negligible, because vent velocities are $\sim 1\,km\,s^{-1}$, well below escape speed ($v_{esc} = 2.6\,km\,s^{-1}$). Escape thus occurs in a complex region where magnetospheric plasma flows through Io's upper atmosphere (plasma corotates with Jupiter at $74km\,s^{-1}$, overtaking Io which orbits at $17km\,s^{-1}$). Io's atmosphere is mostly composed of sulfur dioxide (SO_2), which is at most a trace constituent in all other known planetary atmospheres. This atmosphere is tenuous, being about

a billion times thinner than Earth's. Io's low gravity allows the atmosphere to escape by a variety of processes, but volcanic outgassing resupplies the escaping atoms on a timescale of hours or days.

Interestingly, Io's atmosphere is dramatically denser near its equator than at its poles, as observed with images of Io's H I Lyman-α emissions: see fig. 2.4, from Feldman et al. (2000). The primary source of Io's atmosphere is not yet determined. Volcanic plumes, evaporation of surface frosts by hot lava flows, sublimation, and surface sputtering by magnetospheric particles are all likely sources, but their relative contributions are unknown (Lellouch 1996).

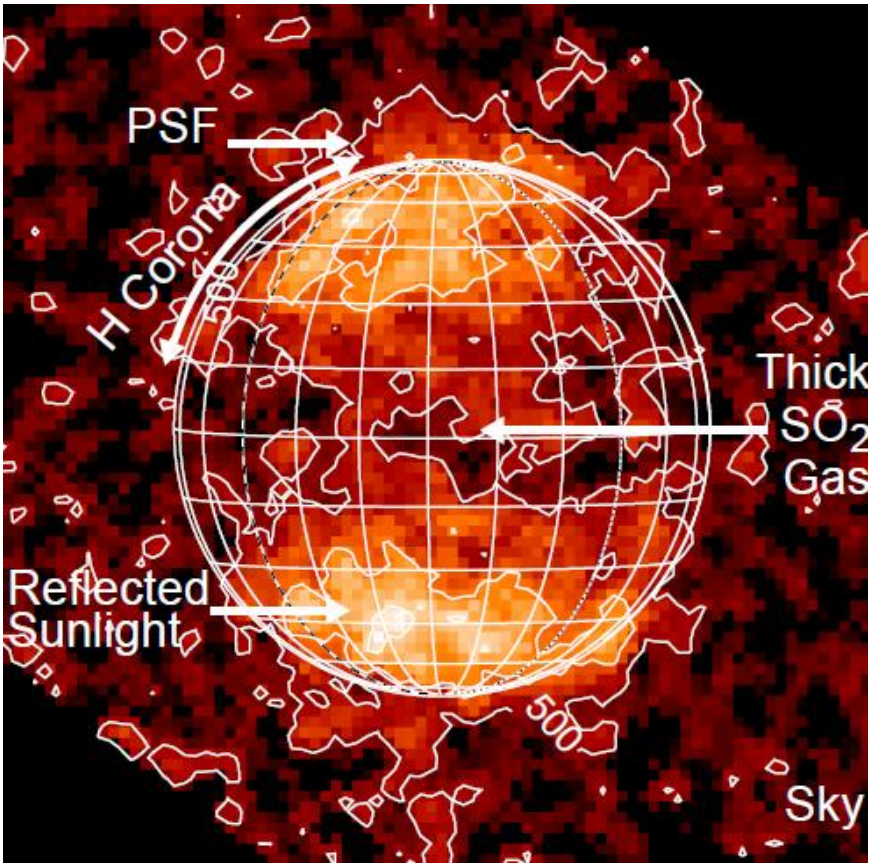

Figure 2.4: STIS image of reflected solar HI Lyman-α emission (1216 Å) at Io. Here, lack of light indicates a thicker SO_2 atmosphere, because SO_2 gas strongly absorbs photons at 1216 Å.

In fact, flow of plasma through Io's ionosphere is a significant driver of Io's atmospheric escape. In situ measurements by the Galileo spacecraft have revealed significantly slowed plasma near Io (Frank et al. 1996) and a dense ionosphere

around it (Hinson et al. 1998), suggesting that Io's collisionally thick neutral atmosphere interacts with a significant flux of plasma. Flanks of Io are the places where interactions between atmosphere and corona happen: inelastic collisions heat the neutrals, and charge-exchange and electron impact ionization excite or ionize neutrals. Farther from Io, electron impact ionization of the neutral corona crates pickup ions which gyrate around the local magnetic field with a speed equal to the relative motion between the original neutral and the local plasma flow. Ions have gyroradii of km, while fresh electrons have smaller gyroradii in the opposite direction. This separation of charge leads to a **pickup current** in the radial direction. The relative contribution from the conduction current through Io's ionosphere vs. the pickup current generated by pickup ions remains an issue of debate that awaits more sophisticated models (Saur et al. 2004).

By far more intense are the tremendous currents that connect Io to Jupiter's ionosphere. The existence of such currents has been shown directly via HST images of auroral emissions along the wake of the footprint of Io's flux tube - see fig. 2.5.

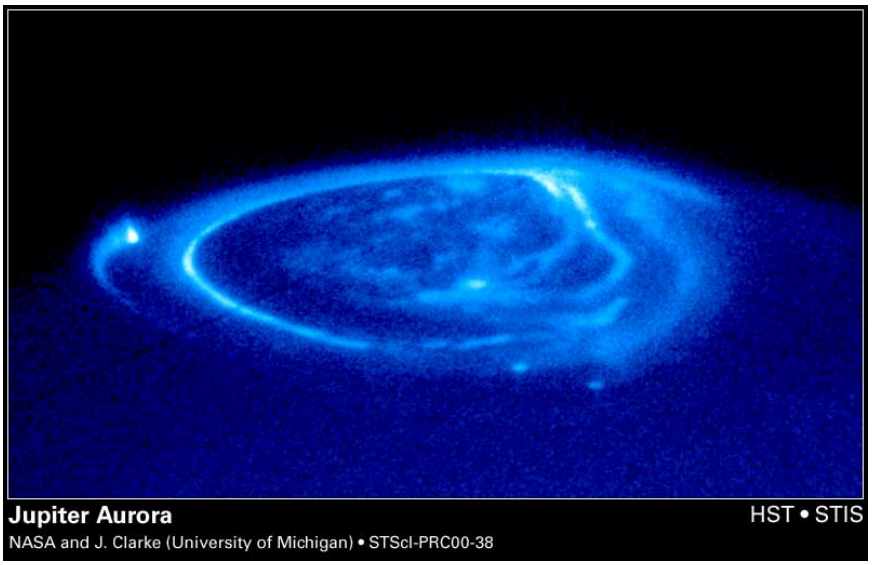

Figure 2.5: The footprint of Io on Jupiter's ionosphere is the bright point on the left edge.

The mechanism is similar to the situation used to explain the Lenz's law. If a wire is dragged through a magnetic field, the variation of the magnetic flux through the wire generates an induced current in the wire. In the case of interest, Io is the wire itself, with the flanks facing and opposing Jupiter acting as the ends of the wire. Since a) Io's surface or interior is modestly conducting, b) currents

are more easily conducted by materials surrounding Io as its ionosphere and the plasma, and c) currents easily flow *along* field lines instead of across field lines, currents induced across Io are closed by currents that flow along field lines between Io and Jupiter's polar ionosphere in both hemispheres. *This* current system is the cause of the deflection of the plasma when it arrives at Io (only 10 % of the plasma impacts on Io's internal atmosphere). In fact, plasma does not flow around, over and under Io, as the case of a rock on a riverbed. Io's case resembles more a

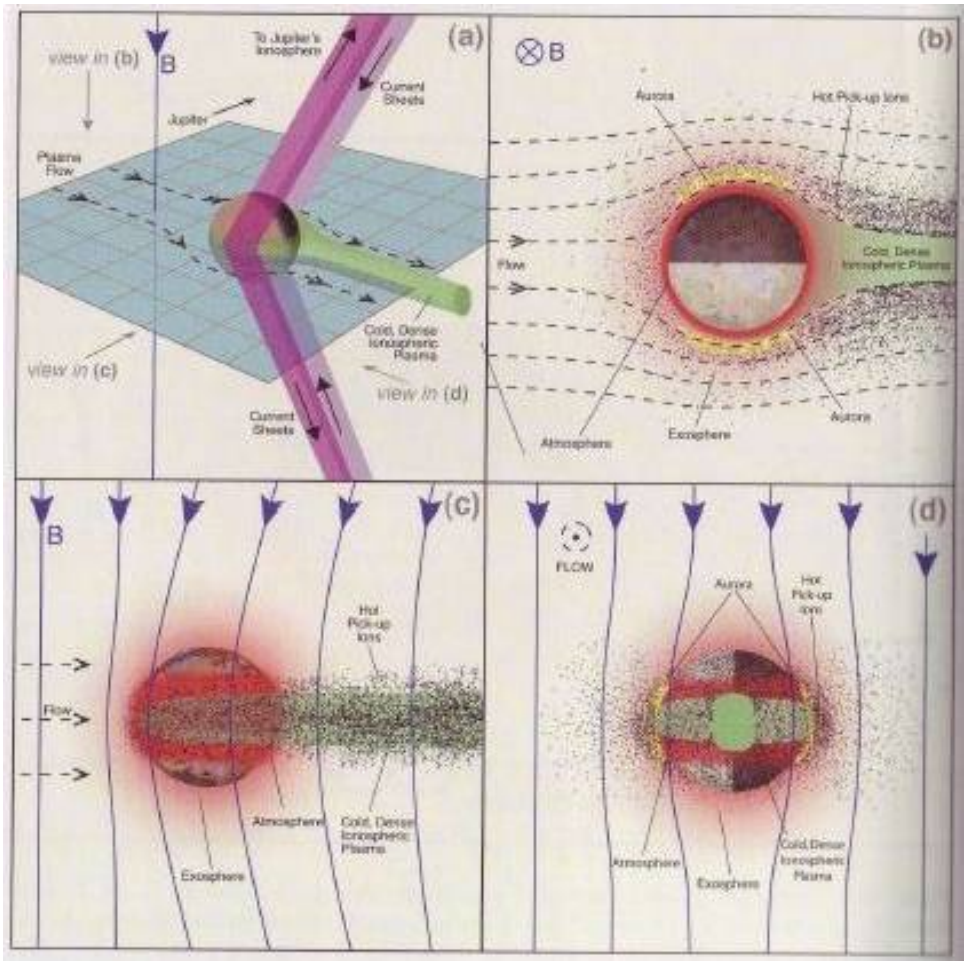

Figure 2.6: Regions of the plasma torus as seen from different points of view.

cylinder case. See fig. 2.6, from Schneider & Bagenal (2007), that shows the interaction of Io and plasma torus and the coupling of the satellite to Jupiter's ionosphere as seen from different points of view. Torus plasma is diverted around Io by its conducting ionosphere and electrons and ions flow through Io's exosphere

at speeds of $57 \pm 30\ km\,s^{-1}$. Through these currents, the ionosphere tries to enforce corotation throughout the magnetosphere. Indeed, inside of $5\ R_{♃}$ the magnetosphere is in rigid corotation with the planet, but at larger distances there is a significant departure from corotation. At jovian distances of $6 \div 10\ R_{♃}$ the plasma lags behind corotation by $1 \div 10\%$, while beyond $20\,R_{♃}$ the azimuthal flow is at a constant speed of about $200\,km\,s^{-1}$.

Photochemical models predict that molecular ions of SO_2^+, SO^+, and S_2^+ should form in the ionosphere along with NaX^+ (Moses et al. 2000). If molecular ion reactions are responsible for producing NaX^+ (Johnson 1994), then pickup ions of SO_2^+ and other species must be present at comparable numbers. Species of S, O, and Na are probably sputtered from the atmosphere at rates proportional to their abundances, with S and O escape rates each being at least an order of magnitude larger than Na (Smyth 1992).

Finally, io triggers also Jupiter's radio emission (Bigg 1964): S-bursts, lasting few minutes, and L-bursts lasting for up to 2 hours. These are due to magnetic disturbances which propagates along these field lines (the Alfvén waves).

2.2 Io's Neutral Cloud

It is clear from previous discussion that this complex environment in which Io is embedded would not be possible without Io's exosphere (or corona). The presence of an atmosphere at Io was inferred for the first time from indications of an ionosphere in Pioneer 10 spacecraft radio occultation observations (Kliore et al. 1975). At about the same time, neutral sodium atoms were the first substance to be discovered above Io's surface (Brown 1974b). Soon Trafton et al. (1974) demonstrated that the sodium emission came from extended neutral cloud ($\sim 20\ R_{Io}$) instead than from the satellite itself. The fact that D-line brightness is maximum when Io is at elongation and is at least an order-of-magnitude fainter when Io is near conjunction (Macy & Trafton 1975) was the decisive proof that sodium is lit up by resonant scattering (see section 2.3). Later, potassium (Trafton 1975) was detected to come also from extended clouds extending large distances from Io. Voyager 1 spacecraft observations made the first direct observation of Io's *near-surface* atmosphere with a spectrum of SO_2 through absorption of thermal infrared emission from the Loki volcano (Pearl et al. 1979). Unfortunately, it is not possible to spatially resolve this inner atmosphere close to Io, i.e. the optically thick layer at Io's surface, because of Io's high geometric albedo (plus the effects of atmospheric seeing for ground-based observations).

Since sodium is so bright at visible wavelength, ground-based studies of Io's exosphere have focused in this region in the visible window. Although on average the sodium emission remains roughly constant from one year to the next, the

intensity is about 25% higher when Io is at eastern elongation (orbital phase 90°) than at western elongation (orbital phase 270°).

Escaping material is composed of the elements of volcanic volatiles SO_2, S_2, $NaCl$, KCl and other plausible combination. Ions observed in Io's ionosphere include molecular SO_2^+ and SO^+ and atomic ions for each neutral atomic constituent, including H^+ and Cl^+ (Retherford 2003). Although silicate volcanism occurs on Io's surface, no refractory elements such as Si, Fe, Mg or Al have been detected in the neutral cloud or torus (Schneider & Bagenal 2007). Substantial internal processing of material related to the heating that drives Io's volcanism has depleted volatile elements like H_2O over the time since Io's formation (Spencer & Schneider 1996). Nevertheless, Io is not in danger to running out of SO_2. Io's sodium clouds result mostly from a combination of two atmospheric escape processes at Io. Neutralization of Na^+ and/or NaX^+ pickup ions produces the "stream" and the "jet" (sections 2.2.2 and 2.2.3). Atmospheric sputtering of Na by plasma torus ions produces the banana-shaped cloud near Io and a diamond-shaped sodium nebula (see section 2.2.1). The total ejection rate of sodium from Io varies from 3 to $25 \times 10^{26}\, atoms\, s^{-1}$.

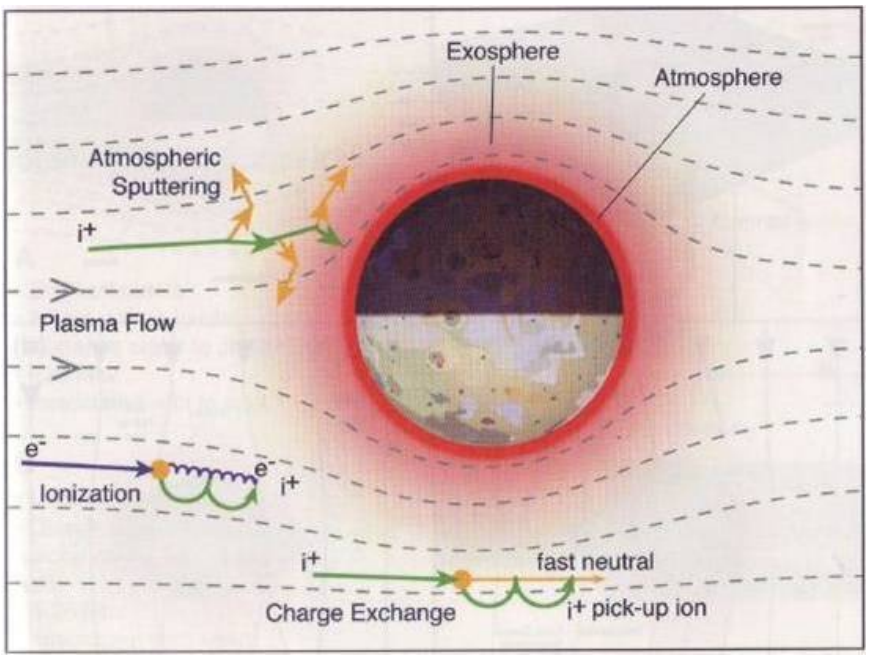

Figure 2.7: Plasma/atmosphere interactions at Io.

The extent of the neutral cloud is determined by the lifetime of the individual atoms. A neutral can get ionized through photoioniation, electron impact ioniza-

tion, elastic collisions or charge exchange. Photoionization of neutrals near Io is very slow: typical lifetimes for O and S are a few year, for SO_2 it is about 1 year, and for Na it is about 1 month. These times are much longer than the survival times against other processes, which are collisional in nature. However, lifetimes of neutrals against electron impact ionization depend upon density and temperature of the electrons. Lifetimes are in general quite short: 1 hour for Na and K, 55 hours for O and 10 hours for S.

The main mechanism of ejection of sodium is **sputtering**, a momentum transfer process in which a torus ion collides with an exospheric neutral, which in turn can collide with other atoms. One single torus ion can thus transfer enough momentum for several atmospheric atoms or molecules to be ejected into Io's neutral cloud (and ultimately into plasma torus) or possibly escape from the satellite. This is the primary pathway for material to be supplied to neutral clouds and ultimately to Io's torus. Another process is **electron impact ionization** (see formula 1.29), where an electron ionizes an atmospheric atom, which is then accelerated up to the speed of plasma along field lines and leaves Io. **Charge-exchange**, when a torus ion collides with an exospheric neutral, giving a fast neutral and a fresh ion (formula 1.32) may be an important source of ions for both the stream and the jet. These high speed neutrals retain the high velocity of the plasma, nearly $70\,km\,s^{-1}$, thus escaping from jovian system (the escape speed from Jupiter at Io's distance is only $24\,km\,s^{-1}$). **Elastic collisions** between ions and atoms can also eject material at speeds intermediate between those of sputtering and those of charge-exchange. **Electron-impact dissociation** breaks down molecules into their component atoms. Finally, another process, known as **molecular ion dissociation**, creates a neutral spray of fast atoms which populate the vast region sometimes called the Mendillosphere (Mendillo et al. 1990) which extends itself up to $400\,R_{\mathbb{Q}}$.

In the following pages I will depict the three main regions of the extended neutral clouds, starting with the forward cloud which is the object of study of this part of the thesis dedicated to Io.

2.2.1 The Forward Cloud

The forward cloud (Brown 1974a) is the most prominent feature of Io's neutral cloud and leads Io as it orbits around Jupiter - see fig. 2.8 from Schneider et al. (2008). Its banana shape (first reported by Matson et al. 1978) is well explained, as a combination of celestial mechanics (dominated by Jupiter's gravity) and non-uniform ionization rates (Burger et al. 1999). Neutral cloud contains slow atoms, probably ejected isotropically from Io (Smyth & Combi 1988), escaping from the surface, traveling only few $km\,s^{-1}$ relative to Io, therefore orbiting Jupiter with Io. Atoms ejected backward relative to Io's orbital motion of $17\,km\,s^{-1}$ have a

speed below that needed for circular motion around Jupiter. They thus precipitate towards Jupiter, converting potential energy into kinetic energy, getting ahead of Io. Viceversa, particles launched ahead of Io have higher speed than that required for orbital motion around Jupiter, thus they move on larger orbits, where they lose kinetic energy and at the end they finish behind Io. The net result is a neutral cloud with one part extending ahead and inside Io's orbit, and another extending behind and outside. In about 20 hrs, atoms launched from Io at only few $km\,s^{-1}$ can reach distances of 6 $R_{\mathcal{Y}_+}$ ahead of, or behind, Io. The banana shape is further refined adding to this effect the non-uniform ionization. In fact, the leading cloud lies inside Io's orbit, where plasma is cool, so atomic lifetimes are longer than outside Io's orbit. The trailing cloud is subject to plasma warm enough to ionize much of the cloud ($5\,eV$ electrons are enough energetic): 4-hr of ionization lifetime for sodium is short compared to 20-hrs travel from front to back of Io, so the trailing cloud is virtually non-existent.

Oxygen and sulfur clouds are much denser than sodium one. Differencies in reaction rates lead to dramatic differencies in their spatial distributions. For example, oxygen and sulfur have greater lifetime for ionization than sodium, so that the outer trailing cloud may be comparable in density and extent to the inner leading cloud, unlike the case for sodium (Schneider & Bagenal 2007).

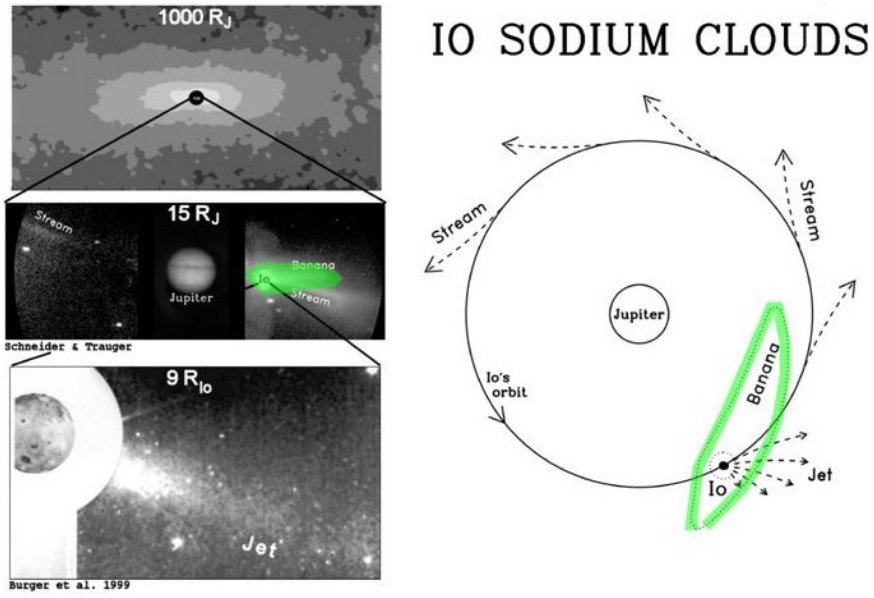

Figure 2.8: The forward cloud, or "banana", main component of Io's neutral cloud.

2.2.2 The directional feature

Early imaging studies of the fast sodium features Goldberg et al. (1984) showed a fast (i.e. $\lesssim 100\,km\,s^{-1}$) jet, produced by pickup ion neutralization in Io's atmosphere - see fig. 2.9 from Schneider et al. (2008). The directional feature, as it is often called the jet, is a narrow feature directed away from Jupiter perpendicularly to the Jovian magnetic field line at Io. It is more variable and energetic than the forward cloud (Wilson et al. 2002). It extends in the anti-Jovian direction and is most easily detected when Io is near maximum elongation from Jupiter. It is sometimes narrow ($1/2\,R_{\jupiter}$ or less at $2\,R_{\jupiter}$ of distance from Io), and usually directed at an angle of up to 20°out of Io's orbital plane. It is probably generated by elastic collisions between corotating torus ions and neutrals in Io's atmosphere. Direction and velocity are consistent with this hypothesis: sideways, medium-velocity ejections are more probable than head-on collisions. The directional feature appears tilted and collimated due to the loss of atoms by ionization in the torus and enhanced ejection in the equatorial plane.

The banana cloud and the jet may be indicative of conditions in separate, localized atmospheric regions on Io. The banana cloud is populated mostly from ejection over Io's *trailing*, subjovian quarter (Smyth & Combi 1988), while low-speed atoms sputtered from the *leading* longitudes of Io populate the inner nebula beyond Io's orbital distance (Smyth 1992). Thus, isotropic atmospheric sputtering will populate both of these cloud regions.

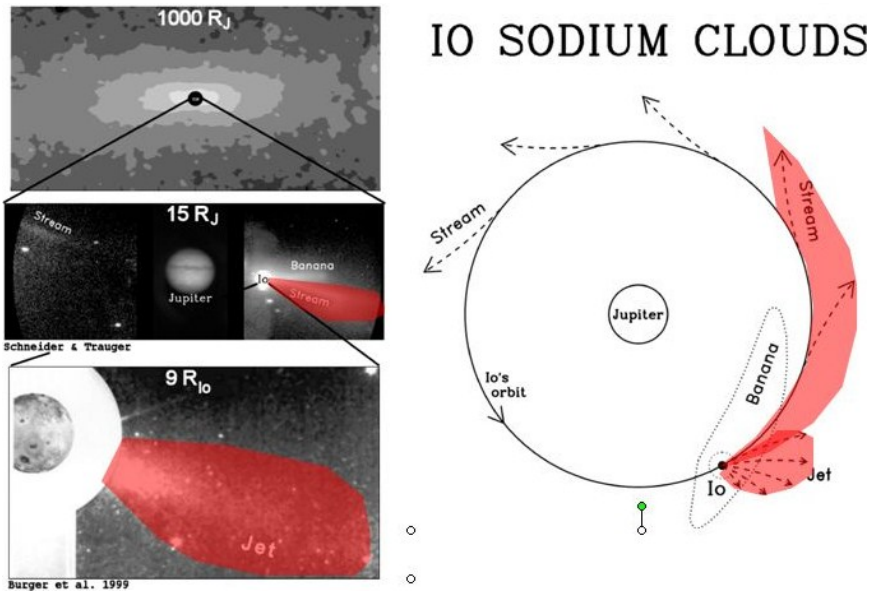

Figure 2.9: The fast jet and stream of Io's neutral cloud.

2.2.3 The molecular ion stream

Another fast sodium feature was discovered by Schneider et al. (1991b) and originates in the plasma torus. This feature, called sometimes the "stream" (see fig. 2.9), has been shown to result from dissociation of unidentified molecular pickup ions containing sodium (NaX^+) in the torus (Wilson & Schneider 1994). Despite directional feature, it can be quite narrow and moves alternatively N and S or Io's orbit in a manner which correlates to Io's magnetic longitude. It may appear intermittently. Unlike the forward cloud, the molecular ion stream may be unique to sodium-bearing ions: streams of oxygen or sulfur are not expected. A possible candidate for the sodium-bearing ion is $NaCl^+$, after chlorine has been discovered at Io (Küppers & Schneider 2000).

2.3 The resonant scattering

Since its discovery nearly 40 years ago (Brown 1974b), sodium has proved itself to be essential for understanding the escape of Io's atmosphere. Despite its small abundance, optical wavelength observations of sodium have several advantages over observations of more abundant species such as oxygen and sulfur. The emission from these species results from electron impact excitation in the plasma torus, so the observed emission is a function of both the neutral density and the electron density and temperature of the plasma, making the neutral density profile difficult to determine from observational data without detailed modeling. Moreover, the lines are weak and at wavelengths inaccessible from the ground. Because the sodium D lines are formed through a resonant transition at optical wavelengths, sodium can be observed at Io in both emission and absorption when in sunlight.

A solar photon pushes an electron to the first excited state, and when this returns to the ground state (after nearly 10^{-7} sec) it emits a photon. The first excited state is in reality double due to fine structure, so this process can actually emit in two possible wavelengths: 5890 and 5896 Angstrom for the D2 and D1 line respectively - see fig. 2.10 from Hunten et al. (1988).

A quantitative measure of this effect is represented by the **γ-factor**. It is the ratio between the intensity of the absorption line at a given wavelength and the intensity at the continuum. It is an indicator of how much solar light a sodium electron experiences at a given velocity with respect to the Sun. When Io has zero heliocentric velocity (this happens when it is at conjunctions), atoms "see" a very small amount of solar light, corresponding to the bottom of the Fraunhofer line. In this case the γ-factor is ~ 0.05, meaning that the sodium atoms receive $\sim 5\%$ of the solar continuum and the brightness of resonant scattering will be faint (right side of the fig. 2.11). As Io increases the modulus of the heliocentric radial

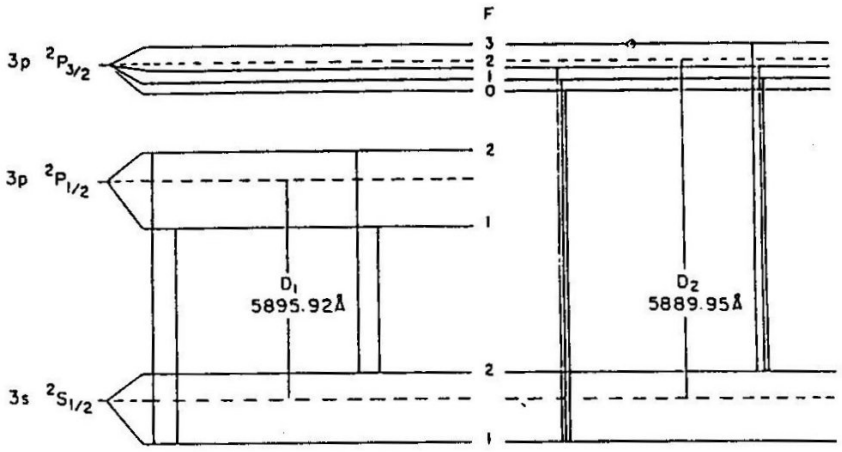

Figure 2.10: Structure of the sodium levels interested by the resonant scattering.

velocity, the atoms have more light available for scattering and the sodium cloud will be brighter (left side of fig. 2.11). The range of Doppler shift associated to Io's orbital motion ($17.3\ km\,s^{-1}$) is about ± 0.34Å, which corresponds to a variation in the the γ-factor of $0.05 \div 0.70$. The brightness of the neutral cloud is usually expressed in **Rayleighs** (Chamberlain & Hunten 1987):

$$1\ Rayleigh = \frac{10^6}{4\pi}\ photons\, cm^{-2}\, s^{-1}\, sr^{-1}. \tag{2.2}$$

For optically thin clouds, the brightness in Rayleighs (or, more commonly, kilo-Rayleighs) I is linearly related to the column density N through the g-factor:

$$I\,(kR) = gN(4\pi/10^9) \tag{2.3}$$

where N is the column density expressed in $atoms/cm^2$. The g-factor depends essentially on the solar flux $F_\odot(\lambda_{Na})$, which in turn depends on the heliocentric distance of the object, and on the γ-factor, which depends on the radial velocity of the atoms with respect to the Sun (Brown & Yung 1976):

$$g\ =\ \left[\gamma \cdot \pi F_\odot(\lambda_{Na}) \cdot \frac{\lambda^2}{c}\right]\ \frac{\pi e^2}{mc} f \tag{2.4}$$

where f is the oscillator strength of the transition line, e and m are charge and mass of the electron, c the speed of light. The g-factor is expressed in $photons\, atom^{-1}\, s^{-1}$, or, more commonly, in s^{-1}.

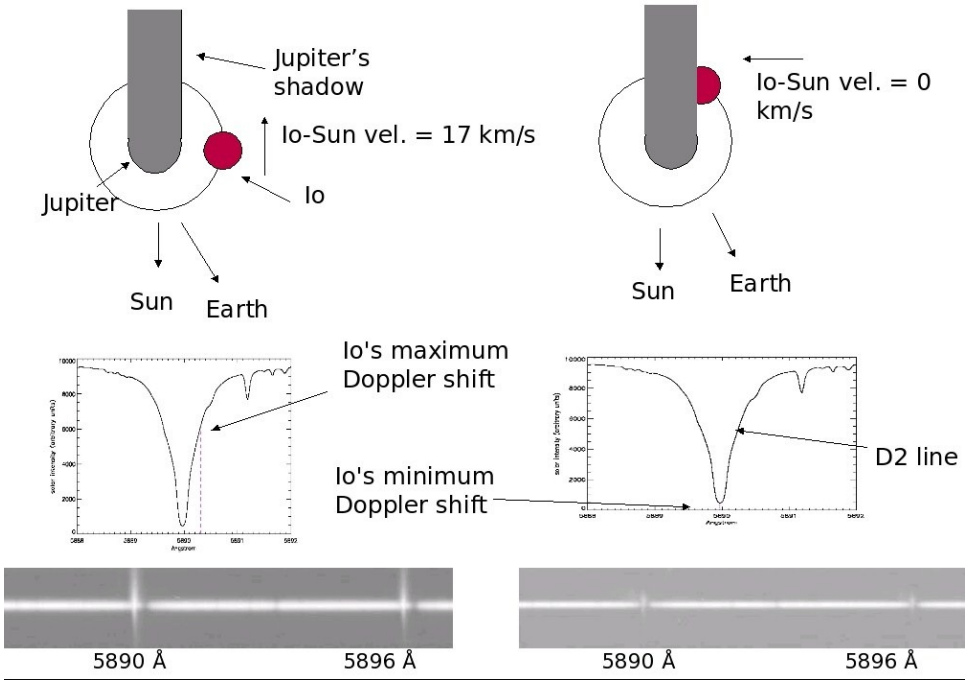

Figure 2.11: If the sodium abundance is constant throughout Io's orbit, its brightness depends only on the orbital longitude. Left part: Io is at western elongation; right part: Io is at superior conjunction. Together with the geometrical configurations (upper part) there are the plots of solar radiance around the sodium D2 line (middle) to show the dependence of the γ-factor from the orbital longitude, and the spectra of Io (bottom), showing the sodium emission being fainter while Io-Sun relative velocity approaches zero.

The optical depth in the center of the D_2 line is

$$\tau_{D1} = \alpha_{\nu_{D2}} N = 2.2 \cdot 10^{-10} T^{-1/2} N \tag{2.5}$$

At 5000 K, $\tau = 1$ corresponds to $N = 6.6 \times 10^{11}\ atoms\, cm^{-2}$ so that, for the neutral cloud at Io, we can consider it optically thin. A measure if its brightness is thus a proxy for the column density.

2.4 The Condensation Hypothesis

It has been stated that ejection to the neutral cloud occurs through the intermediary of the atmosphere, with little or no direct escape from surface. However, the role that the atmosphere plays in the supply of atoms to the neutral cloud is not yet clear: does it hinder the supply of atoms or does it promote escape by placing material at high altitude? A recent controversial result suggests the latter: Morgan et al. (2004) showed that the sodium cloud immediately after the eclipse is less bright than it should be, and reaches the expected values of luminosity hours after the reappearance. One possible explanation is condensation of sulfur dioxide during the eclipse, which would prevent NaCl (possible source of Na atoms) to be released. To test this fascinating hypothesis was the main aim of my PhD period, because those observations have never been published. In fig. 2.12 is depicted the brigthness of the neutral sodium cloud. A non-condensing cloud should follow the black diamonds trend; a condensing cloud will follow the red asterisks trend, that is: starting less bright than the expected soon after the reappearance and reaching the purely geometric trend, which depends only by the radial velocity, some time after the reappearance. The ordinates are intensity at arbitrary units; the abscissae are the orbital longitudes around Jupiter: 0°means superior conjunction, with angles increasing counter-clockwise (90°means eastern elongation).

2.5 Observations

For this purpose, I undertook ground-based observations at italian telescope TNG (Telescopio Nazionale Galileo, $3.6m$ of diameter) at La Palma island, equipped with the high resolution (115000) echelle spectrograph SARG. This instrumental setup proved itself to be particularly suited for spectroscopic observations of planetary atmospheres in the region of the sodium doublet, see e.g. Barbieri et al. (2004). Characteristics of SARG are resumed in Table 2.1.

I used the long slit (26.7×0.4 arcsec) with the Na filter, in order to prevent order overlapping and to better isolate the region of the sodium doublet. I took

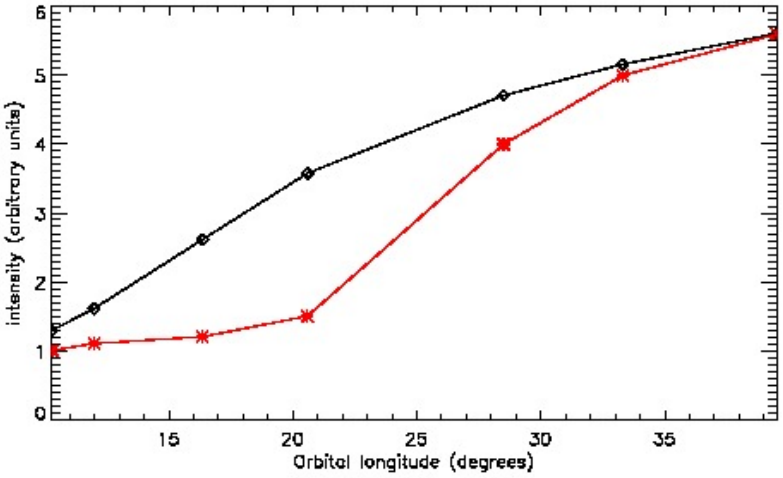

Figure 2.12: The expected brightness of the neutral sodium cloud.

Figure 2.13: The italian telescope TNG.

Table 2.1: SARG main parameters

Spectrograph resolution	115000
Slit length and witdth	26.7×0.40 arcsec
Spectral dispersion	0.022 Å
Pixel scale	0.16 arcsec/pix
CCD dimension	$2k \times 4k\ pixels$

spectra of Io, target of mission, the other galilean satellites (for continuum subtraction), Jupiter (for calibration) and standard stars (for telluric lines removal). The observations (each one night lasting) have been carried on during four different months, from April to July 2007, two nights before eclipse, two nights after eclipse. The geometry of the observations is reported in figures 2.14-2.17, while in table 2.2 I have reported the relevant orbital parameters of Io during the observations.

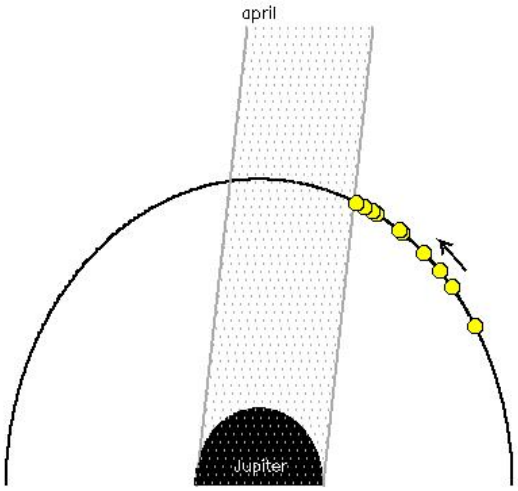

Figure 2.14: Geometry of observations of April (pre-eclipse). The Earth is on bottom of the figure, and the shaded gray area is the Jupiter's shadow. The arrow indicate the direction of Io, whose positions during the observations are indicated by the yellow circles.

Table 2.2: Io orbital parameters for observations at TNG in 2007.

April										
Spectrum:	# 1	# 2	# 3	# 4	# 5	# 6	# 7	# 8	# 9	# 10
Orbital long. (deg)	316	326	330	335	340	342	347	349	351	352
Hel. rad. vel. (km/s)	11.59	9.37	8.25	6.92	5.50	5.01	3.40	2.89	2.38	1.92
Earth-Io vel. (km/s)	-6.52	-8.33	-9.32	-10.48	-11.74	-12.18	-13.65	-14.11	-14.58	-15.02
May										
Spectrum:	# 1	# 2	# 3	# 4	# 5	# 6	# 7	# 8	# 9	# 10
Orbital long. (deg)	316	320	326	328	335	337	345	347	348	350
Hel. rad. vel. (km/s)	11.60	10.84	9.38	8.88	6.89	6.26	4.19	3.57	3.02	2.47
Earth-Io vel. (km/s)	-0.66	-1.31	-2.59	-3.04	-4.83	-5.40	-7.29	-7.87	-8.34	-8.89
June										
Spectrum:	# 1	# 2	# 3	# 4	# 5	# 6	# 7	# 8	# 9	
Orbital long. (deg)	11	12	14	23	25	31	33	41	43	
Hel. rad. vel. (km/s)	-3.66	-4.17	-4.83	-7.26	-7.84	-9.31	-9.85	-11.83	-12.34	
Earth-Io vel. (km/s)	2.78	2.31	1.69	-0.57	-1.11	-2.47	-2.97	-4.77	-5.23	
July										
Spectrum:	# 1	# 2	# 3	# 4	# 5	# 6	# 7			
Orbital long. (deg)	10	12	16	21	28	33	40			
Hel. rad. vel. (km/s)	-3.60	-4.10	-5.38	-6.59	-8.76	-10.00	-11.50			
Earth-Io vel. (km/s)	9.19	8.72	7.54	6.43	4.49	3.39	2.08			

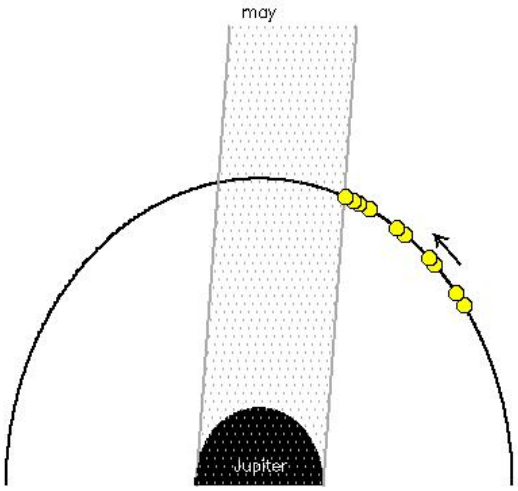

Figure 2.15: Geometry of observations of May (pre-eclipse).

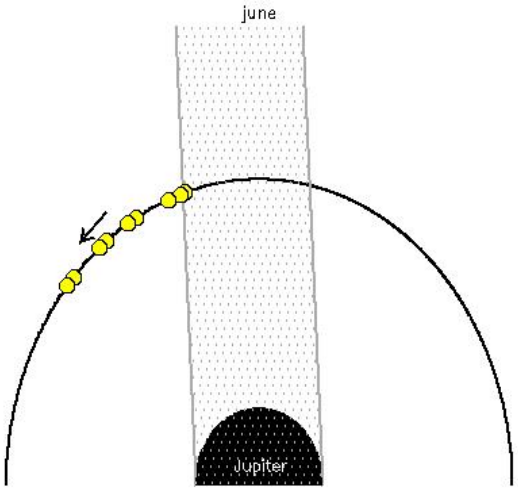

Figure 2.16: Geometry of observations of June (post-eclipse).

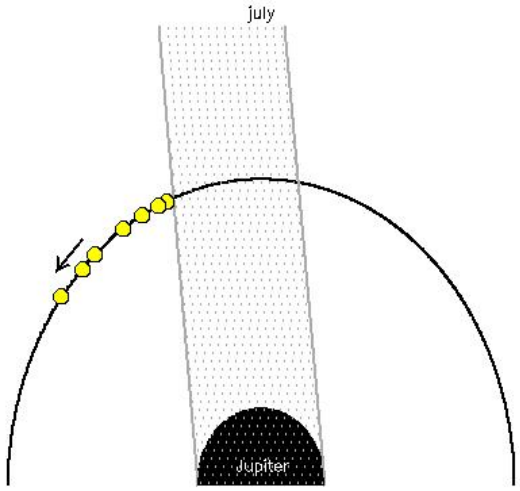

Figure 2.17: Geometry of observations of July (post-eclipse).

2.6 Data reduction

2.6.1 Ordinary data calibration

The first reduction steps are the standard ones required for all spectra, that is: bias removal, flatfielding, calibration in wavelength (see fig. 2.18). For the first two I used IDL routine conceived on purpose, while for the calibration in wavelength I used the IRAF tasks *identify* (to pass the computer a list of reference lines), *reidentify* (for automatic identification of other lines), *fitcoords* (to find the right amount of the shift) and *transform* (to calibrate the spectra).

2.6.2 Telluric lines removal

The removal of telluric lines is essential to this work in order to have a good subtraction of the sunlight reflected from Io. The depth of telluric lines depends on the amount of atmosphere traversed by the line of sight, that is the airmass. An ideal way to proceed would be to observe a star with no intrinsic absorption line at the exact airmass of the target to be corrected for. As standard stars I chose rapidly rotating B stars, so that their absorption lines come nearly uniquely from telluric absorption. Concerning the right airmass, the running time spanned several hours, during which the targets moved on the sky and reached different values of airmass (which depends on the altitude). So I decided to take spectra of standard stars at more than one airmass, in order to have a reference star every

(a) (b) (c)

Figure 2.18: The three ordinary steps of data reduction of echelle spectra. Left: the raw spectrum, the wavelenghts increase downwards and the emission lines are tilted. Middle: the spectrum straightened in the continuum, but with the emission lines still bent. Right: the spectrum straightened and calibrated in wavelength, which changes direction (it increases upwards).

0.25 airmasses, from 1.50 to 2.50, the range of airmasses spanned by the targets. However, it has not been always possibile to use one single star for this purpose. Sometimes it has been necessary to use an "artificial" star, by chosing a weighted mean of two standard stars, whose airmass encompass the airmass of the satellite. Once this star is formed, it is normalized to 1. Finally, the satellite is divided by this normalized-to-one star and its telluric lines are removed. In fig. 2.19 the three different steps of telluric lines removal are displayed..

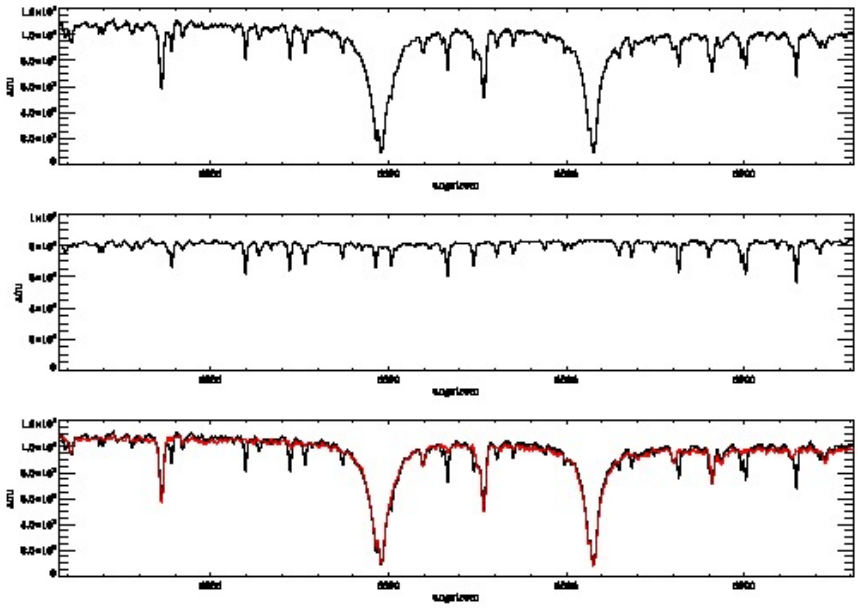

Figure 2.19: Telluric lines removal. Top: original Io spectrum. Middle: normalized-to-one standard star. Bottom: a comparison between Io before (black) and after (red) the telluric absorption correction.

2.6.3 Subtraction of Jupiter's ghost image

Unfortunately, in some cases light coming from Jupiter has been reflected inside the instrument, adding itself to the Io spectra. This light has been removed by scaling the Jupiter spectrum to Io's spectrum, and to move it in the spatial direction until the right Doppler shift is found - see fig. 2.20.

2.6.4 Subtraction of the Io's continuum

For this work on exospheric emission, it was necessary to eliminate the contribution of the disk, that is the sunlight reflected from Io's surface. This is done

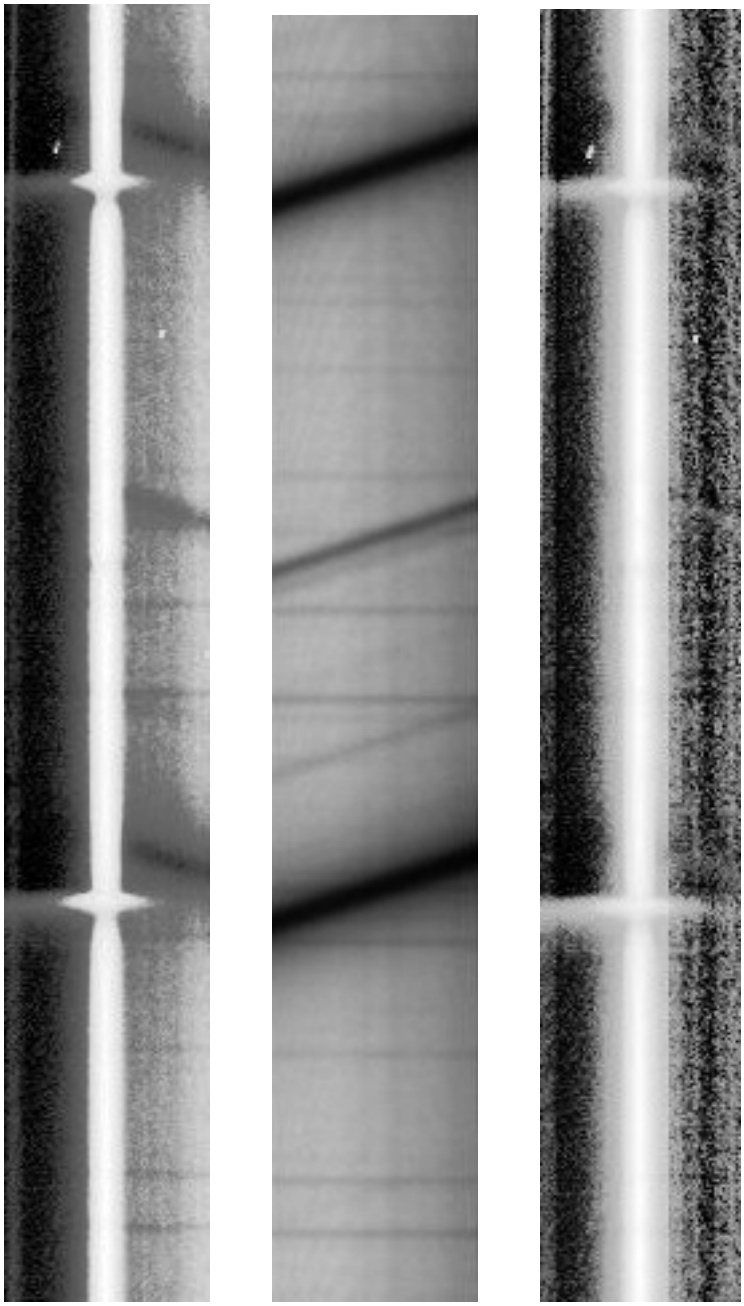

(a) (b) (c)

Figure 2.20: The removal of the ghost spectrum of Jupiter superimposed on Io's one. Left: the original, ghost-affected, Io's spectrum, with the ghost reversed in the wavelength direction with respect to the original Jupiter's spectrum. Middle: the original Jupiter spectrum. Right: the spectrum corrected.

with the sunlight reflected by the other Medicean moons: Europa, Ganymede and Callisto. The reference satellite is first collapsed to 1 dimension, then corrected for the telluric absorption with the method described above, then it is shifted by the amount in pixels corresponding to the difference between radial velocities with respect to Earth of Io and satellite, multiplied for the spectral dispersion of the spectrograph SARG (0.022 Å/pix). Finally, the shifted satellite is then scaled to Io's continuum. The difference between Io and the scaled satellite is performed, giving the exospheric emission. See fig. 2.21, where the three different steps of continuum removal are displayed.

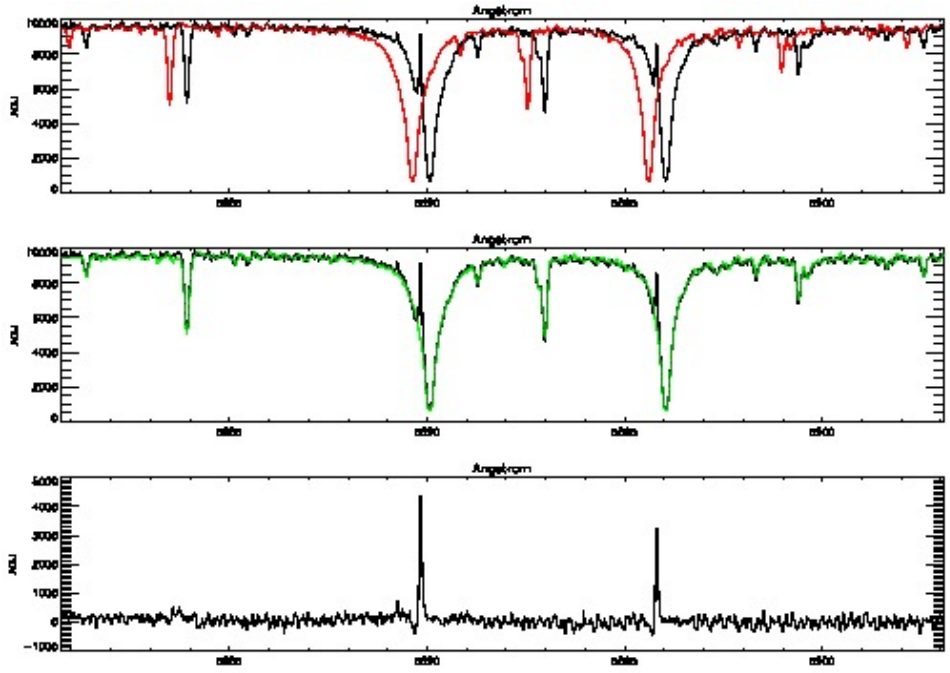

Figure 2.21: Subtraction of continuum. Top: Io spectrum (in black) and the satellite scaled to Io but not shifted (in red). Middle: as before, but with the satellite shifted to match Io's Doppler shift (in green). Bottom: difference Io-satellite, to show just the exospheric emission.

2.6.5 Calibration in Rayleighs

For the calibration in Rayleighs (see equation 2.2) I've used Jupiter itself as a standar candle, because it has a well known brightness of 5.4 MegaRayleighs/Angstrom in the region of the sodium doublet (Brown 2001). I've found the number of counts

ADUs in Jupiter's spectra along 1 Angstrom and divided it for 5.4 MR and for the exposure time of Jupiter spectra (namely, 1 minute). The inverse of this number is what is commonly defined the **calibration factor** (or calfactor), which depends on the instrument and gives the counts in kiloRayleighs corresponding to 1 ADUs in each second: $[calfac] = kR\,s\,ADU^{-1}$. The calfactors so obtained for Jupiter have been interpolated, for each night, for the time of observation of the Io spectra, in order to have a value of calfac similar to the value of the calfac of Jupiter closer in time. In fig. 2.22 calibration factors for pre-eclipse (April and May) and post-eclipse (June and July) observations are reported versus time expressed in hours after 8 pm. The blue asterisks are the calfactors obtained from Jupiter spectra; the red triangles are their interpolation used to calibrate the corresponding Io spectra.

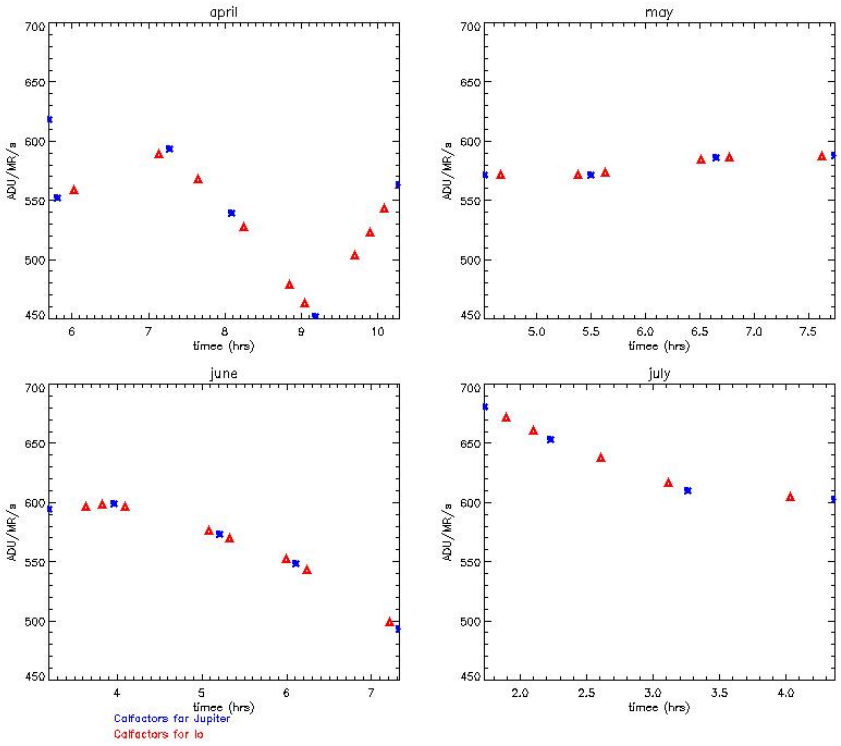

Figure 2.22: Calfactors for Jupiter and extrapolated calfactors for Io.

2.7 Results

In fig. 2.24 I report how a subtracted spectrum looks like after this process. Other features are visible, besides the neutral cloud emissions: the fast jet, the telluric sodium at twilight and the new, unexpected, blueshifted feature (see section 2.9).

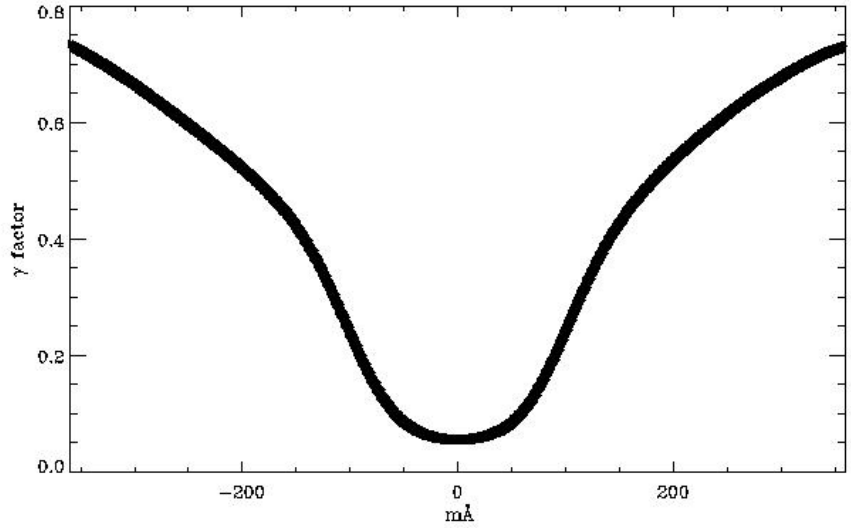

Figure 2.23: The γ-factor for the D2 line.

In the figures 2.25-2.28 I present stacks of reduced spectra of Io. The time increases towards the left, meaning that for April and May stacks, the satellite was entering into Jupiter's shadow. In fact, the neutral cloud appears fainter as time goes by. For June and July stacks, the neutral cloud appears brighter while it exits from Jupiter's shadow.

The red dashed line in figures 2.25-2.28 indicate the wavelength of exospheric emission of sodium at rest at Io. In order to get brightness, I performed a sum over a region that encompasses both the exospheric emissions (D2 and D1). These two regions are delimited by the blue dashed lines in the same figures. I then divided them by the corresponding gamma factors (see fig. 2.23), in order to remove the dependence of the brightness from the orbital position. I reported these data in fig. 2.29.

At this point, the brightness depends only by the amount of sodium in the exosphere, because the neutral cloud is optically thin (see eq. 2.3).

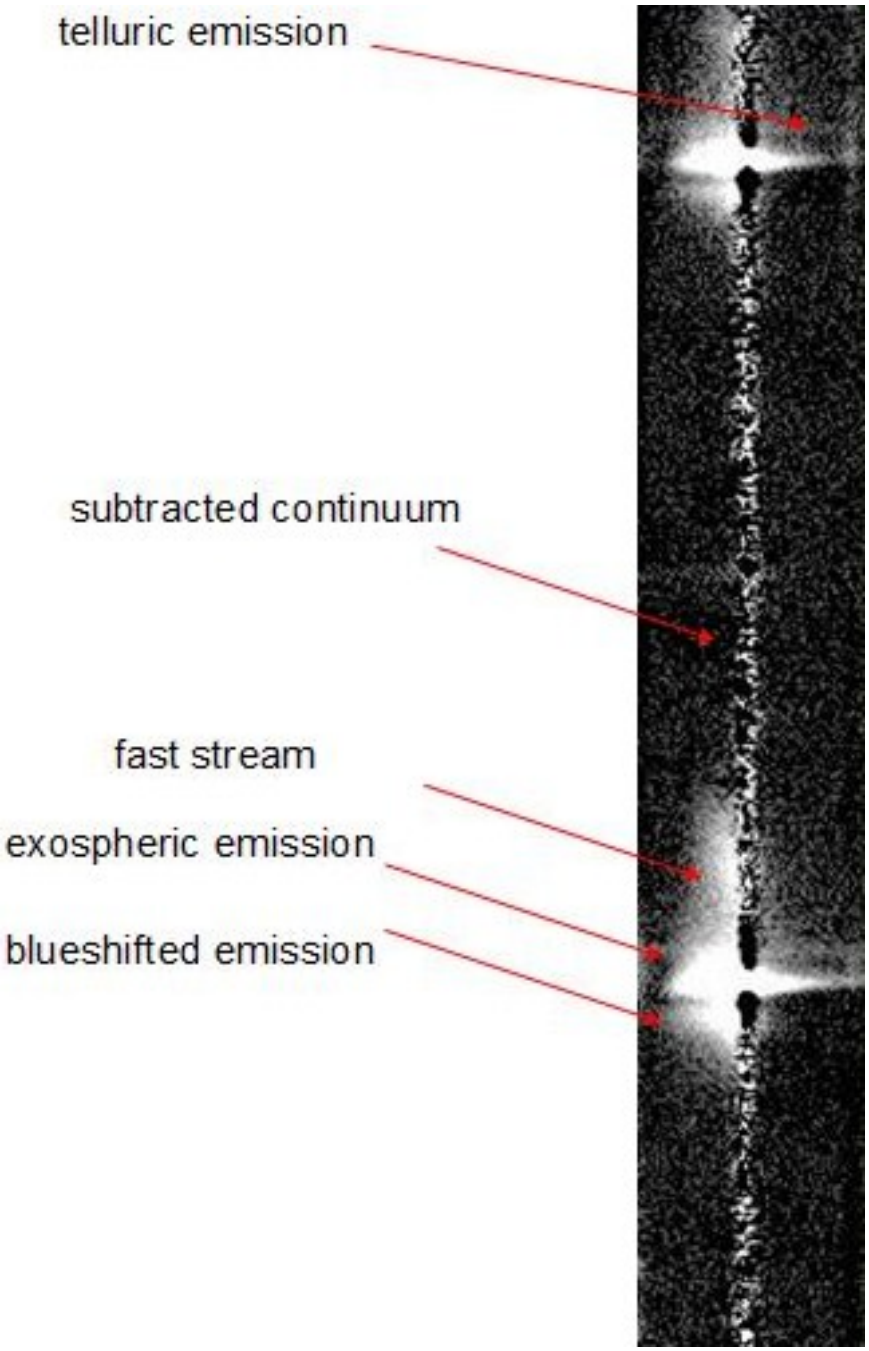

Figure 2.24: An example of a subtracted spectrum. In this month (April), the unexpected emission (section 2.9) is readily visible, among the various emissions - from neutral clouds, fast jet and the telluric sodium layer at 90 km of height brightening at twilight. Jupiter is on the left side.

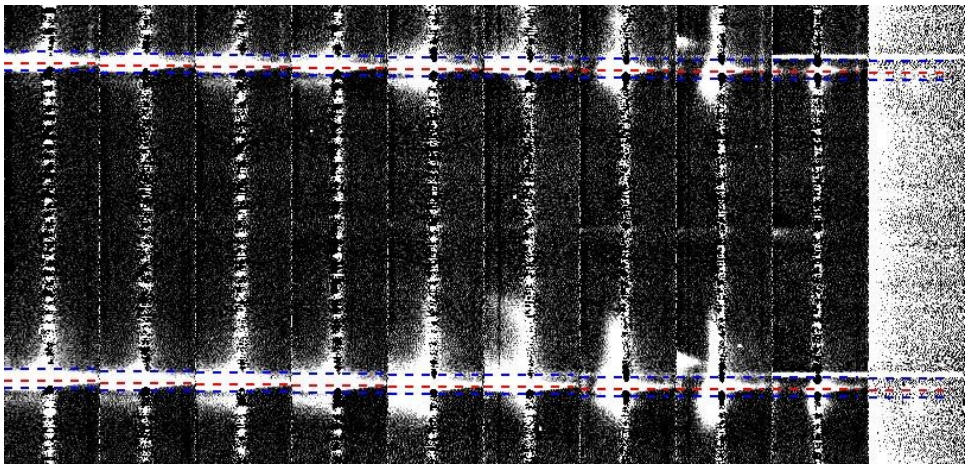

Figure 2.25: Stacks of April, pre-eclipse months. Time increases toward right, wavelengths increase upwards, Jupiter is on the left side.

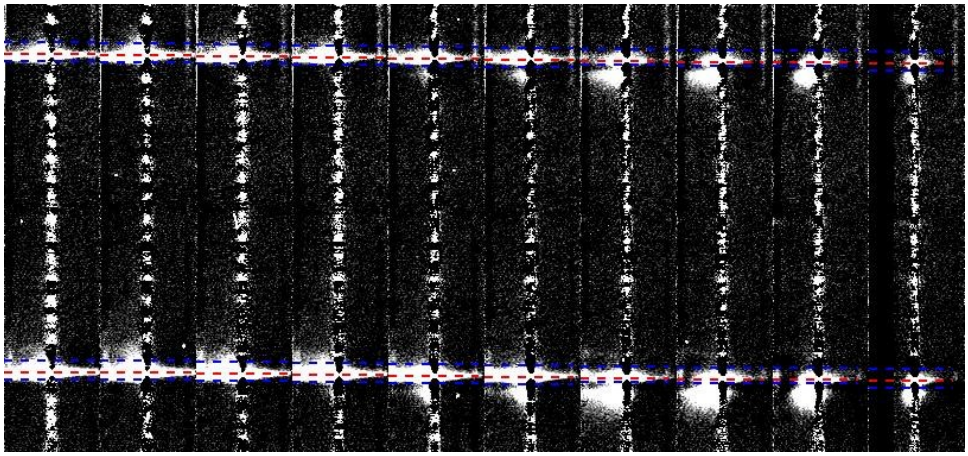

Figure 2.26: Stacks of May, pre-eclipse months. Time increases toward right, wavelengths increase upwards, Jupiter is on the left side.

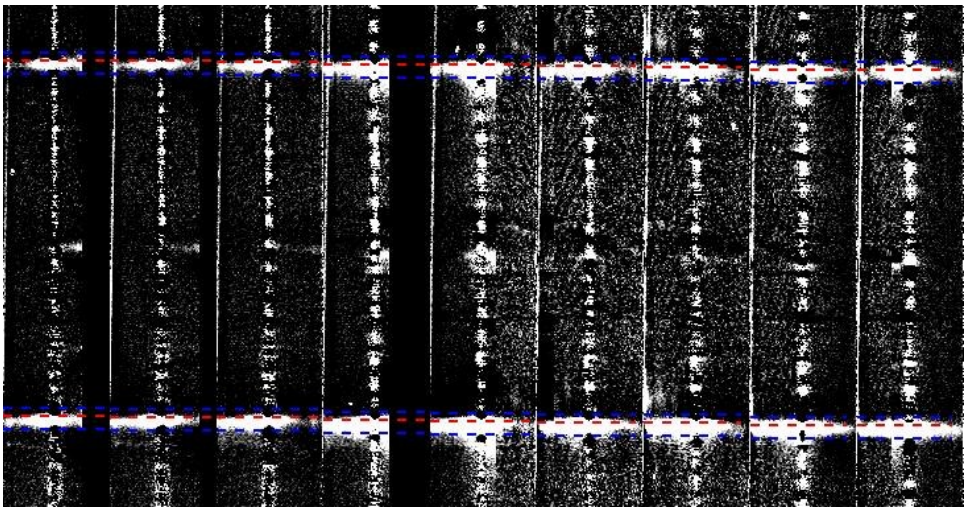

Figure 2.27: Stacks of June, post-eclipse months. Time increases toward right, wavelengths increase upwards, Jupiter is on the right side.

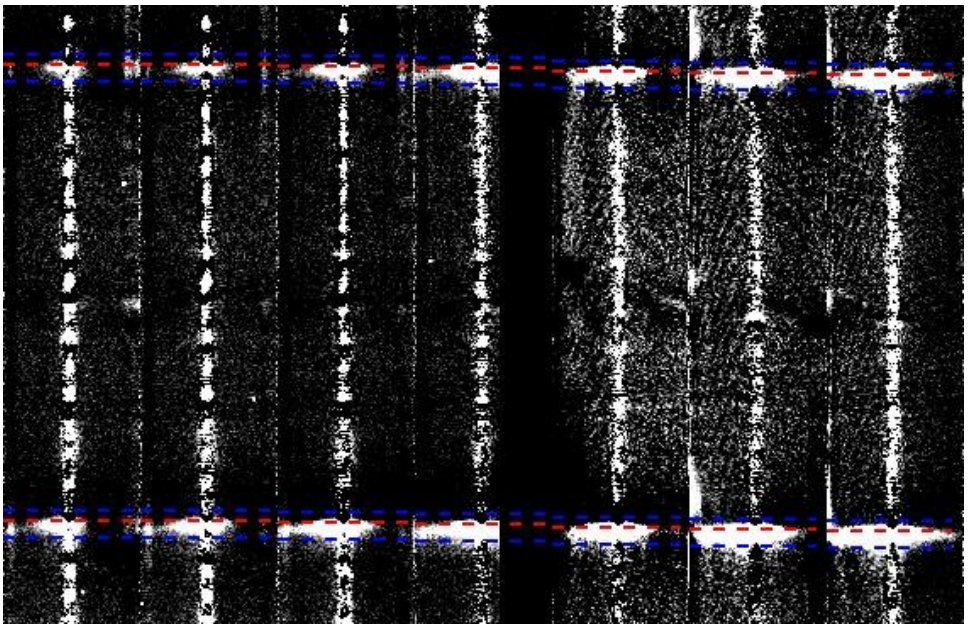

Figure 2.28: Stacks of July, post-eclipse month. Time increases toward right, wavelengths increase upwards, Jupiter is on the right side.

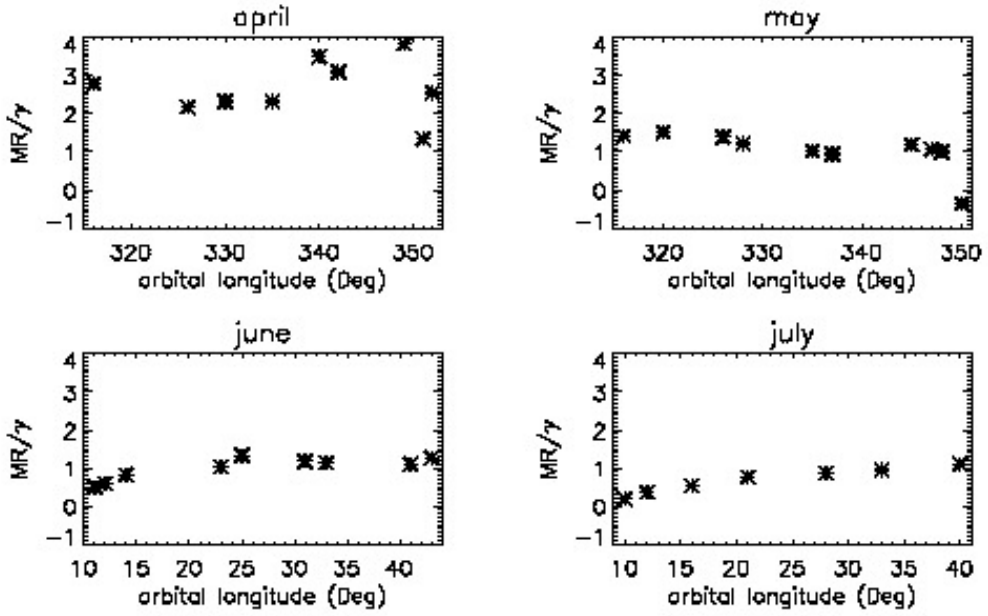

Figure 2.29: The brightness of Io's exosphere as Io approaches Jupiter's shadow (April and May) and as Io leaves it (June and July), divided by the γ-factor. Ordinates are orbital longitudes, starting from superior conjunction (0°) and increasing counterclockwise (i.e. 90°means eastern elongation).

2.8 Discussion

I decided to disregard data of April, because of the high scatter of the points. The trend is all but constant, as expected, and this might be due to the high variability of the calfactor for that month (see fig. 2.22). Probably the night was not photometric. For the remaining three months, the trend is more regular. For May it is fairly constant, as expected for a constant column abundance before eclipse. I discarded the last term of May, because its negative value is by far distant from the mean of other data (see fig. 2.29). However, the great expectations lie in the post-eclipse months: even at a first glimpse, June and July do follow an increasing trend, in contraddiction with constant column density in the neutral cloud. Preliminary results have been published in Grava et al. (2010). I report them here together with a more complete statistical analysis, performed with a chi squared test.

2.8.1 Statistical analysis of post-eclipse behaviour

Given that the majour souces of uncertainties in this case are statistical in nature, and not random, I decided to apply the reduced chi squared test to check whether post-eclipse data are consistent or not with an assumed constant parent function, which is the mean of the data. To find the statistical errors, I imposed a reduced chi value for May of 1.00, because it is fairly sure that May follows a constant trend.

I then applied the same sigma's to June and July. In fig. 2.30, 2.31 and 2.32 I have reported data (red asterisks) together with their errors bars (sigma's). The green dashed line represents the mean of the data (parent function), while orbital longitudes increases counterclockwise starting with 0°corresponding to superior conjunction. I then calculated the chi squared value for these months (Bevington & Robinson 2003):

$$\chi^2 = \sum_{i=1}^{N} \frac{[y_i - f(x_i)]^2}{\sigma_i^2} \tag{2.6}$$

where N is the number of data (N = 9, 9, and 7 for May, June and July respectively), x_i are the orbital longitudes, y_i are the data, $f(x_i)$ is the parent function to test (i.e. the mean of the data), and σ_i are statistical errors calculated from May data. The *reduced* chi squared is calculated dividing eq. 2.6 by the number of degrees of freedom (DOF) $\nu_1 = N - c$ where c is the number of contraints. As the parent function is a constant, it has only one parameter, or constraint ($c = 1$), so the number of DOF is ν_1 = 8, 8, and 6 for May, June and July respectively. The reduced chi squared values are 1.00 (by definition), 2.02 and 2.57 for May, June and July respectively. The terms larger than 1 of the post-eclipse months mean

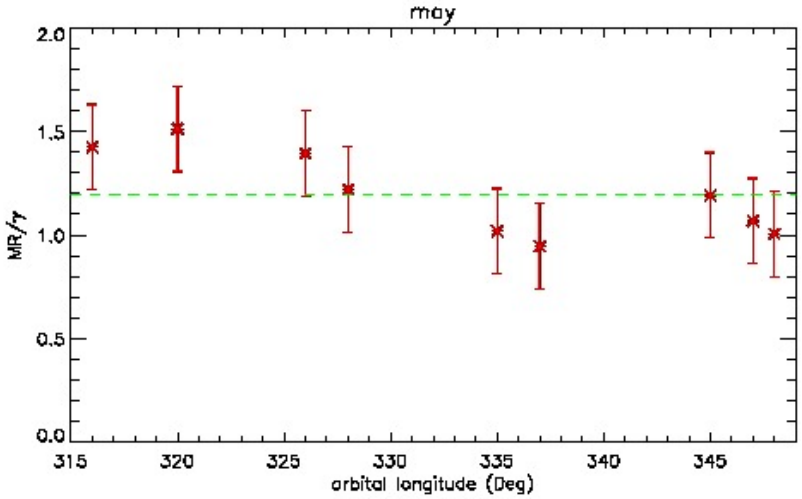

Figure 2.30: Data for May.

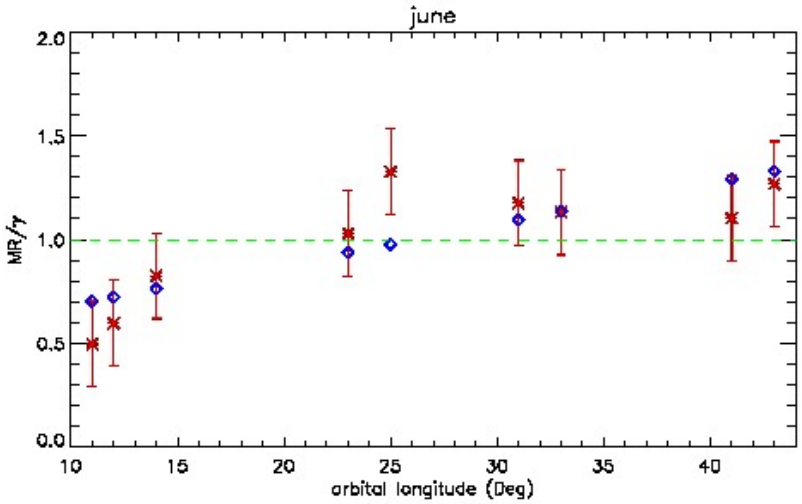

Figure 2.31: Data for June.

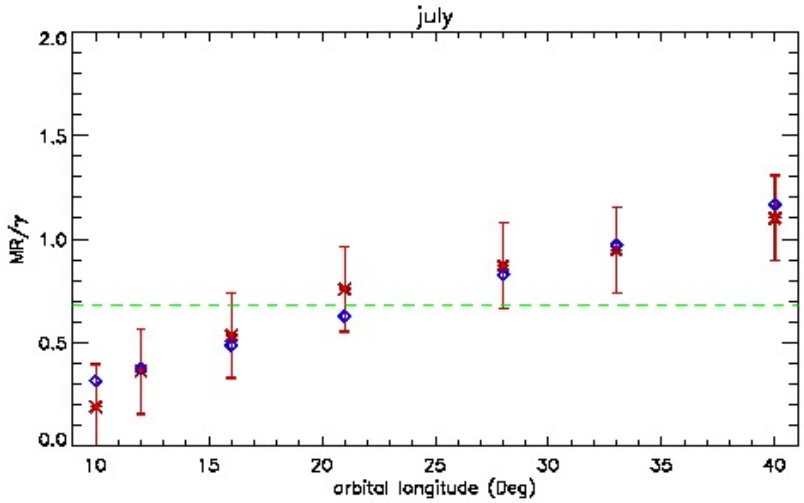

Figure 2.32: Data for July.

a bad fit of the parent constant function. To constraint the confidene level of the inconsistency of data with this null hypothesis, I calculated the Probability to Exceed (PTE), that is the probability that a random set of N data point drawn from the parent distribution would yield a value of chi squared equal to or greater than the one calculated from the data. The PTE depends upon this latter and upon the number of DOF, and the calculation is performed by the routine *chisqr_pdf* of IDL. I obtained, a PTE of 3.98% and 1.73% for June and July, respectively. This means that the null hypothesis of constant parent function is inconsistent at the confidence level of 95% for June and 99% for July.

I then performed a F test for an additional parameter, to check whether it should included in the parent function. I've fitted the data with a straight, increasing line (blue diamonds in fig. 2.31 and 2.32) and I've calculated the reduced chi squared value with respect to this new parent function. Given that this latter has one more parameter (the slope) than the constant used before, the number of DOF is decreased of 1, yielding values of $\nu_2 = 7$ and 5 for June and July respectively. The new reduced chi squared values are 0.81 and 0.20 for June and July respectively. At this point, I've calculated the F number:

$$F_\chi = \frac{\chi^2(c_1) - \chi^2(c_2)}{\chi^2(c_2)/\nu_2} \tag{2.7}$$

where c_1 is the number of constraints from the constant parent function ($c_1 = 1$)

and c_2 is the number of constraints from the linearly increasing parent function ($c_2 = 2$). This statistic follows the F distribution with 1 and ν_2 degrees of freedom. It should be large if the additional term improves the situation. I've obtained F_χ of 13 and 72 for June and July respectively. The PTE in this case is 0.85% for June and 0.04% for July, meaning that an additional parameter (the slope) is required with a confidence level higher than 99% for both months. This is the quantitative proof that the data of post-eclipse months are inconsistent with the null hypothesis of constant column densities, at a highly significant (i.e. 99%) level.

2.9 Unexpected Results

During the reduction steps of this work, two unexpected features have been observed.

The first one is an escape process, an ejection feature blue-shifted (i.e. directed towards Jupiter) of tens of $km\,s^{-1}$ with respect to Io, observed only in the pre-eclipse months. As seen in fig. 2.33, this new feature is not an artifact, being present also in the original, raw spectra, but was clearly visible only after the delicate subtraction. In fig. 2.34 is reported the Doppler velocity of the new

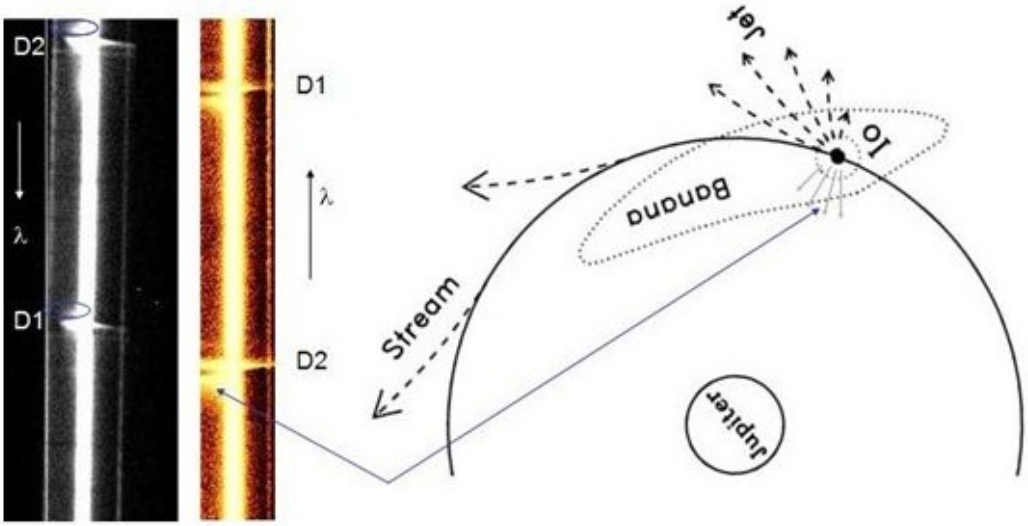

Figure 2.33: The unexpected emission (indicated by the blue arrows) was visible also on the raw, original spectra (left, in gray), but became clearly visible after the delicate subtraction (spectrum on the right, with wavelength direction reversed due to calibration).

feature compared to the peak emission of the first spectrum.

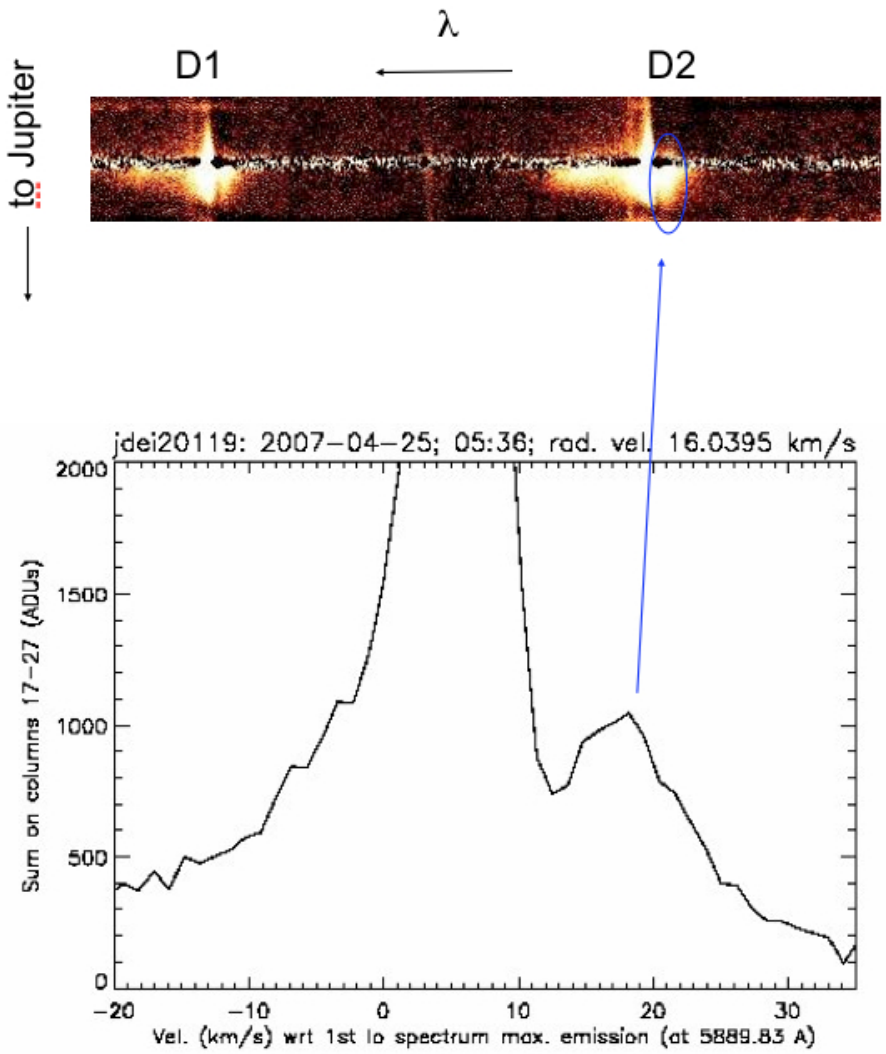

Figure 2.34: The intensity of the blueshifted emission of Io (indicated by the blue arrow) is plotted against velocity (the reference is the position of exospheric emission peak in the first spectrum of the night). Positive velocities mean blue shifting. This spectrum is the 7^{th} of the first observing run (figure 2.14).

Unlike the slow sodium of the banana cloud, the velocity of this new feature ($> 10 km\, s^{-1}$) suggests a source process due to electrodynamic interactions, similar to Io's jet or stream. However, the Jupiter-ward direction of this new feature suggests it does not have the same source mechanism as the jet, which ejects opposite Jupiter. The non-detection of a similar feature in the post-eclipse spectra suggests that the source mechanism is inhibited by atmospheric collapse or by a change in photoionization. Modeling of this new feature has already started. This may be the first new escape process discovered in the jovian system in 20 years, enabled by TNG/SARG's high spectral/spatial resolution and sensitivity, and it could also have possible ramifications for other moons, Mars, Venus and the extrasolar planets.

The second unexplained feature that has been discovered later is an absorption in the same side of the Fraunhofer line where the exospheric emission lies. It has been discovered due to the presence, in the subtracted Io spectra, of dark, negative "beads" slightly "bluewards" of the exospheric emission - see fig. 2.36. This is due to the mismatch between the two blue side of the Fraunhofer line of the satellite and that of Io. This is indeed unexpected, because no sodium is predicted to be present there. A similar effect may be produced by the optically thick layer of sodium lying at the surface, but the Doppler shift, although small, demonstrates that this absorption is not at Io's rest. In fig. 2.35 I report the spectral profile of the subtracted continuum at Io (in black) together with the satellite[1] (in orange) scaled to it in order to subtract the continuum. The subtraction, in blue, shows clearly an absorption "bluewards" of the main exospheric emission. The connection between this unexpected absorption with the unexpected emission is tempting. Both are seen on the blue side of the absorption line, both are seen only in the pre-eclipse spectra. However, the Doppler shift between the twos is different, the emission being faster than the absorption (see fig. 2.36). It is true, however, that the emission lies far from the disk, while the absorption appears to be more closer to the disk, and this may be two manifestations of the same process, acting both in the atmosphere and in the neutral clouds. A modelization of both these features has started. Anyway, in order to further investigate these discoveries, we requested an additional observing time at TNG. This was granted to us and we came back there two years later. This time we decided to consider also Europa as a target (and not as a mere reference satellite) because we were assigned 7 consecutive half nights that gave us the opportunity to observe both satellites in the four quadrants. The details of these new observations and their preliminary results are resumed in section 4.2.1 and 4.2.2.

[1] Actually, in order to have a reference spectrum as uniform as possible, this is indeed an average of satellites spectra.

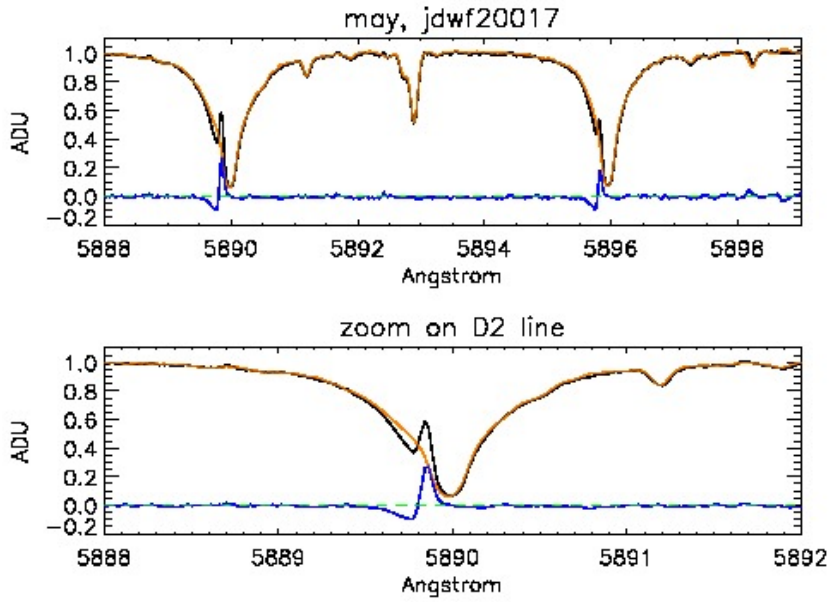

Figure 2.35: Spectral profile of Io (in black) and of the satellite (in orange) shifted and scaled to it. The wide spectral range shows how the match between the two spectra is perfect in the central solar Nickel line. A zoom on the D2 Fraunhofer absorption line reveals the mismatch on the blue side, bluewards of the exospheric emission. The subtraction between the two spectra is the blue line, and clearly shows the unexplained feature as a negative absorption (green dashed line marks the 0). Satellites have been normalized to 1 for a better comparison. Here, Io is the 6^{th} spectrum of second night, see fig. 2.15.

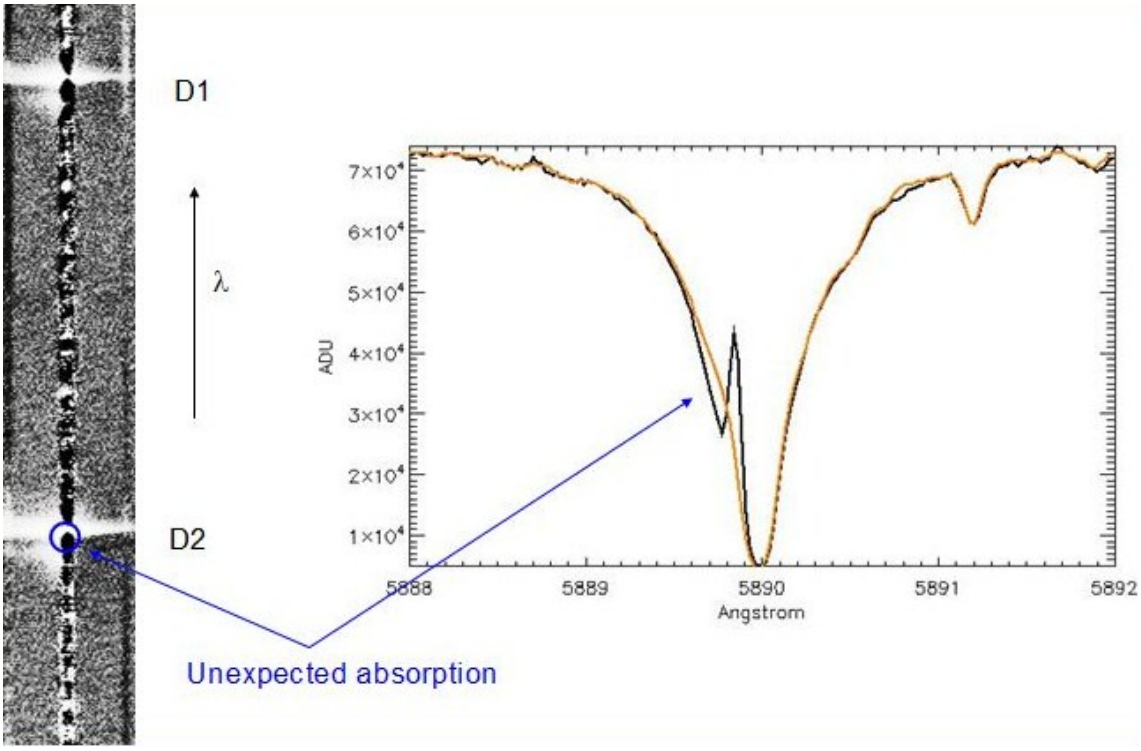

Figure 2.36: The unexpected absorption. On the left, the spectrum with wavelengths increasing upwards, Jupiter being on the left side. The negative, dark "beads" led me to the discovery of this unexplained absorption at Io's disk.

2.10 Conclusions on the work on Io

This work shed new light on the role that the atmosphere of Io plays in the transport of sodium atoms from the surface to the neutral clouds, and on the surface-atmosphere interaction of Io's volatile SO_2 on timescale of hours after emergence from eclipse. If an additional parameter must be introduced at a high confidence level in order to explain the brightness after eclipses, it means that the SO_2 atmosphere condenses at the surface during the period of eclipse (~ 2.5 hours) behind Jupiter. This in turn implies that sodium-bearing molecules (such as $NaCl$), that are the source of sodium atoms in the surface, are sticked at the surface by the condensed atmosphere during the eclipse, and released some time (i.e., hours) after the reappearance.

This is the first time a similar effect is observed. A post-eclipse brightening of the Io atmosphere was first observed photometrically by Binder & Cruikshank (1964) who detected an anomalous brightening of Io by about 10% for 10-20 min following the emergence, however this was due to frost coverage and not by lack of atoms in the neutral clouds. Recently, Cruikshank et al. (2010) observed the atmosphere of Io using infrared telescope, but they found no changes in the appearance of the SO_2 absorption bands, within $60 \div 90$ min from the reappearance. This can be due to the short time interval spanned by their observaions. On the contrary, our time interval was quite long, reaching some hours after the reappearance, enough for the effects of sublimations to be visible.

3

Mercury

With a radius of 2437 km, Mercury is the smallest of terrestrial planets, but is one of the most interesting and at the same time one of the less understood. Its uncompressed density (5.43 $g\,cm^{-3}$) is the highest of the Solar System. This suggests that Mercury has an disproportionately large iron core (1840 km), which occupies 42% of its volume, whereas the iron core of the Earth makes up only 17% of its volume. On the other hand, the silicate mantel must be correspondingly thin (600 km). The reason for this is not yet clear. Three hypothesis have been proposed: chemical differentiation of the protoplanetary disk, erosion of silicate mantle by solar wind soon after Sun had formed, or collision with a large body (e.g. a planetesimal) which caused silicate mantle to be ejected away. However, each of these hypothesis appears contraddictory with the presence of Na and K in Mercury's exosphere, because they predict a very low concentration of volatile elements. Because of its proximity to the Sun, it was not until the 70's that Mercury could be studied thoroughly, thanks to the 3 fly-bys of Mariner 10 (1974 and 1975). For the first time the surface has been imaged, which looked similar to that of the Moon, covered with several impact craters. The "real" surface is buried by a layer of regolith several meters thick, composed of rock fragments and impact glass of the overlapping ejecta blankets associated with impact craters (see fig. 3.1). Mercury suffered the same intense bombardment in its early history than the Moon. The impact craters are not uniformly distributed because some regions have been resurfaced by the eruption of lava flows. The resulting lava plains are only sparsely cratered, indicating that the volcanic activity occurred after the period of intense bombardment, that ended at about 3.8×10^9 years. The largest impact crater on the surfaceo of Mercury is the Caloris Basin. It has a diameter of $\sim$ 1300 km and the outermost rings forms the Caloris Mountains that are up to 2 km high. The Caloris Basin resembles tha Mare Orientale on the Moon. The antipodal area of Caloris Basin contains closely spaced hills that may have formed by seismic waves released by the violent impact of the meteoroid that

carved out the Caloris Basin. The most recent episode in the geologic history of Mercury was the formation of scarps called *rupes*, that cut across craters as well as the inter-crater lava plains. The Discovery scarp extends for $\sim 350\,km$ and is up to $3\,km$ high. This and other scarps formed by compression of the crust that may have resulted from the shrinking of the iron core as it cooled and or/by large impacts on the surface of the planet. Scarps of Mercury are crustal fractures along which there is vertical displacement. Therefore, scarps can be classified as a special type of fault that has not been observed on the Moon or on the Earth. The scarps have been preserved on Mercury because of the absence of an atmosphere which has prevented erosion and redeposition of weathering products.

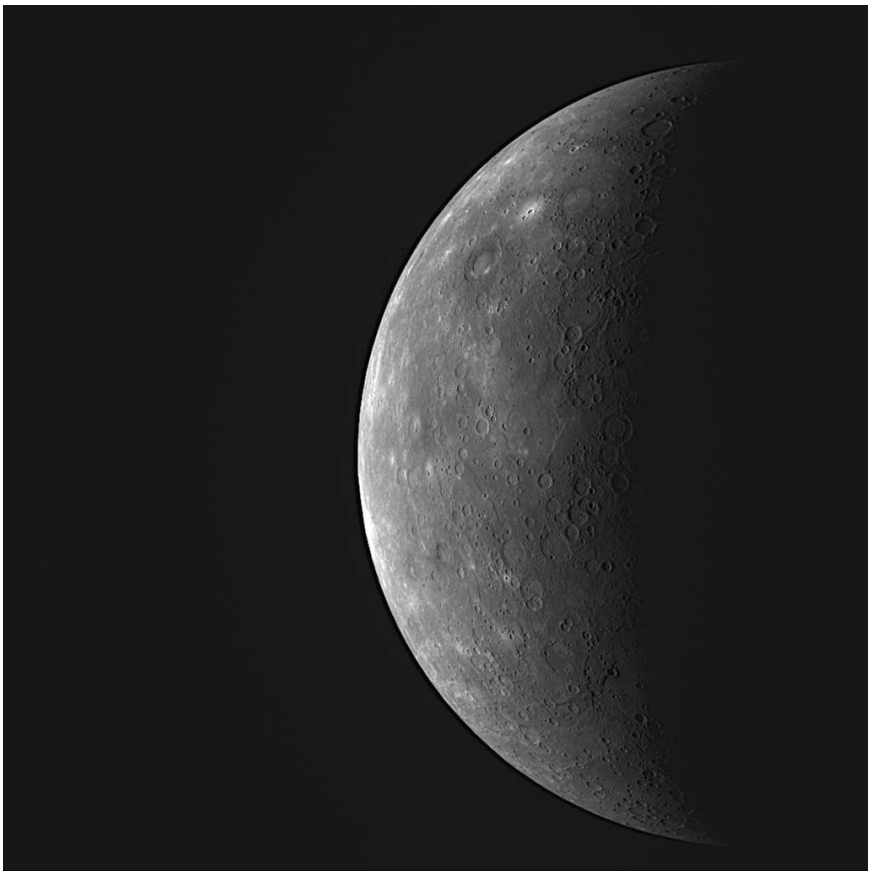

Figure 3.1: Messenger's picture of a region of Mercury's surface which has been imaged for the first time (credit: NASA).

Another outstanding discovery of Mariner 10 was the intrinsic magnetic field at Mercury. Although weak (1% of that of the Earth), this magnetic field is however unexpected, because, according to dynamo theory, planetary magnetic fields are

generated by electrical currents flowing in the iron-nickel cores of rotating planets. This doesn't seem applicable to Mercury case for two reasons:

1. its core is thought to be solid, because the Surface-Volume (S/V) ratio is between that of Moon and Earth. The S/V ratio is related to the cooling rate, because amount of heat lost by radiation from a planet depends on its surface area per unit volume. The high S/V ratio for Mercury implies a high cooling rate which has caused iron core to solidify and has lowered the internal temperature sufficiently to prevent volcanic activity at the surface.

2. the planet rotates very slowly, with a period of ~ 58 days.

The observation that Mercury has its own mangetic field suggests that some part of metallic core is liquid, because the magnetic field cannot be generated by a solid core: solid iron which is magnetized loses its magnetism when temperature reaches 770°C (the Curie temperature of the iron), and temperature in the core of Mercury is supposed to be higher. A solution may be a refinement of dynamo theory, that allows that convection currents may arise from buyoancy of liquid iron due to differences in temperature. Other, weaker, hypothesis suggest that melting temperatureor the iron is lowered by presence of other elements with a lower melting temperature (as Cu, Pb, Zn, S), or that iron core of Mercury is heated by decay or radioactive atoms of U and Th.

3.1 Mercury's exosphere

Mariner 10 discovered also a very tenuous atmosphere at Mercury. Given the very low pressure (1 picobar) and thus the absence of collisions among the species, Mercury's atmosphere is an exosphere, whose exobase coincides with the surface, contrary to Io. Its composition and behaviour depend thus from interactions with the magnetosphere and the surface. The exosphere is not stable on timescales comparable to the age of the planet, so there must be sources for each of the constituents. Seven constituents are known at present to form Mercury's exosphere: H, He, O (discovered by Mariner 10), Na, K and Ca (discovered by ground-based observations) and Mg (discovered by Messenger). Again, like the case of Io, sodium is only a trace element, but is by far the preferred tracer for ground-based spectroscopists thanks to its high cross-section for resonant scattering and thus to its high intensity emission (see section 2.3). Other constituents are expected to be present in Mercury's exosphere, as the pression of the exosphere is 2 orders of magnitude higher than the sum of species known to exist so far. Hydrogen and helium come from solar wind, but they are released in the exosphere from the surface by thermal desorption. Na, K, O and Ca come from surface sputtering,

while H and He have their origin in the solar wind, and are released from surface after having been implanted there and neutralized by recombination.

3.1.1 Spatial distribution of sodium

As sodium is a great tracer of dynamics of Mercury's exosphere, it is not surprising that the "hermean community" has focused their observations in the region of its D-lines doublet. Sodium is not uniformly distributed in the planet, as it would be in the case of a classical exosphere. Strong variations in exospheric characteristics have been observed as function of local time, solar distance and level of solar activity, and correlations between atmospheric Na and K enhancements and surface features have been suggested. See for example fig. 3.2 from Potter et al. (2006) where intensities (right ordinates) and equivalent width (left ordinates) are plotted against angular distance from center of planet. The dashed line is the surface continuum while the solid lines are D2 and D1 exospheric emissions. In the two upper panels, the scan is performed along the north-south direction. Fig. b) clearly reports an enhancement in the northern hemisphere, while in fig. a) values of emission in the northern and southern hemisphere are similar. In the lower panels, the scan is performed along the limb-terminator line. In fig. c), the dusk terminator was in view, and there is a clear increase approaching the limb. Here, sodium is non existent at dusk terminator. In fig. d), the dawn terminator was in view, and there is a decrease of 30% in intensity from limb to dawn terminator.

Another example of uneven spatial distribution of sodium is in fig. 3.3, from Potter & Morgan (1990). Images have been taken at different times, looking at different surface longitudes (nearly the opposite side of the planet) and with different terminators in view (dusk in July, left image; dawn in August, right image). However, high latitude enhancements are present (plus minor excess at the susbolar point) with similar peak values: (3.8 MR for July, 1.2 MR for August). Another intriguing explanation to the north-south excess sodium has been proposed by Sprague et al. (1997), who showed a correlation between excess of sodium at high latitudes and presence of radar-bright spots B and A[1]. The next year, Sprague et al. (1998) observed an exceptionally high emission value, corresponding to a column content of $1.5 \times 10^{11}\, atoms\, cm^{-2}$, at a location close to the Caloris Basin. These authors suggested that these regions were rich in sodium as a result of geologic process. This fascinating hypothesis was however questioned years later, when Potter et al. (2006) measured the ratio of north to south emissions, and

[1]These regions, discovered by Goldstein (1970) have been used to argue for the presence of condensed volatile species in a manner analogous to that suggested for permanently shadowed regions on the Moon. These areas have been attributed to H_2O ice (Harmon & Slade 1992) or to cold silicate minerals (Starukhina 2000).

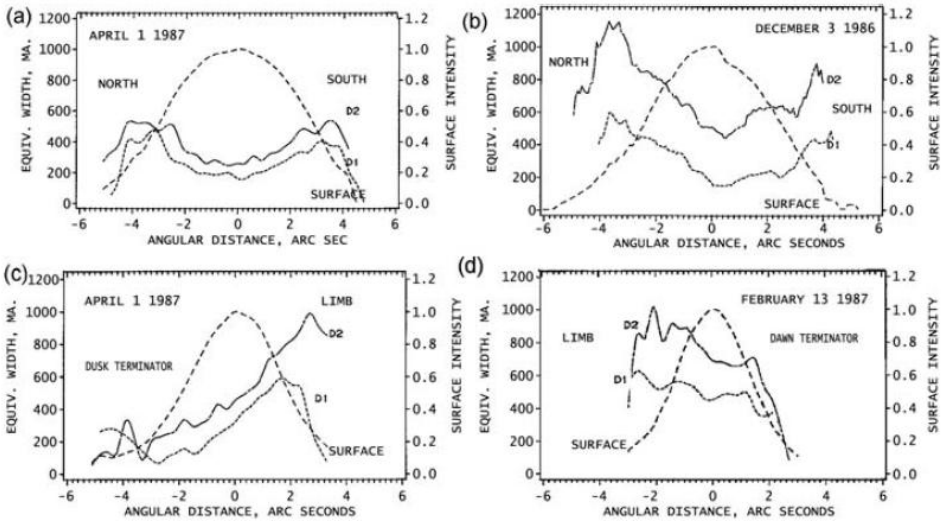

Figure 3.2: Profiles of sodium emission (solid lines) and surface continua(dashed lines) across Mercury.

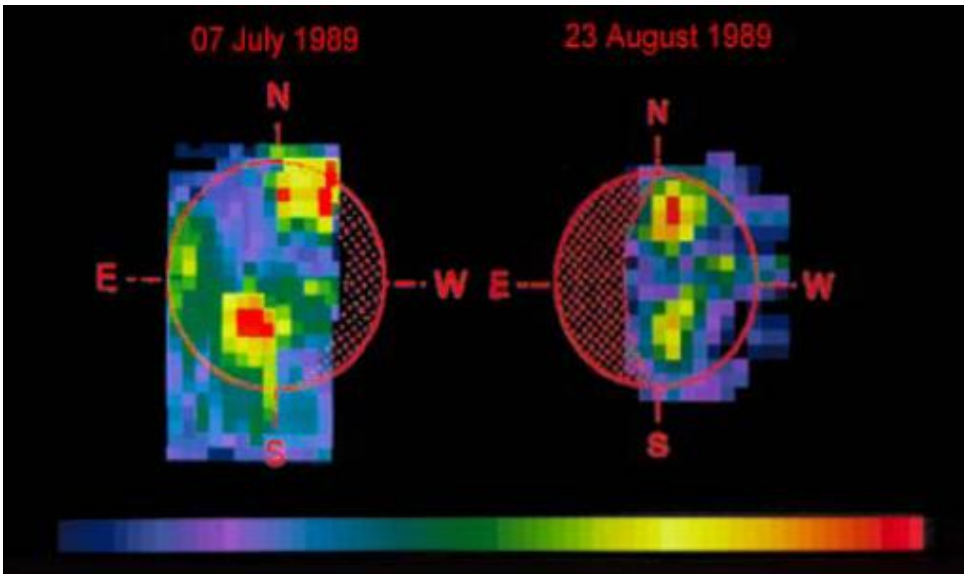

Figure 3.3: Maps of sodium emission from Mercury.

didn't found any correlation with longitude, see fig. 3.4. Rather, images measured

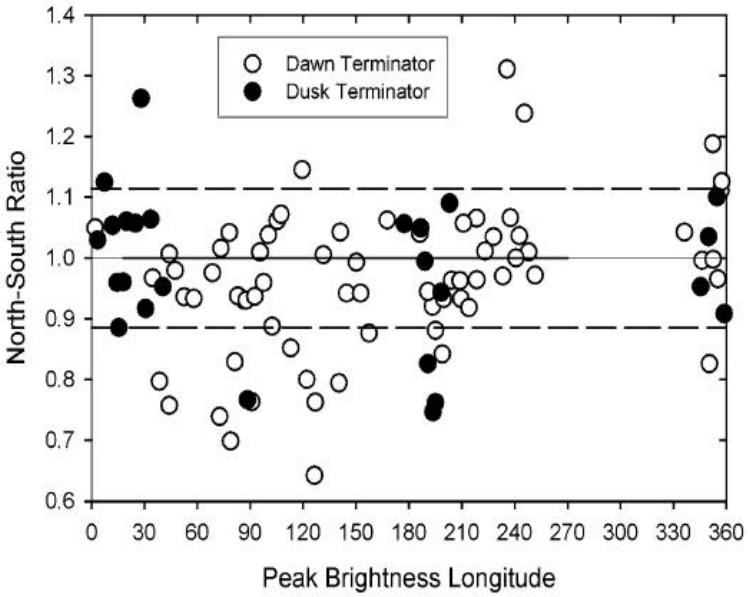

Figure 3.4: North-south hemisphere emission rates. Filled points were data taken when dusk terminator was in view, while open points are data taken when dawn terminator was in view. No particular enhancements were seen when Caloris Basin (longitude 170°) and other radar-bright spots (longitude 355°for both) were in view.

at high values of radiation acceleration almost always showed bright spots in both hemispheres. Ip (1990) modeled the effect of solar radiation pressure on planetary sodium distribution, and showed that high values of radiation acceleration would push atoms towards the terminator. At the poles, terminator and bright limb meet, so that limb brightening occur, enhanced by sodium pushed to the terminator by radiation acceleration.

North-south excess emissions appear sometimes even when solar radiation pressure is relatively low, as showed by Schleicher et al. (2004) who imaged Mercury's sodium exosphere during the solar transit. They found almost no sodium in the dusk hemisphere, as can be seen in fig. 3.5.

3.1.2 Temporal variation in exospheric sodium content

Also temporal variations have been shown to occur at Mercury. Obviously, as it is impossible to observe Mercury for more than half an hour from ground-based telescopes due to its proximity of the sun, diurnal variations are recorded

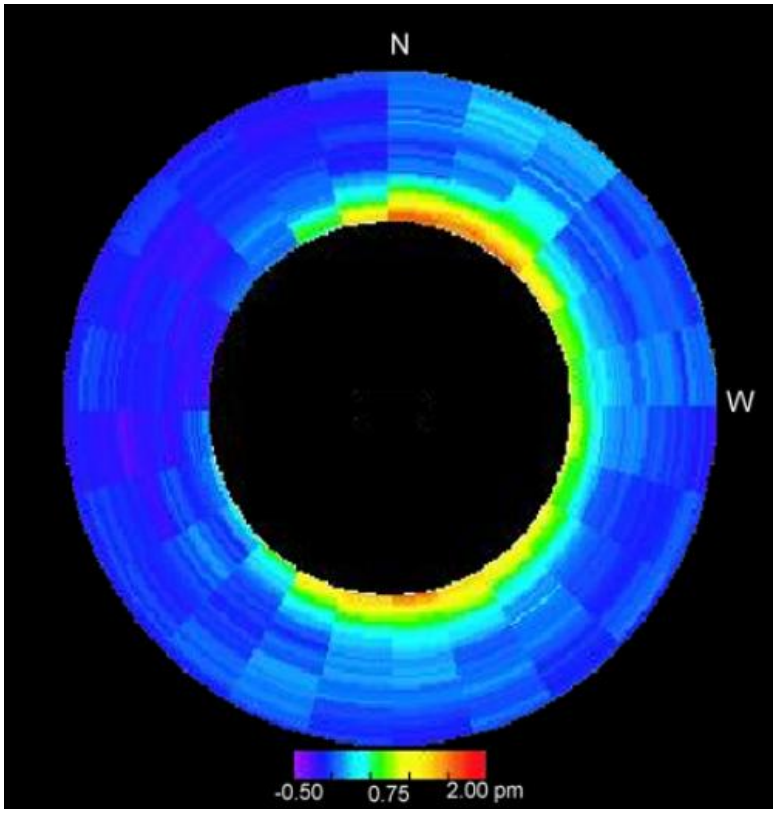

Figure 3.5: Distribution of sodium at Mercury during solar transit of 2003. Here, dawn terminator was in view, therefore dusk hemisphere is on the left.

as differences between terminator (dusk or dawn) and limb. Sprague et al. (1997) have reported that sodium abundance in the morning is about 3 times sodium abundance in the late afternoon - see fig. 3.6. It is natural to think about the

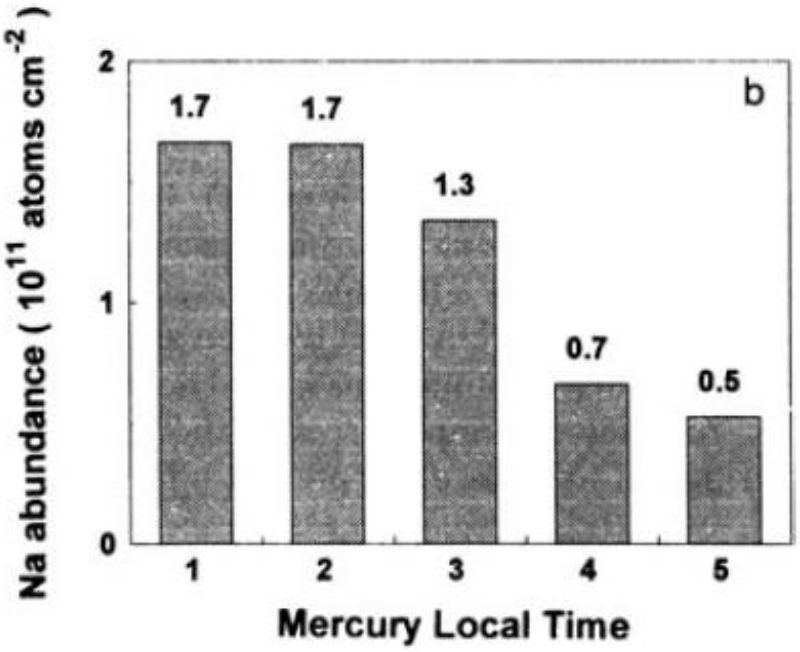

Figure 3.6: Sodium abundance versus local time at Mercury: 1 means early morning, 2 means mid-morning, 3 mid-day, 4 mid afternoon and 5 late afternoon.

evaporation of cold-trapped and ion-implanted sodium as the cause for this effect, and this was proposed by these authors. However, Potter et al. (2006) reported terminator-to-limb ratios for dusk and dawn views, and plotted them against TAA, which is also a proxy for solar radiation pressure(see section 3.4.1). Fig. 3.7 shows these ratios together with the trend of radiation pressure. The drop of "dawn ratios" (black points) at $TAA > 140°$is inconsistent with the hypothesis of thermal evaporation of sodium near terminator, because at aphelion ($TAA = 180°$) the terminator advancement is at maximum (3.38 deg/day) and hence maximum should be the amount of sodium available for thermal desorption. Rather, this minimum suggests a correlation with solar radiation pressure, given that this latter is also minimum at this true anomaly angle (green line).

Finally, daily changes of sodium content have been detected, e.g. Potter et al. (1999). The cause of this variation is unknown, but their episodic nature suggests some connection with solar activity, or heating of the surface. These author suggested a possible correlation with Coronal Mass Ejections, given the high num-

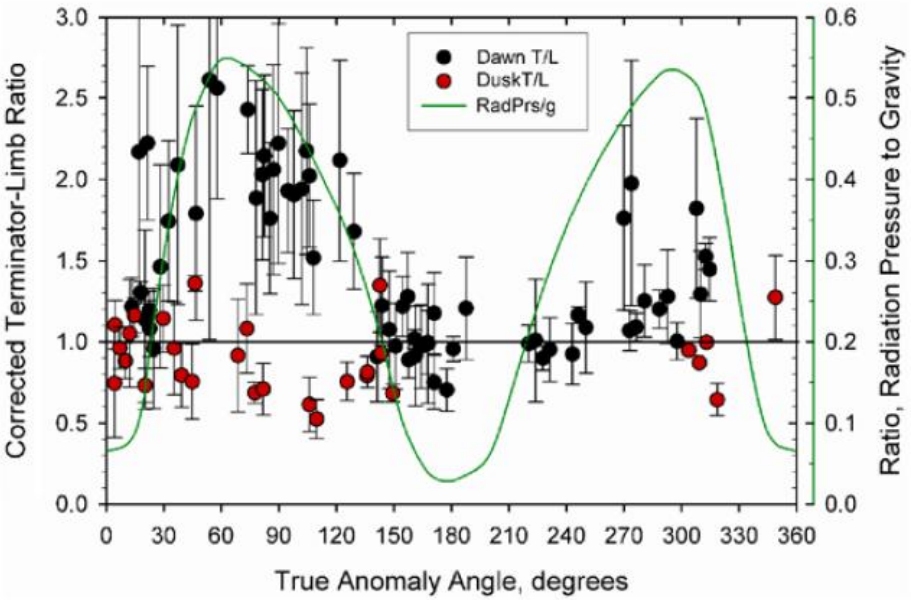

Figure 3.7: Terminator-to-limb ratios (left ordinates) against true anomaly angle. The green line is the value of the solar radiation pressure(right ordinates).

ber of such events during their observations. These are explosive events in which massive amounts of plasma ($10^{14} \div 10^{17}\, g$) are ejected from the Sun. They are characterized by a steep increase in plasma density, temperature and velocity. They also drag magnetic field structures known as "magnetic clouds" characterized by twisted field lines. These CMEs could open the magneotosphere of Mercury, such that solar particles would have direct access to the surface.

Another way to study temporal variability is to use solar telescopes. It is thus possible to track the evolution of sodium exosphere for more than a scarse half an hour permitted by stellar telescopes (and solar telescopes can never observe Mercury due to its proximity to the Sun). Using solar telescope THEMIS, Leblanc et al. (2008) were able for the first time to map intensity for several hours consecutively. They found localized high-latitude peaks, whose temperature was hotter than the rest of the exosphere. For the first time, these peaks were observed to vary within few (Earth) hours, strongly suggesting that they are prouced by solar wind sputtering. Some months later, using the same instrument, Leblanc et al. (2009) have observed a peak in the northern hemisphere that vanished during the first 5 hours of observation, and a peak in the southern hemisphere that lasted during the whole sequence (see fig. 3.9). These observations suggest that a strong ejection event occurred before or at beginning of observations, producing the short

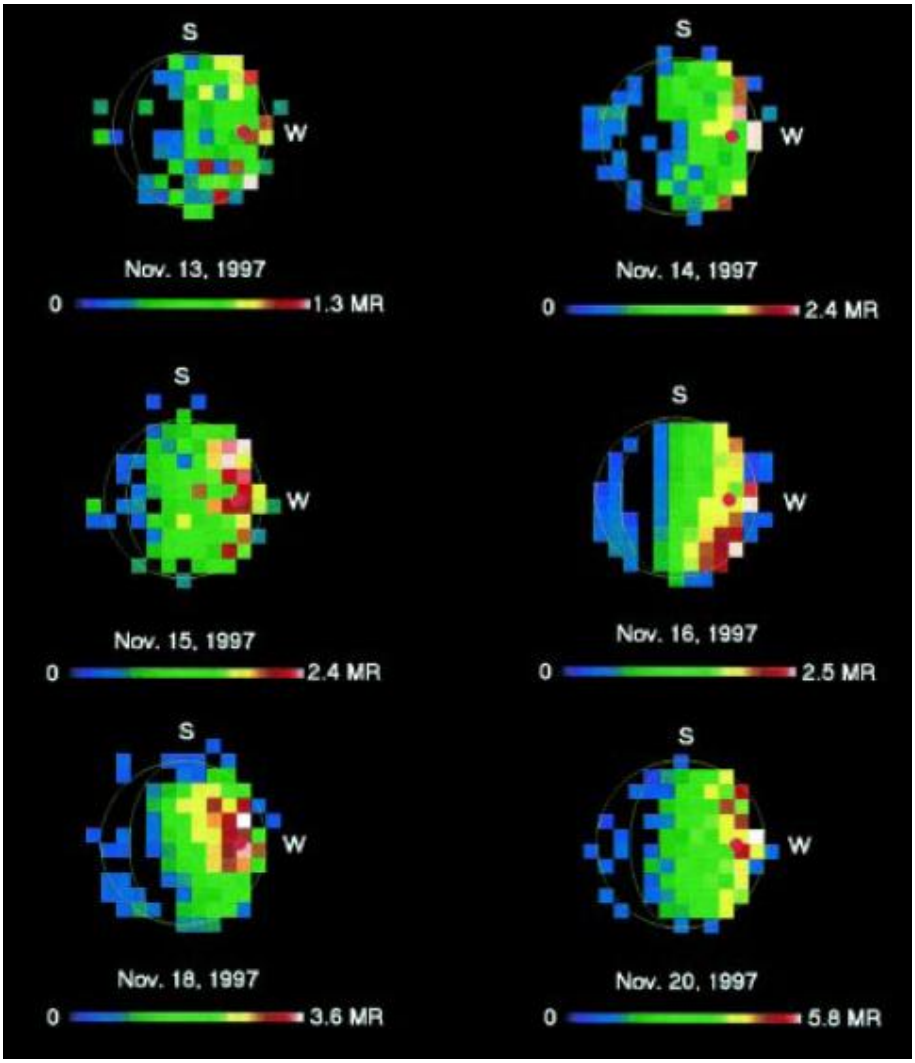

Figure 3.8: Daily changes in sodium emission at Mercury.

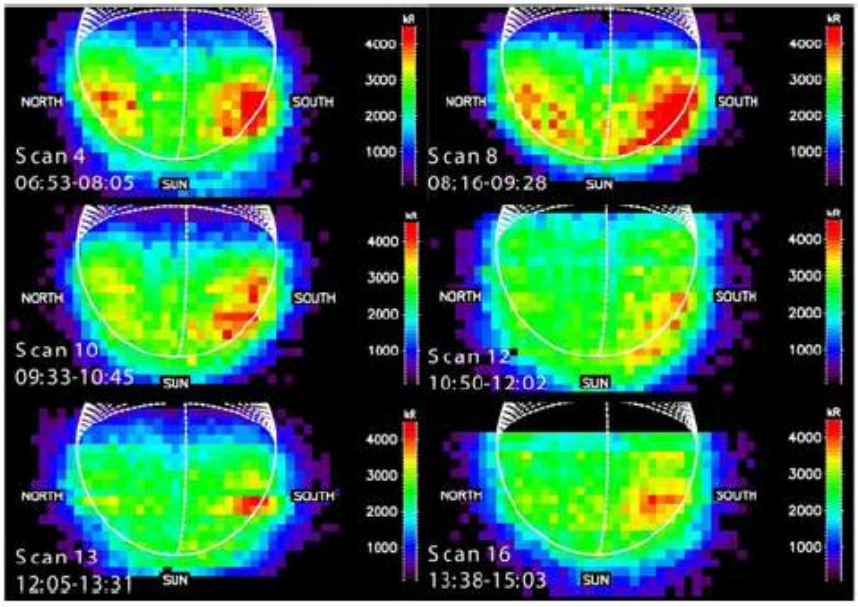

Figure 3.9: Emission brightness from THEMIS solar telescope.

northern peak.

Atoms are released through different emission processes, and are lost from the exosphere from different sinks processes - see fig. 3.10, taken from Killen & Ip (1999). I will review briefly the source and sinks of sodium atoms in the forthcoming sections.

3.2 Source processes

Atoms that are liberated from the surface by various source mechanisms are called "source atoms" and may be thermal or non thermal in nature. They impact the surface and move independently from point to point on the surface by ballistic hops. The number and shape of these hops are determined by the relevant forces acting on the atoms (namely, solar radiation pressure and Mercury's gravity), the nature of gas-surface interaction and the various loss processes that are operative. Source atoms that encounter the surface and have one or more additional ballistic hops are called "ambient atoms" and form the bound component of atmosphere. In fig. 3.11 from Smyth & Marconi (1995) are depicted the various processes that can emit atoms as well as the different fates they will experience.

In addition to the solar wind, plasma related to Coronal Mass Ejections (CMEs), cosmic rays and solar energetic particles, Mercury's surface environment is contin-

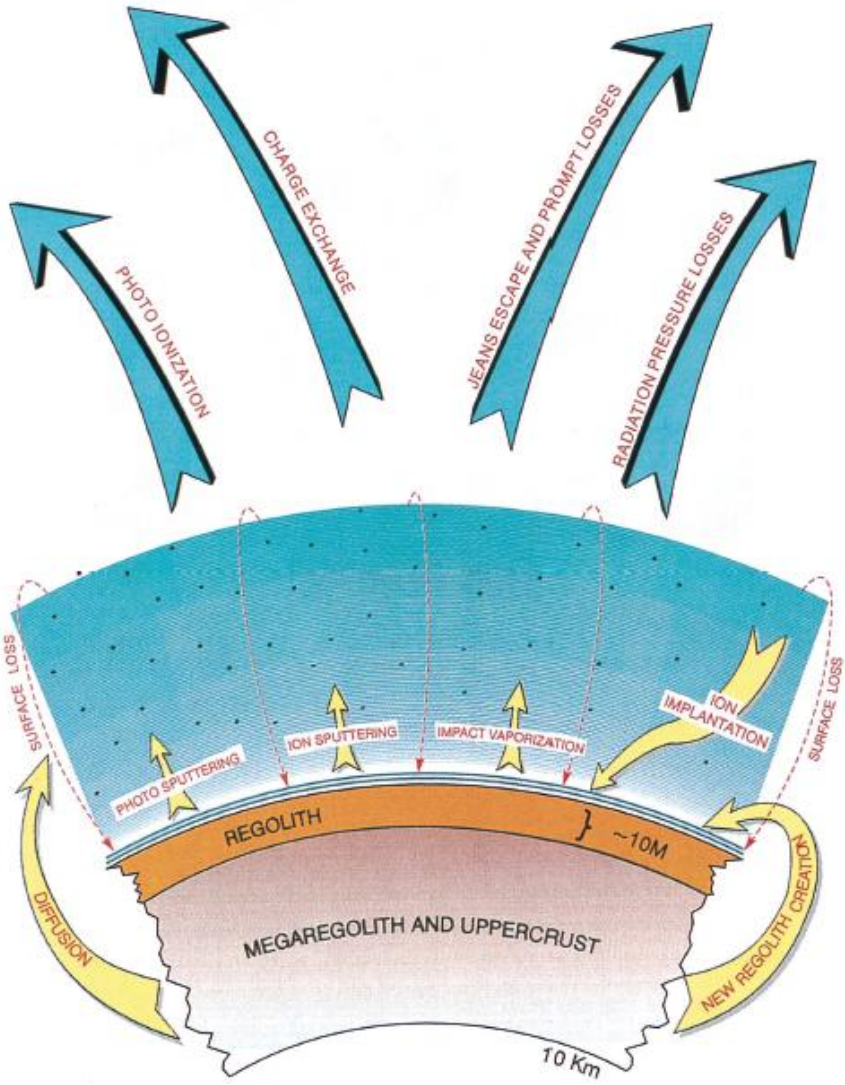

Figure 3.10: Sources and sinks of sodium atoms in Mercury's exosphere.

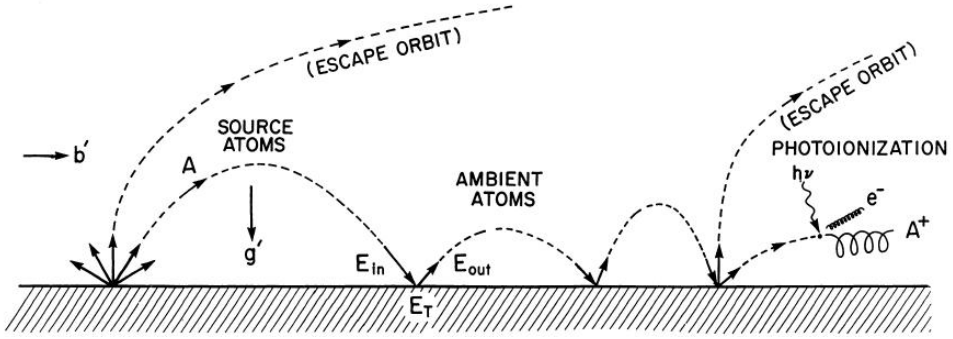

Figure 3.11: Surface-exosphere interaction at Mercury.

uously bombarded by solar radiation and electrons. Solar radiation in the form of infrared and visible and energetic photons is absorbed by the surface and causes heating and alteration of the dayside surface area. This heating can reach dayside temperatures on Mercury of up to about 700 K at the planet's equator, which is relevant for **thermal desorption**. Moreover, solar photons with energies ≥ 4 eV can induce bond-breaking, which is important for **photon-stimulated desorption** (PSD) of absorbed elements. Lower energy electrons in the order of tens of eV are also important in addition to surface charging because they can cause electronic excitations that also lead to **electron stimulated desorption** (ESD) of adsorbed elements from the planetary surface. **Micro-meteoroid impact vaporization** (MIV) is also a source of atoms, both from the impactor and from the surface. In the following subsections I describe these processes and their expected role in refilling Mercury's exosphere in more detail. Anyway, recently Leblanc & Johnson (2010) have demonstrated that no mechanism is dominant over the others during a year. Rather, particular features of the annual cycle of the sodium intensity appear to be induced by one, *temporarily dominant*, ejection mechanism. Mercury's exosphere content varies from $(1.6 \pm 0.1) \times 10^{28}$ Na atoms at TAA = 140°and 70°respectively to $(4.5 \pm 0.3) \times 10^{28}$ Na atoms at TAA = 180°and 0°.

3.2.1 Thermal Desorption

Thermal desorption (TD) is due to atoms whose thermal energy exceeds the binding energy. The TD depends strongly from exposure to Sun, hence the higher TD rate is at subsolar point at perihelion, when temperature as high as 700 K can be reached. Yakshinskiy & Madey (1999) studied Na desorption from a SiO_2 film, and they found that this process is strongly dependent upon surface composition and structure, and that sodium achieves appreaciable desorption rates at temperature greater than 350 K. Thermal desorption produces atoms at $0.03 \div 0.05\, eV$

energy (Yakshinskiy & Madey 2000), when escape energy at Mercury's surface is $2.07\,eV$. Thus, desorbed atoms remain close to the surface and do not contribute significantly to planetary loss. However, TD could deplete the sodium surface causing a lack of atoms available for more energetic processes (Hunten & Sprague 2002). The rate of ejection of Na atoms can be expressed with this formula:

$$\tau_{thd} = \nu c_{Na} \exp(U/k_B T_S) \tag{3.1}$$

where ν is the vibrational frequency in the surface, U the binding energy, k_B the Boltzmann's constant, c_{Na} the sodium concentration in the surface and T_S the surface temperature. The value most often used for ν is $10^{13}\,s^{-1}$ (Hunten et al. 1988), but in fact it can vary from 10^4 to $10^{23}\,s^{-1}$ (Killen et al. 2007), due to large number of physical processes involved in thermal desorption: diffusion to and from bulk rock or grains, surface diffusion between sites with different desorption energies, electronic excitation and de-excitation, jumps during near-desorption in excited states. The energy distribution for TD ejecta is a Maxwellian (Leblanc & Johnson 2003):

$$f(E,\theta) = 2\cos\theta \cdot \frac{E}{(k_B T_S)^2} \exp\left(-\frac{E}{k_B T_S}\right) \tag{3.2}$$

where E is the energy of the ejecta and θ is the angle between the velocity vector of ejecta and the normal to the surface - see fig. 3.12. The rate of thermal desorption

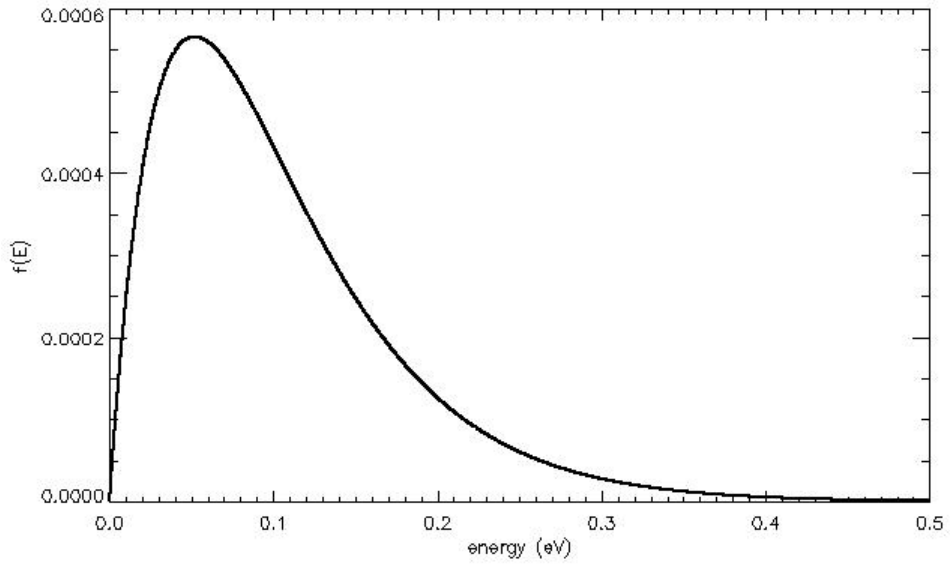

Figure 3.12: Normalized energy distribution for thermal desorption.

is in fact limited by the slowest process acting in the chain of events leading to desorption. For Mercury, Killen et al. (2004a) demonstrated that rate-limiting process for thermal desorption from Mercury's surface is **diffusion** of atoms from the bulk of the grains. In fact, the source rates for all processes other than impact vaporization (which accesses a depth equal to several impactor diameters) depends on the availability of atoms at the extreme surface. To maintain a long-term supply to the exosphere by PSD or ion-sputtering, atoms must diffuse from the bulk of the rock or grain to the extreme surface. The long-term source rates are therefore limited by the diffusion rates. These are dependent not only on temperature, but grain size and lifetime of the grain on the surface. The measured temperature for the sodium atmosphere is high, about 1200 K, whereas a high adsorption energy would imply efficient sticking at the surface, and hence rapid thermal accommodation to the surface temperature. However, observations of the variation of sodium D2 intensities with true anomaly angle imply that the sticking coefficient is quite small, on the order of 0.15 Potter et al. (2006).

3.2.2 Photon-Stimulated Desorption

Photon-stimulated desorption (PSD) corresponds to the desorption of surface elements as a result of electronic excitation by a photon of a surface atom. This varies with respect to the flux of photon at Mercury's orbit and therefore with respect to the square of Mercury heliocentric distance. At Mercury's surface it is also proportional to the cosine of the zenith angle on the dayside whereas this flux is null on the nightside. Yakshinskiy & Madey (1999) found from their laboratory experiments with Na covered lunar basalt samples that UV photons with energies of about 3-5 eV or greater than 5 eV cause desorption of "hot" Na atoms. This process acts through electronic transitions such as band gap excitation, valence electron excitation, or core excitation, rather than by thermal processes or momentum transfer. Yakshinskiy & Madey (2004) found that the desorbed Na atoms are suprathermal with a velocity peak in the PSD distribution of about $900\,m\,s^{-1}$. It was also discovered that desorption of Na varies with surface temperature and increased by a factor of 10 after the sample was heated from 100 K to 470 K.

The solar averaged cross section for photon stimulated desorption in the wavelength range $400 \div 250\,nm$ has been measured in laboratory by Yakshinskiy & Madey (1999), bombarding lunar silicates by UV photons ($\lambda < 300\,nm$). They found a cross section of $Q_{Na} = 3 \times 10^{-20}\,cm^2$. This has been obtained for a flat surface and needs to be reduced to take into account the porosity of the regolith (because of the probability that a desorbed atom in a regolith will collide with a surface element before reaching the extreme surface), so probably the cross section is closer to the value predicted by Killen et al. (2001), that is $Q_{Na} = 1.4 \times 10^{-21} cm^2$. Only volatile species, mostly Na and K, will be released into the exosphere via PSD,

and this is a highly nonstoichiometric process in reproducing the composition of the surface in the exosphere (Wurz & Lammer 2003).

To investigate the PSD-induced release of atoms from the surface of Mercury, the variation of solar UV photons incident on the planetary surface over the planet's orbit has to be considered. The solar flux at Mercury's eccentric orbit differs substantially from the average condition present at 1 AU. The solar UV flux is about a factor 11 higher at the periherm and more than five times higher at apoherm than that at the Earth's orbit in 1 AU. The largest PSD fluxes of released Na occur near equatorial latitudes at periherm, and there should not be any noticeable PSD sources at Mercury's polar areas (Lammer et al. 2003). In addition to PSD experiments with adsorbed Na and K atoms on lunar silicates, Yakshinskiy & Madey (1999) also studied electron-stimulated desorption (ESD). They found that exposure of Na covered surfaces by low energetic electrons with energies from $3 \div 50\, eV$ causes also desorption of "hot" Na atoms. Generally there are intimate connections between ESD and PSD because similar electronic processes cause desorption of the atoms via electron or photon excitation. However, the release of Na via ESD is strongly temperature dependent. The observed average ESD cross-section for Na atoms and $10 \div 50 eV$ electrons is about $(1 \div 2) \times 10^{-19} cm^2$ Yakshinskiy & Madey (1999). The experimentally determined ESD cross-section for atomic Na has its initial threshold at about $4\, eV$, which is comparable with the PSD threshold. Furthermore, the desorption cross-sections have a similar magnitude for electron energies of about 5 eV. If one assumes quasi-neutral solar wind plasma, then electron fluxes for electrons with energies of about 12 eV are about 5×10^9 and $2 \times 10^9\, cm^{-2}\, s^{-1}$ at periherm and apoherm, respectively.

Particle ejected through this mechanism have the Weibull energy distribution (see fig. 3.13):

$$f_{PSD}(E) = \beta(1+\beta)\frac{EU^{\beta}}{(E+U)^{2+\beta}} \tag{3.3}$$

where E is the particle energy, U the characteristic energy for PSD for a particular species, and β the shape parameter of the distribution: $\beta_{Na} = 0.7$; $\beta_K = 0.25$; $U_{Na} = 0.098\, eV$ (Johnson et al. 2002). The flux of desorbed atoms is:

$$\phi_{Na}^{PSD} \approx \frac{1}{4}\phi_{ph} Q_{Na} f_{Na} N_S \tag{3.4}$$

where the factor 1/4 gives the surface-averaged value, N_S is the total regolith surface density ($N_S = 7.5 \times 10^{14}\, cm^{-2}$) with a sodium fraction in the regolith $f_{Na} = 0.0053$ (Killen et al. 2001). $\phi_{ph} = 2.29 \times 10^{16}\, cm^{-2}\, s^{-1}$ is the solar UV photon flux at 0.38 AU integrated over the wavelength range from 0.1 to $318.0\, nm$ (Wurz & Lammer 2003). Q_{Na} is the PSD cross section. Using these values, equation 3.4 gives $\phi_{Na}^{PSD} \approx 4.1 \times 10^{12}\, m\, s^{-1}$. With an average release velocity of

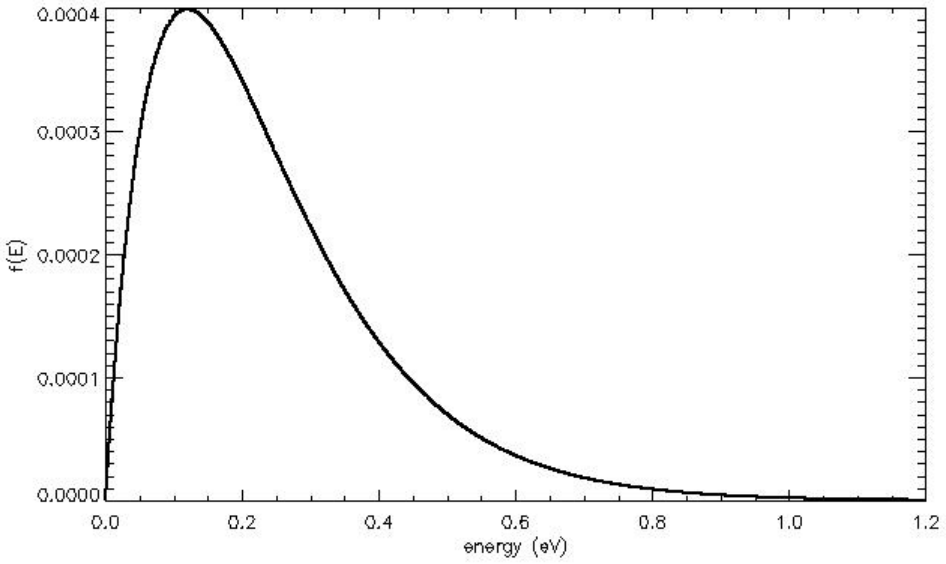

Figure 3.13: Normalized energy distribution for photon stimulated desorption.

$v = 1000\,m\,s^{-1}$ (Yakshinskiy & Madey 2001) the exospheric density at the surface is $n_0 = 4.1 \times 10^9\ m^{-3}$.

3.2.3 Solar Wind Sputtering

Physical sputtering, or simply sputtering, is the release of particles via momentum transfer. Particle sputtering will release all species from Mercury's surface into space, reproducing more or less the local surface composition on an atomic level. Although the small magnetosphere is capable to stand off solar wind most of the time, it has been argued that for certain, restricted, time intervals Mercury's magnetosphere could be open to the solar wind over significant areas when the interplanetary magnetic field turns southwards or when the solar wind dynamic pressure is very high (Massetti et al. 2003). The solar wind ions can thus impinge on the planet's surface by direct penetration through the cusp regions and lead to variability of Mercury's exosphere. Magnetospheric ions hitting the planet's surface at the auroral zones will also cause sputtering. However, even under favorable conditions only a few percent of Mercury's surface are associated with open magnetic field lines.

The energy distribution for sputtered particles is described by a Sigmund-

Thompson function (Sigmund 1969):

$$f(E_e) = \frac{6E_b}{3 - 8\sqrt{E_b/E_c}} \frac{E_e}{(E_e + E_b)^3} \left(1 - \sqrt{\frac{E_e + E_b}{E_c}}\right) \tag{3.5}$$

where E_b is the surface-binding energy of the sputtered particle, E_e the energy of the sputtered particle, E_c the cut-off energy, or the maximum energy that can be imparted to an atom by a projectile with energy E_i:

$$E_c = E_i \frac{4m_1 m_2}{(m_1 + m_2)^2} \tag{3.6}$$

The maximum of the energy distribution is at $E_{max} = E_b/2$. See fig. 3.14 for energy distribution.

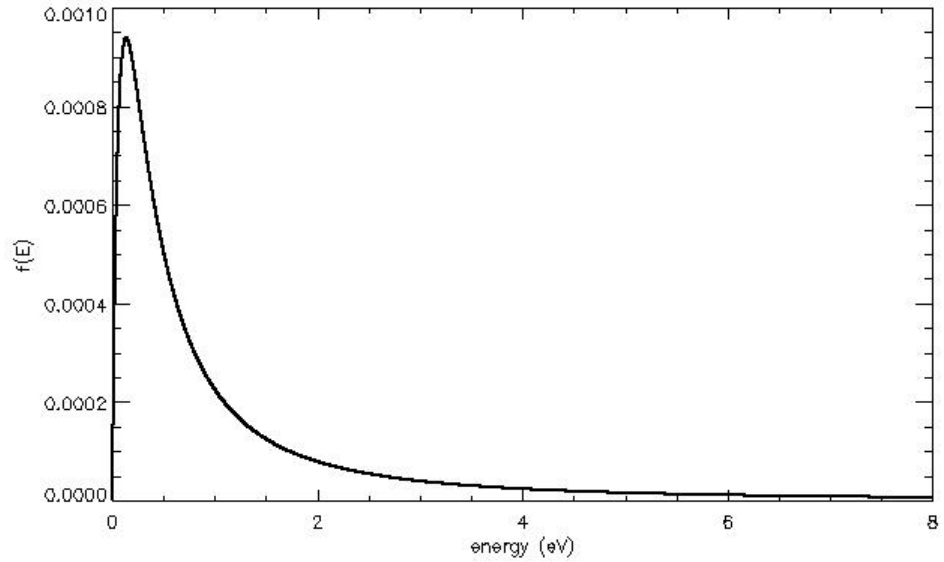

Figure 3.14: Normalized energy distribution for sputtering.

The total flux of precipitating solar wind particles onto Mercury's surface is:

$$\Phi_{sw} = C\rho_{sw} v_{sw} A_s \tag{3.7}$$

where ρ_{sw} is the solar wind density, v_{sw} the solar wind velocity, A_s the surface area associated with open magnetic field lines. C is a factor that takes into account the assumed difference of the surface area with open field lines and the corresponding

area in the undisturbed solar wind. Local solar wind flux is $\phi_{sw} = \Phi_{sw}/A_s$. Therefore, if the flux of ions impinging the planetary surface, ϕ_{ion}, is known one can calculate ab initio, with the sputter yield Y_{Na}, the sputtered flux, the surface density, the density profile, and the column content and compare these numbers with the observations. Using a weighted sputter yield of the solar wind of $Y_{tot} = 0.15$ per solar wind ion, the sputtered flux is $\phi_{sput} \approx 4.2 \times 10^{12}\, m^{-2}\, s^{-1}$ with $C = 1$ (Wurz & Lammer 2003). With a typical energy of the sputtered Na particles of $0.6\, eV$, corresponding to the temperature of $T = 6500$ K of the suprathermal Na atoms, one has an exospheric surface density of Na of $n_0 = 1.9 \cdot 10^9\, m^{-3}$.

3.2.4 Micrometeoroid Impact Vaporization

Micrometeorite impacts may contribute to the production of exospheric densities, including low-volatile and refractory species. Especially during quiet times, i.e., without energetic ions from the magnetosphere or the solar wind hitting the surface, it may be the only release process acting over the whole planetary surface. The composition of the Hermean exosphere reflects the chemical composition of the surface, and of meteorites impacting Mercury, mixed with traces of solar wind. Unfortunately, the meteoritic gardening and the impact history of the Mercury surface is presently unknown because it depends on variables related to the composition of the surface and the flux of meteoroids: this latter is roughly derived from estimate at the Earth's heliocentric distance, then extrapolated to the inner Solar System. It means we may not have a good estimate of the statistics on the number of impacts and the velocity distribution of the meteoroids.

The impact of micrometeorites will evaporate a certain volume from Mercury's surface to the exospheric gas at the impact site. About one to two orders of magnitude more material than its own is released because of the high impact speed for meteorites at Mercury (Cintala 1992). The meteorites will consist of mainly refractory material since the meteorite population in the inner solar system is not as rich in H_2O and other volatiles as in the outer solar system, which is more cometary-like being supplied from cometary matter having their origin in the Kuiper Belt (Divine 1993). The ratio of the maximum ejecta velocity to the primary impact velocity decreases with increasing impact speed. The measured temperature in the micrometeorite produced vapor cloud is in the range of $2500 \div 5000$ K (Eichhorn 1978). Such temperatures are up to a factor ten higher than Mercury's dayside surface temperature, but the corresponding characteristic energies are still lower than for particles that result from surface sputtering. Cintala (1992) estimated the total vaporization for Mercury to range from 8.18×10^{-16} to $2.75 \times 10^{-15}\, g\, cm^{-2}\, s^{-1}$ for aphelion and perihelion, respectively. Later, using a higher mass influx and considering surface porosity, Killen et al. (2001) estimated the total impact vaporization rates on diabase regolith and found vaporization rates between 9.0×10^{-16}

and $1.6 \times 10^{-14} g\, cm^{-2}\, s^{-1}$. From the total vaporization rates, Na vaporization rates can be estimated that correspond to fluxes of released Na atoms, which range from 1.3×10^9 to $2.2 \times 10^{10}\, m^{-2}\, s^{-1}$. With the most probable speed of Na at 4000 K we get exospheric surface gas densities of Na ranging from $n_0 = 7.2 \times 10^5\, m^{-3}$ to $n_0 = 1.3 \times 10^7\, m^{-3}$. These densities have to be compared with the exospheric surface density for quiet times of $2.1 \times 10^{10}\, m^{-3}$ derived from observations. Aside from the uncertainties of the estimate, the contribution to the exosphere by impact-vaporization appears to be one or two orders of magnitude smaller than by other processes, when these processes operate. Impact vaporization may only be relevant at the night-side of the planet.

3.2.5 Chemical sputtering

Chemical sputtering is a term that refers to ejection of Na atoms from reactions that occur at the surface, for example (Potter 1995):

$$2H + Na_2SiO_3 \rightarrow 2Na + SiO_2 + H_2O \tag{3.8}$$

Chemical reactions, either on the surface or in the atmosphere, can enhance the loss rates of the reaction products if the reaction products are created with enough energy to escape. Very little work has been done to quantify rates for chemistry as a source or loss process in the context of planetary sciences.

3.3 Loss Processes

There are also several mechanism for loss of sodium from the exosphere, that can be defined into two categories of loss: reversible loss processes (sticking to the surface or ionization followed by impact with the surface and neutralization) and irreversible loss processes (Jeans escape and ionization followed by crossing the magnetopause boundary and entrainment into the solar wind). Reversible loss processes must be further characterized as long-term loss, such as burial or chemical reaction into a bound state with a large binding energy, or short-term loss such as adsorption on the surface of grains. Sticking to the surface results in loss from the exosphere but not from the regolith.

Jeans escape (see section 1.5.1) is an irreversible loss process, that affects only H and He, at the ambient surface temperature on Mercury (Hunten et al. 1988). However, with the exception of thermal vaporization, the source processes populating the Hermean exosphere create non-thermal populations and the mean energy is species dependent. The mean velocities of atoms ejected by ion-sputtering may be above escape velocity, $4.25\, km\, s^{-1}$, and will depend on the binding energy of the atom in the substrate, and its mass. The binding energy of a given atom will

depend not only on the particular mineral in which it is found, but also on the surrounding conditions (Holmlid 2006).

3.3.1 Photoionization

Photoionization is an irreversible loss process *if* the ions cross the magnetopause and become entrained in the solar wind. Killen et al. (2004b) suggested that half of the photoions produced near the surface return to the surface where they are neutralized. An east-west electric field produces an asymmetric escape pattern such that those ions created on the dusk side reimpact on the dawnside, and those ions created on the dawnside escape across the magnetopause boundary or impact the nightside. However, the escape rate is higher as the ions are produced at successively higher altitudes. Photoionization rates of many likely exospheric species are known. However, the sodium ionization rate is controversial because of the discrepancy between the experimental and theoretical cross-sections.

3.3.2 Charge-Exchange

A charge-exchange process may occur when an energetic ion collides with an exospheric neutral particle (target). In the interaction, an electron and a small amount of kinetic energy are exchanged between the neutral and the ion; the net result is an energetic neutral atom and a thermal ion. The target (ionized) is scattered at an approximately perpendicular angle with respect to the projectile path; the newly created fast neutral retains approximately both the energy and the direction of the colliding energetic ion. The energy defect of the process is equal to the difference of the two atomic ionization potentials . The cross-section varies with species and energy and is of the order of $10^{-14} \div 10^{-17} cm^2$ Killen et al. (2007). Charge exchange at Mercury may occur due to solar-wind plasma as well as due to planetary ions. Generated neutrals have typical energies of 1 keV or more. Hence, such neutrals are no more trapped in ballistic orbits and the result is a net loss from the planet. This process mostly occurs in the dayside and dawnside regions close to the planetary surface. Mura et al. (2005) have estimated that, approximately, less than 1% of the solar wind plasma circulating inside the magnetosphere of Mercury experience charge-exchange. The related charge-exchange loss rate, cumulated on all neutral species, is between 10^{22} and $10^{24}\, atoms\, s^{-1}$, which is, on average, small if compared to other loss mechanisms.

3.4 The Mercury Sodium Tail

Sodium tails have been observed streaming away from a number of solar system objects: comets (Cremonese et al. 1997), the Moon (Mierkiewicz et al. 2006) and Mercury (Potter et al. 2002). The presence of an anti-sunward tail at Mercury was first predicted by Smyth (1986). Each time a sodium atom scatters a solar photon, it recoils in the anti-sunward direction. As these atoms accelerate away from the Sun, they move out of the Fraunhofer absorption line, experience increasing solar flux, and consequently an ever increasing acceleration. After ~ 50 hours the atoms are moving at $\sim 10\,km\,s^{-1}$. For example, the discovery image of the lunar Na tail showed it to decrease from a few hundred Rayleighs near the limb to ~ 5 Rayleighs at a distance of $16\,R_{☾}$ (Mendillo et al. (1991) and section 4.3).

Since modeling studies indicate that Mercury's total neutral sodium production is perhaps ~ 100 times the rate of the Moon Morgan & Killen (1997), coupled to the fact that the solar flux at Mercury's average distance (and therefore the radiation pressure) is ~ 7 times that at Moon's distance, while the surface gravity is only twice that of the Moon, it is expected that Mercury should have a sodium tail similar to that of the Moon, only brighter and longer. Indeed, the first detection of Mercury's sodium tail (Potter et al. 2002) showed brightness levels decreasing from 6 Mega-Rayleighs (MR) at the disk to 600 R in a tail detected out to 16 Mercury radii ($\sim 40000\,km$) during the "out" leg of the orbit (Mercury moving away from the Sun). At this distance, velocities up to $11\,km\,s^{-1}$ were observed downstream, and the tail was expanding, on average, at a rate of $(1.9\pm0.3)\,km\,s^{-1}$. The source rates for sodium generation from Mercury into the tail were found to be in the range $(2 \div 5) \cdot 10^{23}\,atoms\,s^{-1}$, corresponding to between 1 and 10% of the estimated total sodium production rate on the planet. The limiting value of radiation acceleration required to produce an observable sodium tail was estimated to be $(112 \pm 24)\,cm\,s^{-2}$. For observations where Mercury was moving towards the Sun ("in" leg of the orbit), the emission intensity in the sodium tail decreased very rapidly with distance downstream, disappearing entirely beyond $12000\,km$ ($6R_{☿}$) for radiation accelerations of 128.7 and $135.4\,cm\,s^{-2}$. For smaller radiation accelerations, the sodium tail was not detectable at all, yielding a limiting value for tail generation of about $(122 \pm 2)\,cm\,s^{-2}$. Baumgardner et al. (2008) imaged the sodium tail up to 3.4 millions km (fig. 3.15), a distance achieved in less than 2 ionization time constants, or ~ 14 hours. Thus, the extraordinary length of the sodium tail portrays Na source conditions versus time. All of the sodium seen in the extended tail was on the surface of Mercury less than a day earlier.

Ip (1986), Smyth (1986) and Smyth & Marconi (1995) modeled the effects of radiation acceleration on trajectories of sodium atoms emitted from the surface at various velocities and showed that the spatial character and density of sodium atmosphere and tail changes with the position of Mercury in orbit, as consequence

of the change of radiation acceleration. For minimum value of solar radiation pressure the shape of the sodium exosphere is essentially the same as it would be for solar radiation acceleration of zero, producing a "normal" spherically symmetric atmosphere. However, for the maximum value of solar radiation acceleration, the atmosphere is severely depressed at the subsolar point, and for atoms leaving the surface at velocities greater than $2\,km\,s^{-1}$ the atoms can escape the planet to form a long comet-like neutral sodium tail. Given this, the morphology of the sodium tail behind the planet could be used to infer the ejection conditions, and thus to understand the source processes for sodium on Mercury.

In addition to the effect of solar radiation pressure, there is evidence that space weather in the vicinity of Mercury can also produce substantial changes in the sodium atmosphere as a result of changes in sodium production processes Killen et al. (2001). These changes would also be reflected in the morphology of the sodium tail.

3.4.1 The role of the Solar Radiation Pressure

Solar radiation acceleration on sodium atoms varies with the position of the planet in the orbit, depending on distance from the Sun and on heliocentric radial velocity of Mercury. The heliocentric radial velocity of Mercury varies between $\pm 10.06\,km\,s^{-1}$, and as a result, the solar spectrum seen by a sodium atom on the planet shifts between ± 200 mÅfrom the center of the sodium Fraunhofer line in the solar spectrum. Since this line is very deep, the shift leads to more than an order of magnitude change of solar intensity seen by a sodium atom, with corresponding changes in the solar radiation acceleration experienced by the atoms. As a result, the radiation acceleration can reach large values, up to $200\,cm\,s^{-2}$ (54% of surface gravity) at true anomaly angles near 64°and 300°, and minimum value of $12\,cm\,s^{-2}$ at aphelion, true anomaly angle of 180°.

The tail configuration is expected to differ between "out" leg of the orbit (true anomaly angle, TAA $<$ 180°) and "in" leg of the orbit (TAA $>$ 180°). When Mercury is on the "out" leg of its orbit, the sodium atoms in the Mercury exosphere see sunlight shifted redwards, and will scatter sunlight from the low-wavelength, or "blue" side of the Fraunhofer line. When the atom velocity increases as a result of radiation acceleration, the solar spectrum seen by the atom will shift further redwards, resulting in an increase of the intensity of sunlight seen by the sodium atom on the blue side of the Fraunhofer profile. This is a self-accelerating process- the faster the sodium moves anti-sunward, the greater the intensity of sunlight it sees, the greater the radiation acceleration, and the greater the intensity of scattered sunlight. When Mercury is on the "in" leg of its orbit (TAA $>$ 180°), the situation is reversed. Here, sunlight seen at Mercury is shifted bluewards, and sodium scatters light from the high-wavelength side, or "red" side of the Fraunhofer

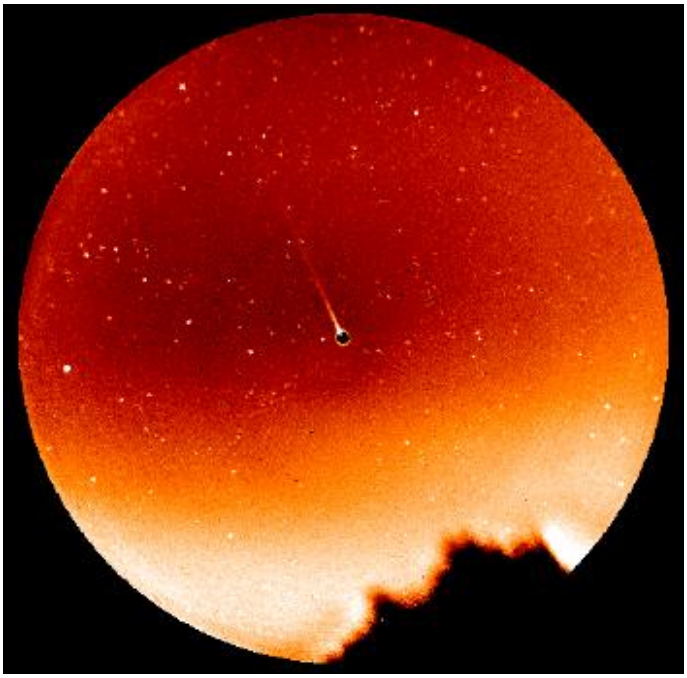

Figure 3.15: The anti-sunward sodium tail of Mercury.

line. Now, when radiation acceleration imparts an anti-sunward velocity to the sodium atom, the solar spectrum seen by the atom will shift redward, and the atom will see a lower intensity of sunlight. As a result, the intensity of sunlight scattered from the sodium atom decreases. Detailed model calculations of the sodium exosphere by Smyth & Marconi (1995) included these effects, showing how the predicted shape of the sodium exosphere might differ between the two legs of the orbit: see fig. 3.16. The same authors pointed out the importance of photoionization in the formation of the anti-sunward tail. Photoionization times range from about 4.6 to 10.6 h from perihelion to aphelion (Cremonese et al. 1997). Thus, a sodium atom can experience solar radiation acceleration over a period of several hours before photoionization removes it from the scene. During this time, solar radiation acceleration will change the anti-sunward velocity of the atoms, with corresponding changes in the intensity of scattered sunlight. The planet-wide interaction of solar radiation acceleration with sodium atoms is complex, with atoms generated near the subsolar point affected differently than atoms generated near the terminator. The overall effect of radiation acceleration might be described by a single number, representing the effective time that sodium atoms were exposed to sunlight, and calculated the effect for a range of exposure times. Fig. 3.17 from Potter et al. (2007) shows how the calculated relative emission intensities

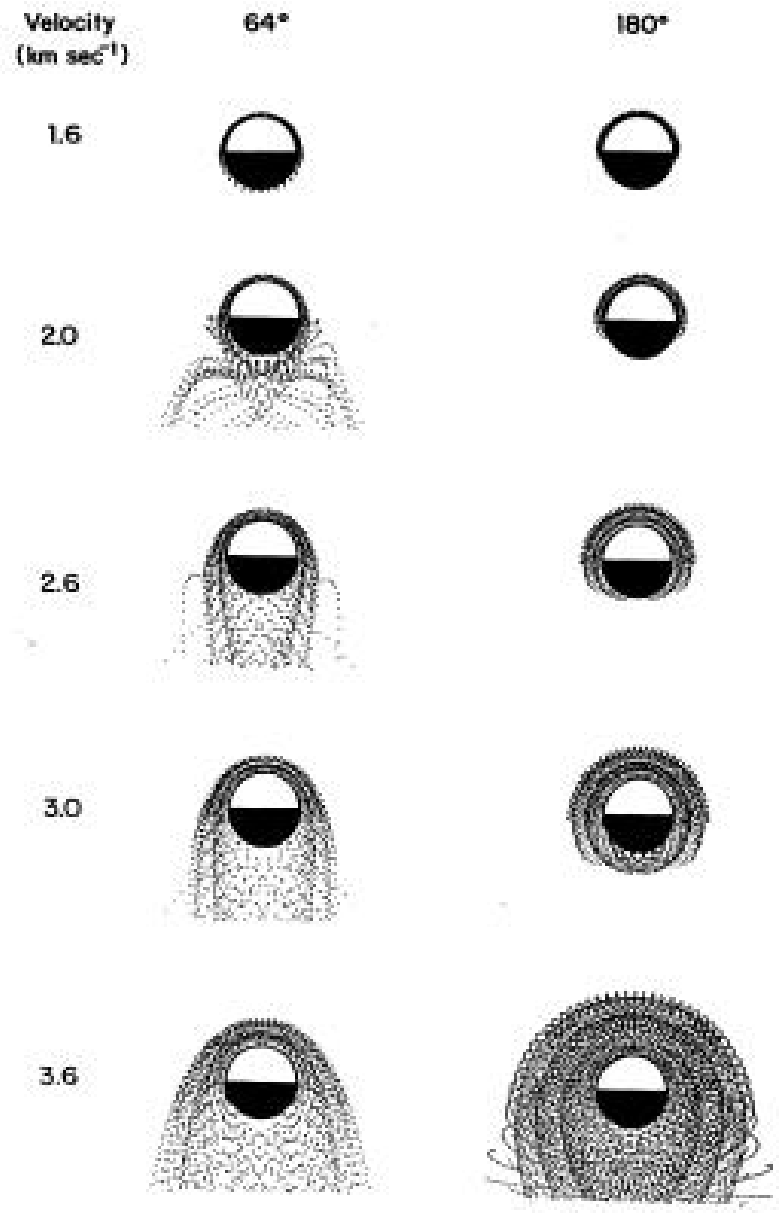

Figure 3.16: Comparison of the spatial character of sodium at maximum (TAA = 64°) and minimum (TAA = 180°) solar radiation pressure, for different ejection speeds.

for sodium atoms on Mercury would vary with radiation acceleration for both the sunward and anti-sunward directions of the orbit, assuming an exposure time 1700 s. The relative intensity plotted in fig. 3.17 is defined as the ratio of emission intensity after acceleration to the intensity before acceleration. The variation of relative intensity with radiation acceleration for the "out" leg of the orbit shows the expected increases in intensity resulting from increased anti-sunward velocity.

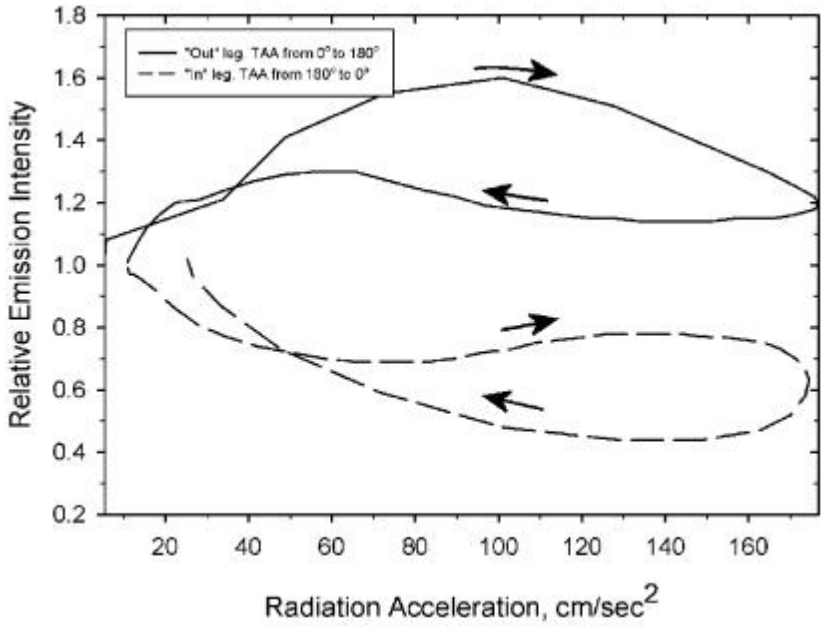

Figure 3.17: Effect of Solar Radiation Acceleration on Relative Brightness.

3.5 My work on Mercury

My work on Mercury has been double. First, I've helped in the reduction of telescopic observations of Mercury, whose results have been published in Mangano et al. (2009), and summarized in section 3.9. On the other hand, I've started a modelization of Mercury's anti-sunward sodium tail, with the aim to provide a tool to understand the obserations. Description is provided in section 3.8, and preliminary results in 3.9.

Table 3.1: Mercury parameters for observations at TNG in 2005

Parameter	June 29^{th}	June 30^{th}	July 1^{st}
Heliocentric distance (AU)	0.42	0.43	0.43
Heliocentric radial velocity ($km\,s^{-1}$)	8.12	7.77	7.39
Earth-Mercury velocity ($km\,s^{-1}$)	-28.72	-28.58	-28.42
True Anomaly Angle (degrees)	124	127	130
Phase angle (degrees)	81	83	85
Seeing FWHM (arcsec)	$2.5 \div 3.3$	$1.5 \div 2.2$	$2.5 \div 3.5$

3.6 Observations

Observations have been carried on at TNG telescope in 2005, with the same instrumental setup used for Io observations (see section 2.5): i.e. high resolution spectrograph SARG, sodium filter in order to isolate the order of interest, long slit. Observations lasted half an hour around sunset, repeated for three consecutive nights. See tab. 3.1 for the observational parameter. The phase angle is the Sun-Mercury-Earth angle.

3.7 Data Reduction

Preliminary data reduction steps of TNG-SARG data are the same of those performed during Io's work: bias, flat fielding, calibration in wavelength (see subsection 2.6.1). The subsequent data reduction steps are different.

3.7.1 Removal of diffuse sky light

The first additional step is the removal of the diffuse sky light, which is important because observations are carried during twilight. For this operation I've performed a twofold operation. First I've fit a 1D spectrum of sky (upper right spectrum of fig. 3.18), created averaging a few columns on the anti-sunward side of Mercury spectra (left spectrum in fig. 3.18). I then normalized to 1 this sky spectrum, and multiplied it by the fit of the spatial profile, obtained averaging few rows (in the spectral direction) of the spectra. See figures 3.19 and 3.20.

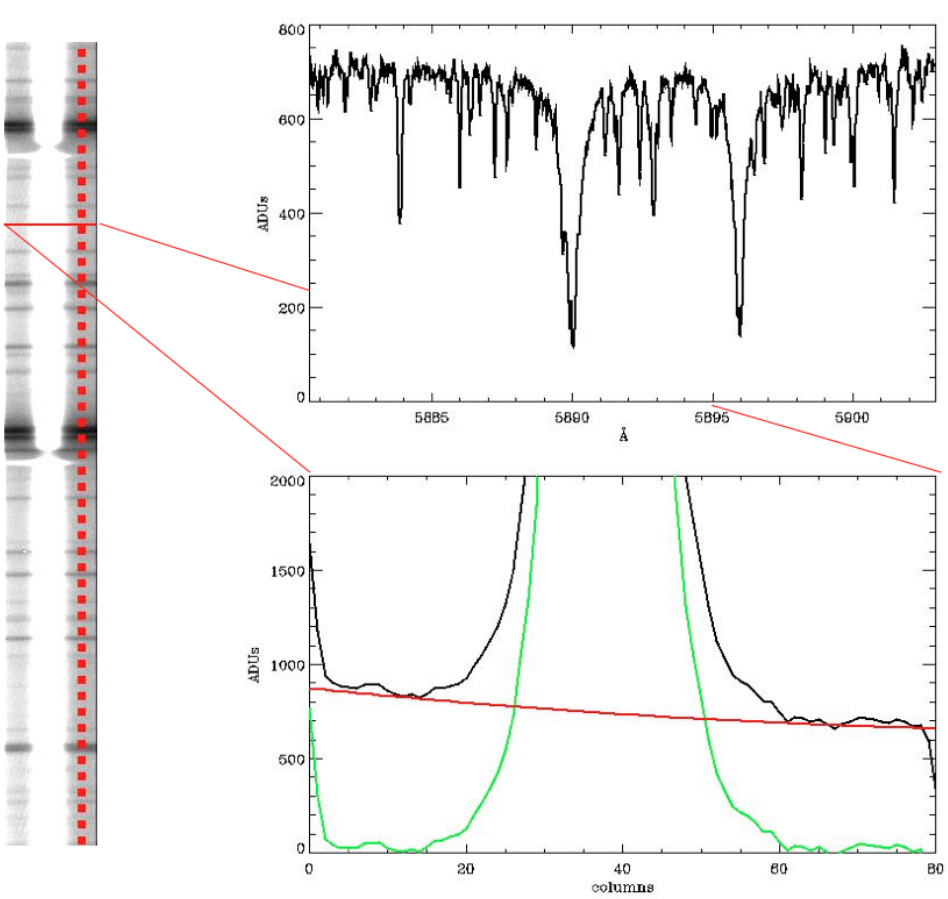

Figure 3.18: First, a template of the sky spectrum (upper right graph) is found by averaging the red dashed region in spectrum on the left. Then, this template, properly scaled to 1, is then scaled to the spatial profile (averaged along the spectral direction) of the Mercury spectrum. In the lower right graph is reported the spatial profile of Mercury (black), the spatial fit (red) and the subtraction between the twos (green), all at the wavelength indicated by the red solid line in the left panel. Wavelengths increase upwards, and the Sun is on the left.

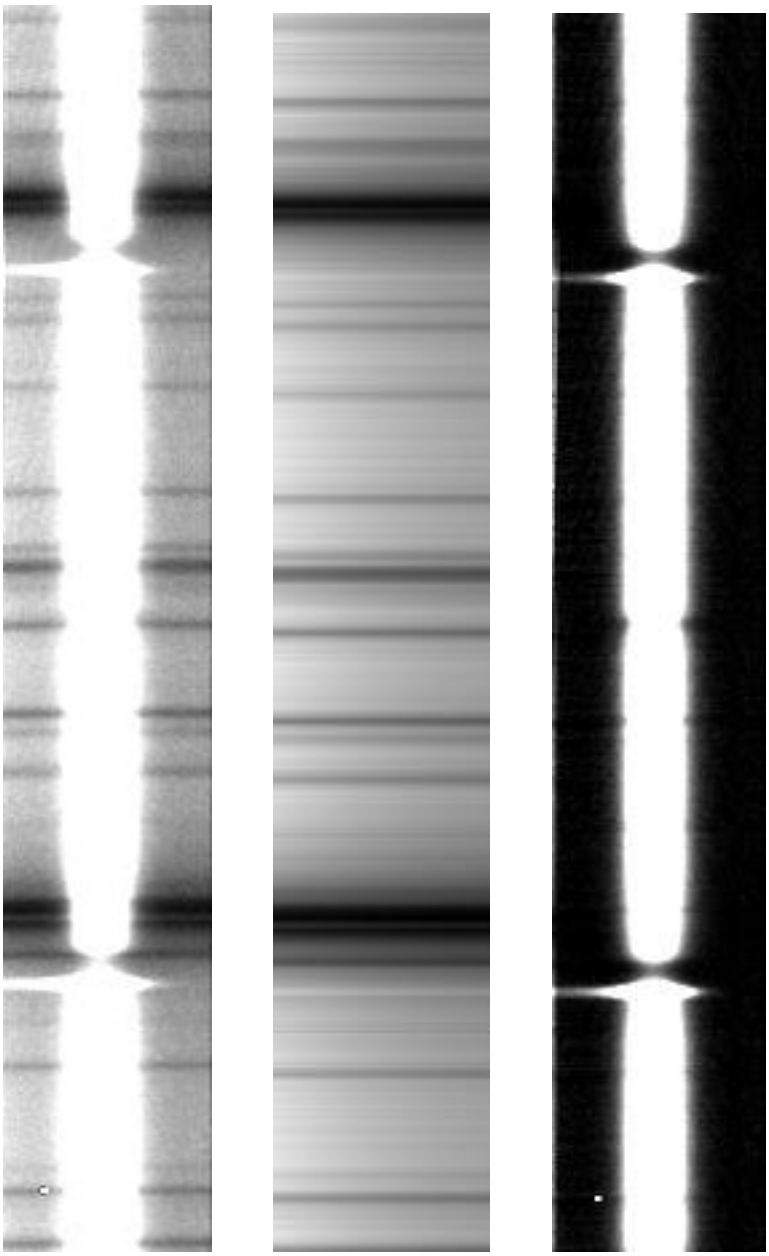

(a) (b) (c)

Figure 3.19: The removal of diffuse sky light. Left: the original, calibrated, Mercury sprctrum. Middle: the extrapolated sky. Right: the object sky-subtracted. Wavelengths increase upwards, and the Sun is on the lefts side, where the extrapolated sky is seen to be brighter.

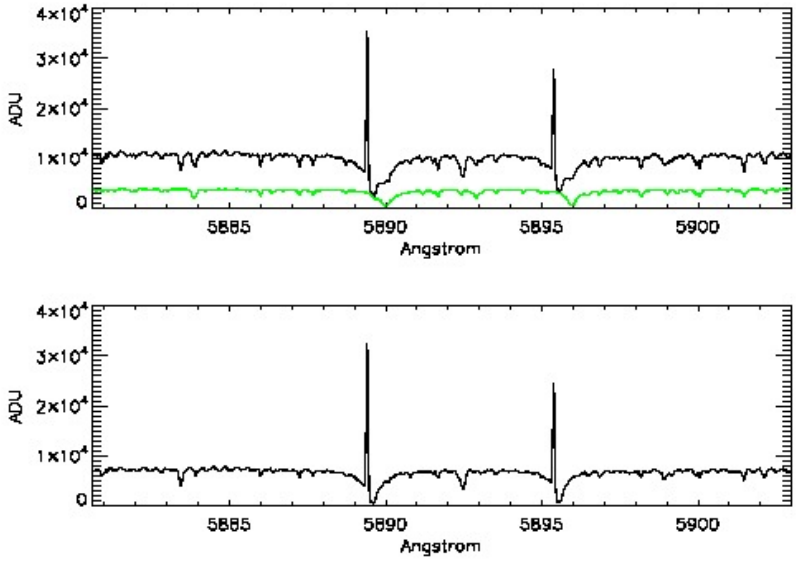

Figure 3.20: The removal of diffuse sky light. Top: spectral profile of Mercury's continuum (black) and diffuse sky light (green). Bottom: spectral profile of Mercury's continum after the subtraction of the diffuse sky light.

3.7.2 Calibration in Rayleighs

Unlike the case of Io, here I had to use Mercury itself for calibration, because the poor seeing, unavoidable observing at twilight with ordinary (nightly) telescopes, blurs the planet's disk. I had to use Hapke method (Hapke 1993). First, a model of Mercury's surface reflectance is reproduced, depending on the phase angle and on the apparent diameter of the planet. Then this reflectance image is convolved with various values of the seeing until the convolved image matches the observed one (in this step one has also a better estimate of the seeing during the observations). The Hapke method allows to convert ADUs into Rayleighs (equation 2.2) comparing the peak in intensity in ADUs in the slit and the peak in intensity in Rayleighs of the theoretical, blurred, model.

The program first generates a model of Mercury reflectance according to the observational parameters, that is the phase angle (or Sun-Mercury-Earth angle) and the apparent diameter of the planet. Then generates a blurred image of this reflectance model using various values of seeing, however close to the assumed one during the observations. The blurred image is compared to the slitview one, and seeing is changed until the variations between the slitview image and the blurred image is below a certain treshold. The seeing so calculated is the so-called seeing

sigma σ. It is related to the FWHM of the seeing by:

$$\sigma_{FWHM} = 2\sigma\sqrt{2\ln 2} \approx 2.35\sigma \tag{3.9}$$

Another important problem in observing Mercury is that, because of the poor seeing, the position of the slit on the disk if not accurately determined. At TNG, this error can reach 1 arcsec, when the planet typically has an apparent diameter of $6 \div 7$ arcseconds. In order to improve this situation, a scan on the theoretical, blurred image is performed by the routine. It predicts the expected counts for a slit placed in different (parallel) positions close to the one recorded during the observations. When the peak of the theoretical, blurred image match the peak of the slit, the position is recorded (see 3.21(a)). In this way it is possibile to improve the error on the position, to about half arcsecond.

Now it is possibile to use Mercury itself as a standard candle. In fact, knowing the position on the disk and the brightness in Rayleighs from the blurred, theoretical disk, the peak of counts in the slit (still in ADUs) is compared to the peak of counts in the blurred disk, which is in Rayleighs (see fig. 3.21(b)). The ratio between the twos (and divided by the exopsure time) gives the calfactor (see section 2.6.5) and this, in turn, allows the calibration in Rayleighs of both continuum and the exospheric emission (see fig. 3.21(c)). Calfactor is expressed in $kR\,s\,ADU^{-1}$.

Results are exposed in section 3.9.

3.8 The sodium tail model

I developed a Fortran routine in order to study the distribution of sodium atoms in the anti-sunward tail, and to compare this distribution with the spectra taken at ground-based telescopes (thus not only TNG).

The code generates a fixed number of particles each second throughout the planet surface, and follows their trajectory under the influence of Mercury gravity and Solar Radiation Pressure (SRP), using 4th order Runge-Kutta algorithm. Particles are ejected in the illuminated hemisphere of the planet by three different processes: thermal desorption (section 3.2.1), photon-stimulated desorption (section 3.2.2) and solar wind sputtering (section 3.2.3). The energy distribution of the particles is accordingly different:

- Maxwell-Boltzmann Flux Distribution (see fig. 3.22) for thermal desorption:

$$f(E,\theta) = 2\cos\theta \frac{E}{(k_B T_S)^2} \exp\left(-\frac{E}{k_B T_S}\right) \tag{3.10}$$

  where E is the energy of the ejecta and θ is the angle between the velocity vector of ejecta and the normal to the surface. T_S is the surface temperature.

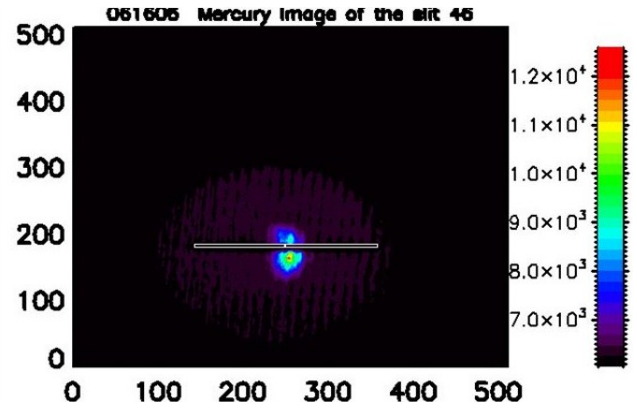

(a)

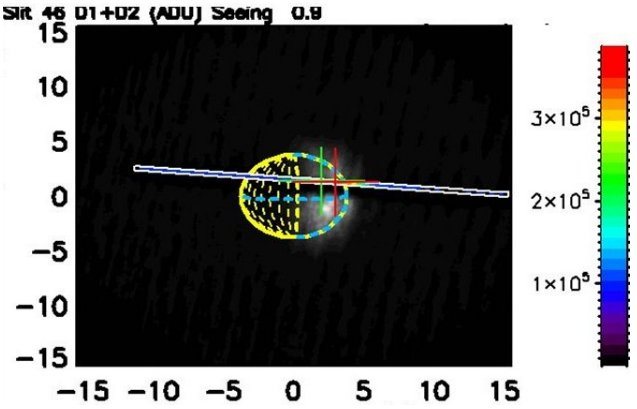

(b)

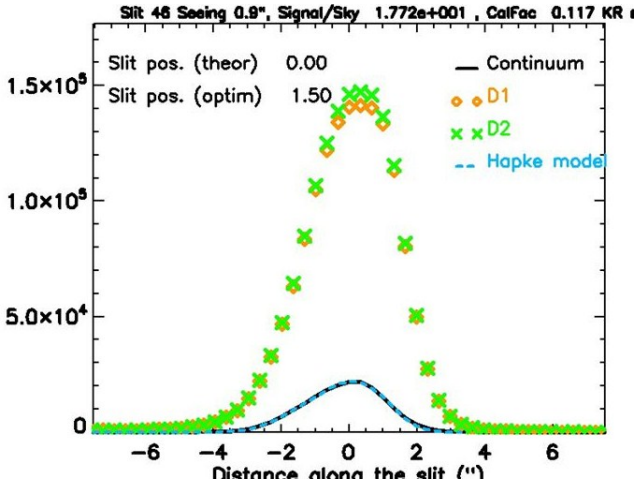

(c)

Figure 3.21: Top: the counts in the slit are compared to counts in the slitview image, in order to have a better precision of the slit position. The axis units are in pixels on the slitview image. Middle: The comparison between the peak of counts and the peak of slitview allow determination of the calfactor. The axis units are in arcseconds on the slitview image. Bottom: The blue dashed line indicate the continuum from the Hapke model, which matches very well the observed continuum (black). Abscissae are distance from disk's centre along the slit (in arcsecs). Ordinates are in $ADU\ Angstrom^{-1}\ s^{-1}$.

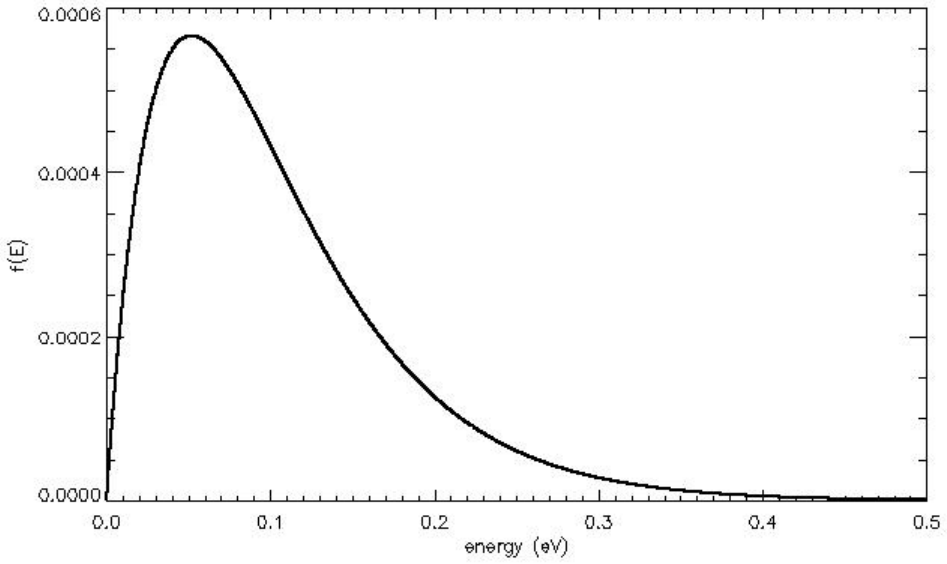

Figure 3.22: Normalized energy distribution for thermal desorption.

- Weibull distribution (see fig. 3.23) for photon-stimulated desorption:

$$f_{PSD}(E) = \beta(1+\beta)\frac{EU^{\beta}}{(E+U)^{2+\beta}} \tag{3.11}$$

  where E is the particle energy, U the characteristic energy for PSD and β the shape parameter of the distribution. I used $\beta_{Na} = 0.7$ and $U_{Na} = 0.098\,eV$ (Johnson et al. 2002).

- Sigmund-Thomposon (see fig. 3.24) for solar wind sputtering:

$$f(E,\theta) = 2\cos\theta\frac{2EU}{(E+U)^3} \tag{3.12}$$

  where θ is the angle between the ejection direction and the normal to the surface in the ejection point and $U = 0.27\,eV$ is the binding energy for sodium to be desorbed from an Na_2SO_4 surface (Wiens et al. 1997).

The angle between the normal at the surface and the direction of ejection, θ, is chosen, for all processes, from a distribution between 0 and $\pi/2$, peaked at $\pi/4$ - see histogram in fig. 3.25. The initial co-latitude is distributed between 0 (north pole) and π (south pole), with a peak at $\pi/2$ (equator) The initial azimuth, instead, is uniformly distributed between $-\pi/2$ and $+\pi/2$ (where 0 means subsolar point). See fig. 3.26 and fig. 3.27 for histograms of co-latitude and azimuth respectively.

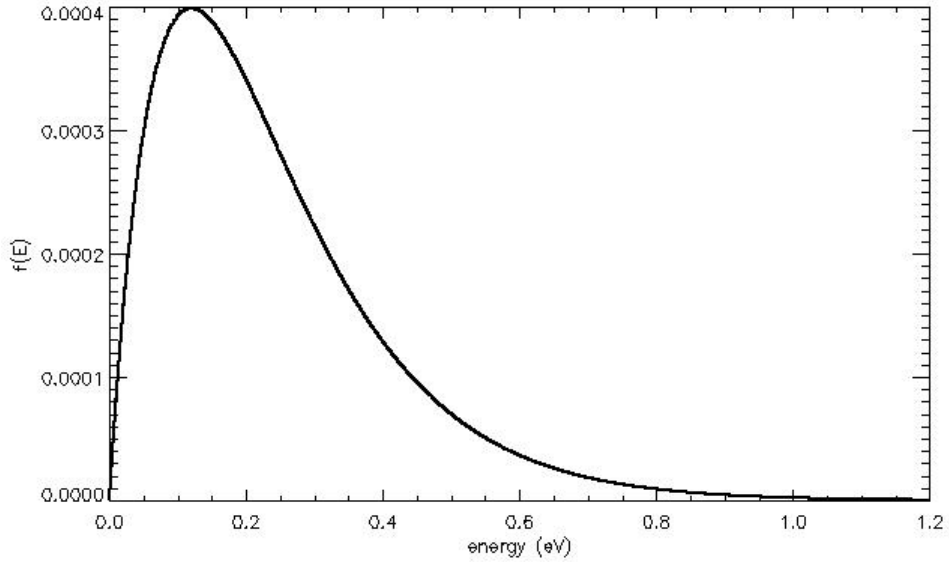

Figure 3.23: Normalized energy distribution for photon stimulated desorption.

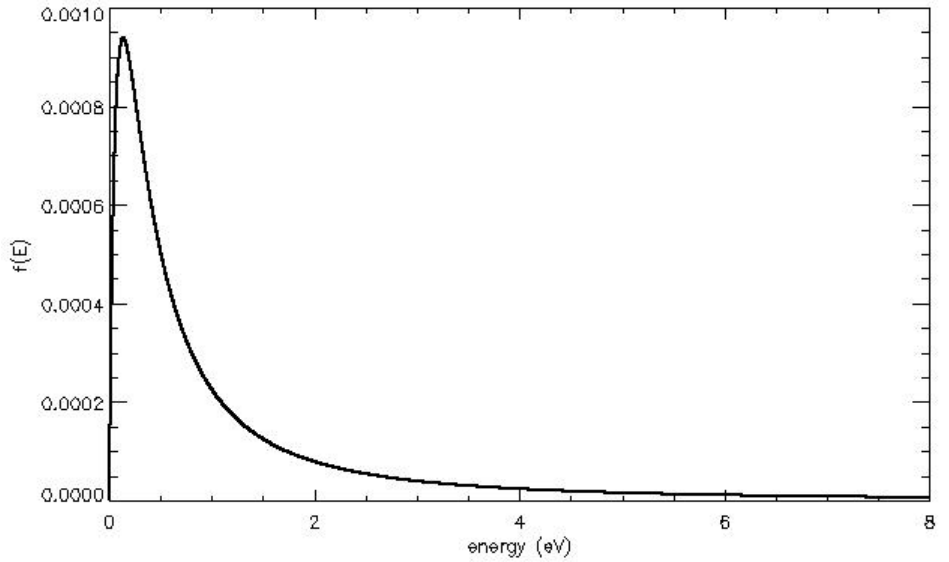

Figure 3.24: Normalized energy distribution for sputtering.

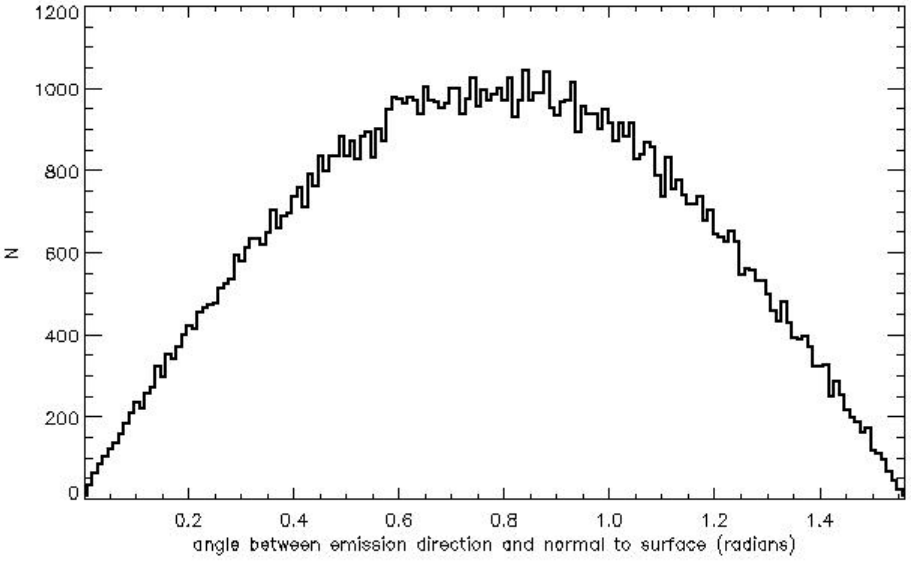

Figure 3.25: Histogram of θ, angle between ejection direction and normal to the surface.

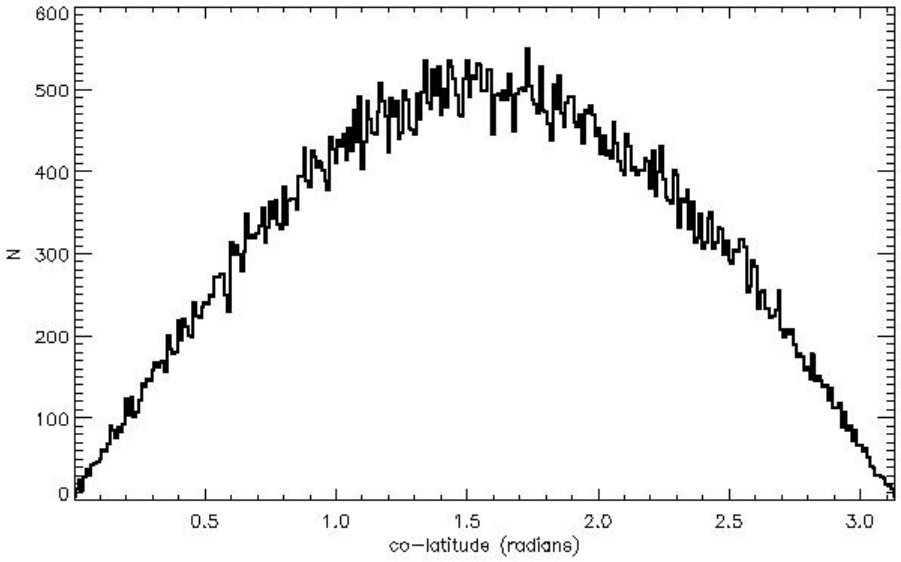

Figure 3.26: Histogram of co-latitude θ'. Here 0 means north pole, while π means south pole.

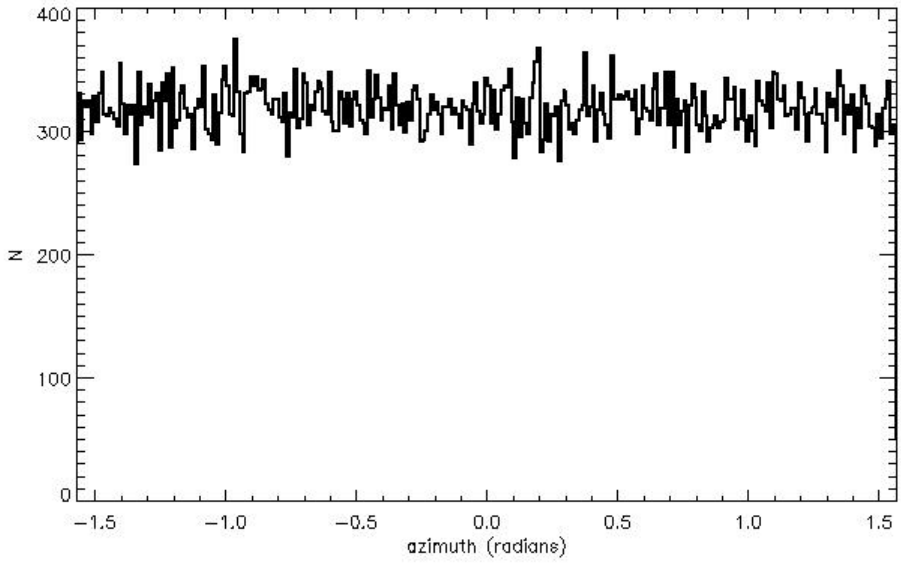

Figure 3.27: Histogram of azimuth. $\phi = 0$ means sunward direction.

Once the initial velocity has been chosen, the velocity is resolved in the x,y,z directions of a cartesian grid, where x represents the Sun-Mercury direction (positive x means pointing towards the Sun), z is the Ecliptic North Pole and y is directed accordingly.

A 4th order Runge-Kutta algorithm (Press et al. 2007) is then performed, with each particle followed under the sole effects of solar radiation pressure and Mercury's gravity. The former is taken into account only in the illuminated fration of the planet, i.e. particles are not accelerated back when reside in the Mercury's shadow. Position and velocity of each test particle after each time step ($\Delta t = 1\,s$) are recorded.

I ran the simulation for an integration time of 100τ, which is enough to reach a steady-state condition in which the number of particles present at each time step is constant - see fig. 3.28.

Particles that are ionized are removed from the routine. I've chosen a statistical method to check whether a particle is ionized or not. I generate a random number uniformly distributed between 0 and 1, and compare this number with the ratio $\Delta t/\tau$, where τ is the ionization lifetime (in my simulation, $\tau = 2.2$ hours). If $\Delta t/\tau >$ *random number*, the particle is ionized, and removed from the simulation.

Once a particle re-impacts the surface, it is re-inserted in the routine, from the impact point, with an initial velocity determined by the accommodation coefficient

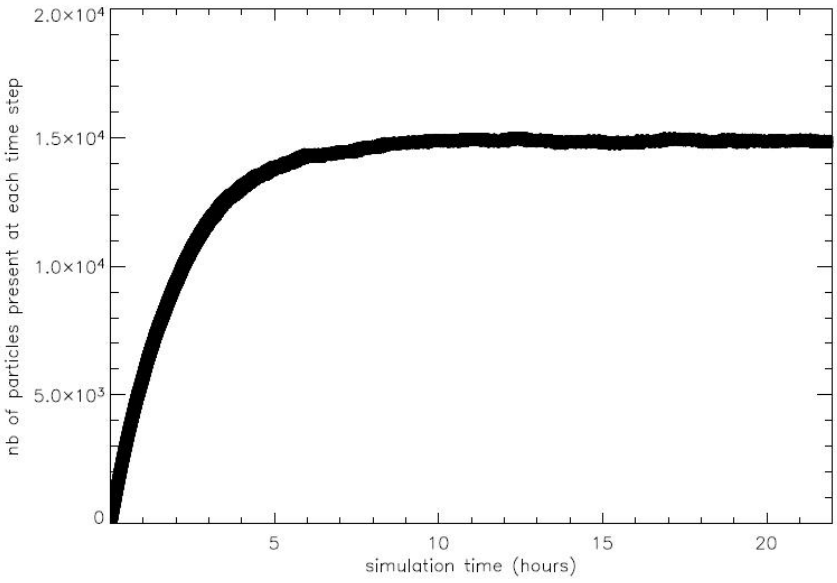

Figure 3.28: Number of test particles present at each time step as a function of simulation time. The steady-state is reached after ~ 5 hours of simulation time, i.e. $\sim 18000\ s$.

(Hunten et al. 1988):

$$\alpha = \frac{(E_{out} - E_{in})}{(E_{TS} - E_{in})} \tag{3.13}$$

where E_{in} is the energy of particle at the impact and E_{TS} is the energy in the limiting case of thermal equilibrium with the surface. This means that $E_{TS} = k_B T_S$. It is a rough approximation valid for heavy species but not for light species (Hodges 1980). E_{out} is the energy of the re-ejected particle. It is calculated from the previous energies, with the assumed value of $\alpha = 0.62$, valid for a surface temperature of 600 K, known from laboratory measurements. I then determined the value of E_{out} as $E_{out} = \alpha E_{TS} + (1 - \alpha) E_{in}$ and finally converted this into ejection velocity, with the assumption that the particle has only kinetic energy. The surface temperature present in E_{TS} is a function of the position (latitude and longitude) on the planet (Butler 1997):

$$T = T_0 + 100 \cdot |\cos\Theta \cos\phi|^{1/4} \tag{3.14}$$

where T_0 varies from 600 K at the perihelion to 475 K at the aphelion and the latitude Θ is computed from the co-latitude of impact site:

$$\Theta = \left| \frac{\pi}{2} - \theta \right| . \tag{3.15}$$

At the end of each time step I calculate in which cell of the density-grid-not-normalized (an array of 1000x1000x1000 elements in spherical coordinates) a test particle resides, and I add to this cell the time step.

At the end of the loop on time, I multiply each cell of the density-grid-not-normalized by the weight of each test particle, divide it by its volume element and by the total simulation time. In this way, I have another 1000x1000x1000 elements array which describes the number density in each cell. The volume of each cell is

$$dV = \frac{1}{3}\left[(\rho + d\rho)^3 - \rho^3\right] d\phi \cos\theta - \cos(\theta + d\theta) \tag{3.16}$$

where ρ is the radial distance from the center of the planet, and $d\rho$ the radial thickness of the cell. Here θ and ϕ are the co-latitude and the azimuth respectively. The weight of the test particle is found dividing the flux of particles from the whole planet N_{Na} by the number of test particles. I have taken $N_{Na} = 10^{23}\, atoms\, cm^{-2}\, s^{-1}$ (Wurz & Lammer 2003).

I finally integrate this density grid normalized along the observed line of sight, determined from the phase angle, that is the angle between Sun, Mercury and observer. This is done in order to have the projected column density (expressed in $atoms\, cm^{-2}$). Given that the tail is optically thin, I can find the intensity in Rayleighs I through the relation $I = g \cdot N$ (Hunten et al. 1988), where g is the g-factor (eq. 2.4) and N is the column density.

3.9 Results

The detection of a southern peak

The spectra I reduced have been used in Mangano et al. (2009), a work devoted to study the spatial distribution of sodium in the exosphere of Mercury. In this work an enhancement in the southern hemisphere of Mercury has been detected, see figures 3.29, 3.31 and especially 3.30.

This must be related to a local peak of release of the sodium trapped in the surface. In agreement with Leblanc et al. (2008), this peak could be related to the interplanetary space conditions, in particular to the *sign* of the B_x component (in the planet-Sun direction) of the interplanetary magnetic field (IMF). In these cases, a connection between the Hermean magnetic field and the IMF may allow solar wind particles to impinge on the surface through the magnetospheric cusps (section 3.2.3). A realistic IMF configuration with significantly $B_x > 0$ (< 0) causes reconnection mainly in the southern (northern) dayside magnetopause, wich a consequent particle precipitation and an enhancement due to solar wind sputtering. In order to have confirmation, data have been checked from ACE satellite, located at Sun-Earth lagrangian point L1, with the solar coronal magnetic field

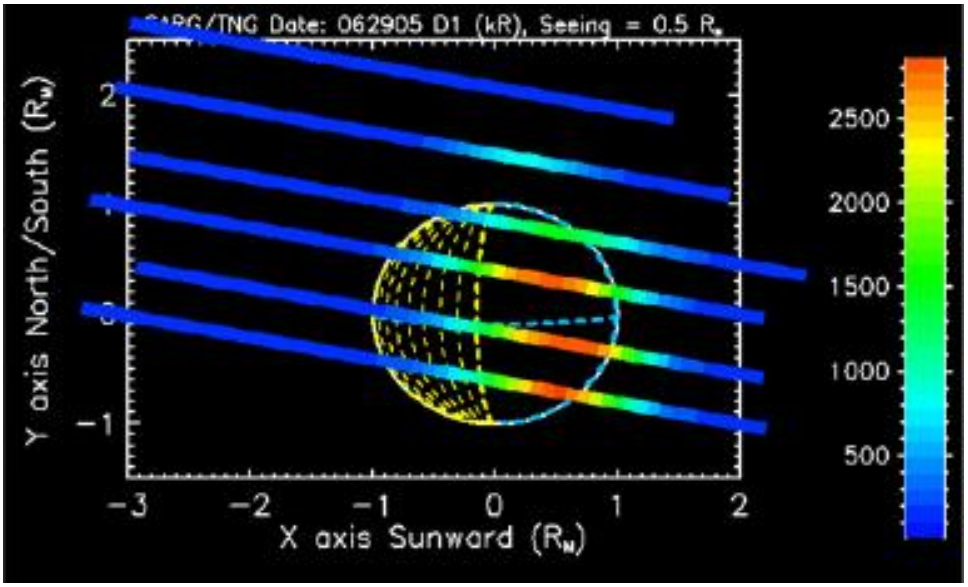

Figure 3.29: Brightness of Mercury during the first night.

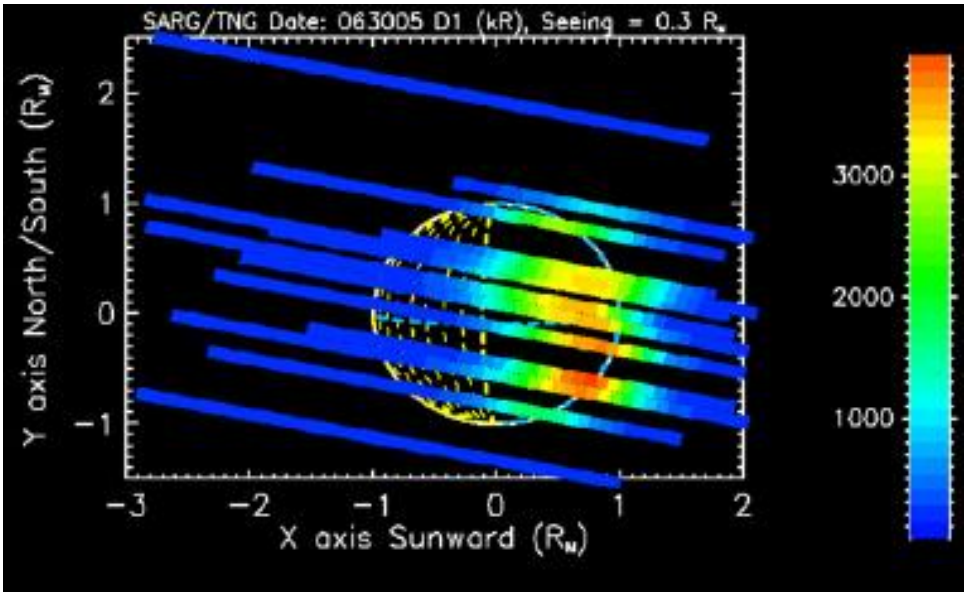

Figure 3.30: Brightness of Mercury during the second night.

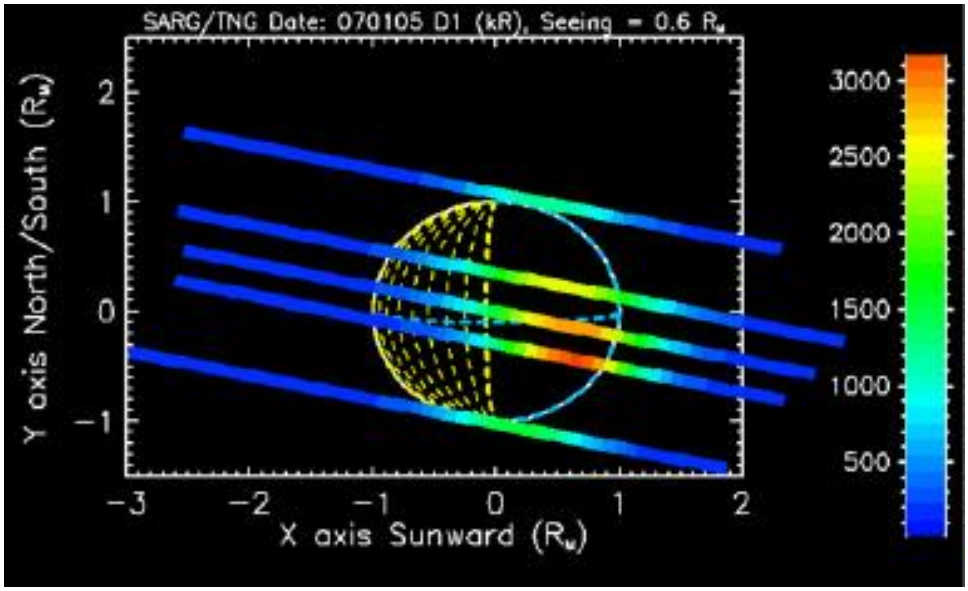

Figure 3.31: Brightness of Mercury during the third and last night.

extrapolated from photospheric measurements of Wilcox Solar Observatory. ACE data revealed that an interplanetary discontinuity, likely caused by the transit of a fast stream coming from a coronal hole, occurred 4 days before the TNG observations - see fig. 3.32, from Mangano et al. (2009). ACE detected a period of 6-7 days characterized by a slightly positive IMF B_x component ($\sim 2\,nT$) at Earth orbit. When scaled to the distance of Mercury, this translates in $B_x \sim 6 \div 12\,nT$ at Mercury. This IMF configuration is consistent with an asymmetric reconnection pattern with a large open cusp region in the southern hemisphere. A 10% fraction of the precipitating ion flux is able to reach the dayside planetary surface, leading to ion sputtering and thus to an enhancement in the sodium brightness. The geometry of the Ecliptic-plane IMF calculated by the Geophysical Institute of University of Alaska confirmed this fact. It is clearly seen (fig. 3.33) that during the three days of observations, Mercury lay in the positive sector of IMF (blue lines): $B_x > 0$, pointing thus towards the Sun.

Moreover, by inspecting the SOHO/LASCO CME catalogue, it turned out that several Coronal Mass Ejections (CMEs, see section 3.1.2) occurred during the period of observations as well as solar flares (sudden and intense brightness enhancements occurring in the solar corona, and emitting radiation with energy of $10^{27}\,erg\,s^{-1}$ as well as particles, including heavy ions). Observations from second night are indeed brigther than other two nights, as expected from a higher efficiency of solar wind sputtering, but the uncertainty of the calibration in Rayleighs (35%)

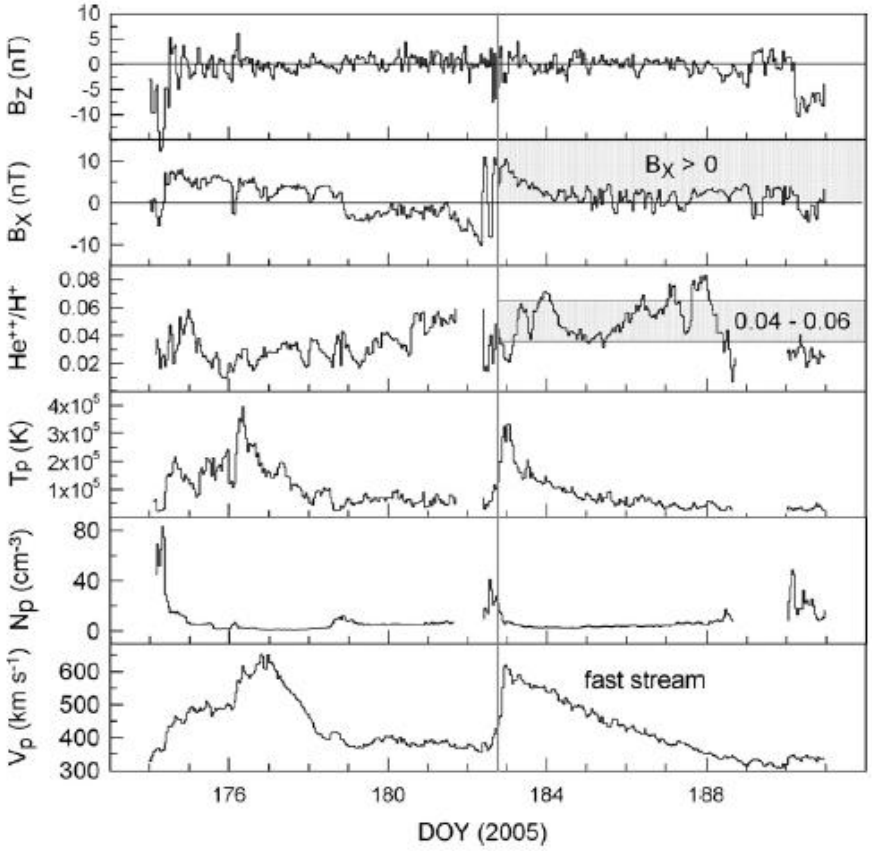

Figure 3.32: ACE data of (from top to bottom): IMF B_z and B_x components, He^{++}/H^+ ratio and proton temperature T_p, density N_p and velocity v_p. The vertical line indicates the fast stream arrival at Earth, which occurred at DOY 182. Scaling this at the Mercury's distance, it comes out that the fast stream must have interested Mercury 4 days before the TNG observations.

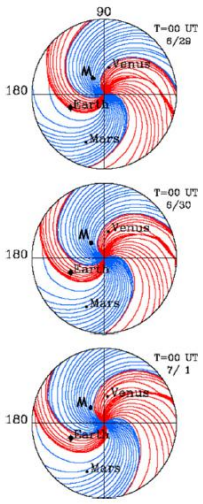

Figure 3.33: IMF geometry on the ecliptic plane during the three nights of observations. Red regions indicate $B_x < 0$, blue regions indicate $B_x > 0$.

hindered to state whether the observed enhancements were a real feature or not.

The anti-sunward sodium tail

Concerning my sodium tail model, I have used three different mechanisms of ejection. However, it was soon clear that thermal desorption and photon-stimulated desorption did not contribute much to the anti-sunward tail. See fig. 3.34, where the planet (in blue) is represented together with the very short tail generated exclusively from PSD. Atoms (red points) resides mostly near the illuminated surface, contributing only to a very small extent to the anti-sunward tail. This latter is negligible, especially if compared with the simulation where atoms were ejected through solar wind sputtering, see fig. 3.35. In both the plots, axis units are in Mercury Radii. x axis is the Mercury-Sun direction, pointing towards this latter, z axis is the North Pole and y axis is oriented accordingly. The importance of the solar wind sputtering is evident in the extension of the tail (up to 50 Mercury Radii). Clearly, too many particles ejected by PSD re-impact the surface and are later re-inserted in the exosphere by thermal desorption, an even weaker process.

Therefore, I considered only solar wind sputtering as the main ejection mechanism for test particles, and I proceeded in the calculation of the projected column density and of the brightness.

A 1D-scan in the anti-sunward direction is plotted in fig. 3.36(a). This has to be compared to the values observed by Potter et al. (2002), fig. 3.36(b), which spans

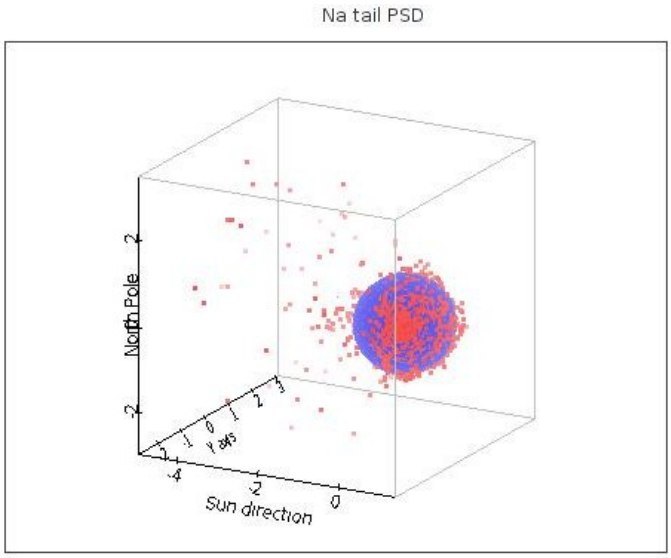

Figure 3.34: The anti-sunward tail with atoms ejected by PSD.

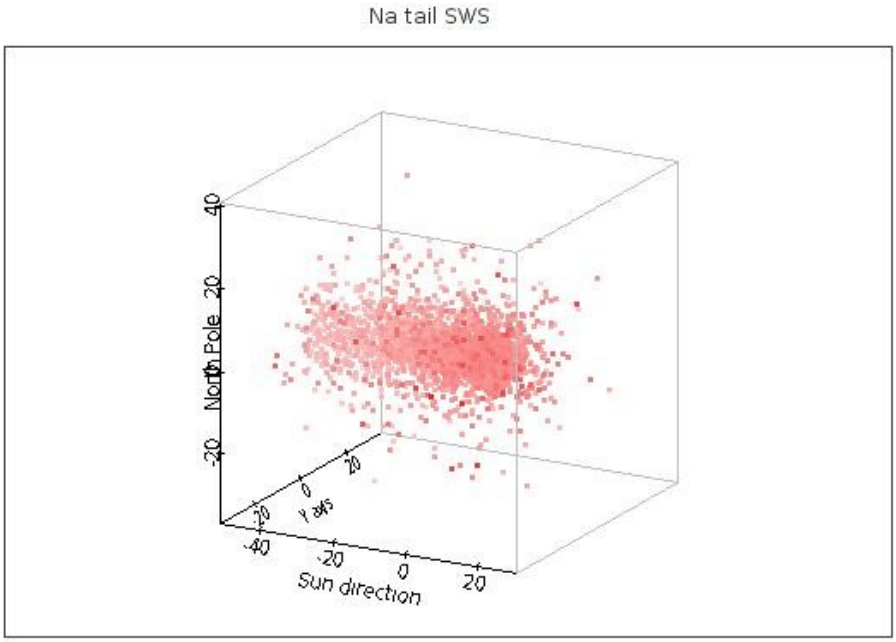

Figure 3.35: The anti-sunward tail with atoms ejected by solar wind sputtering.

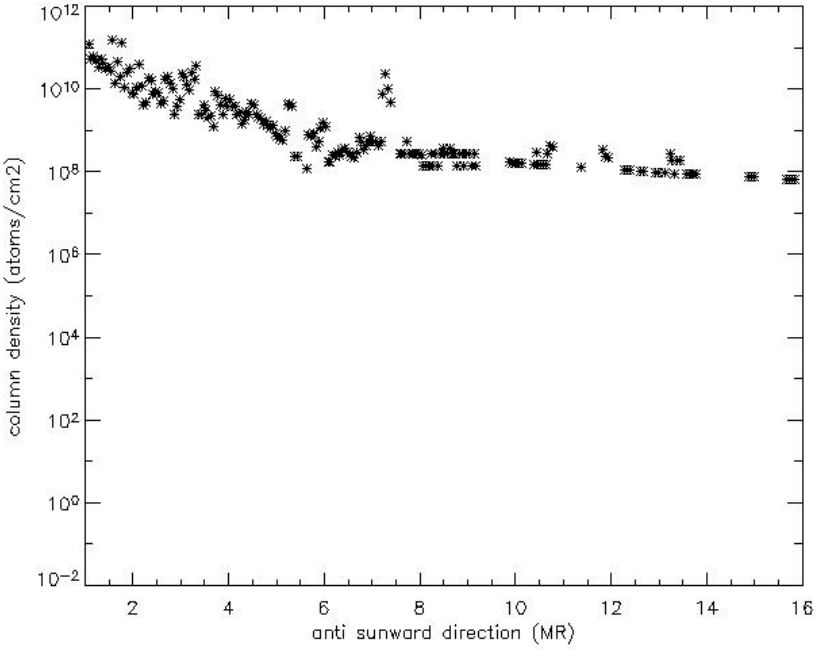

(a)

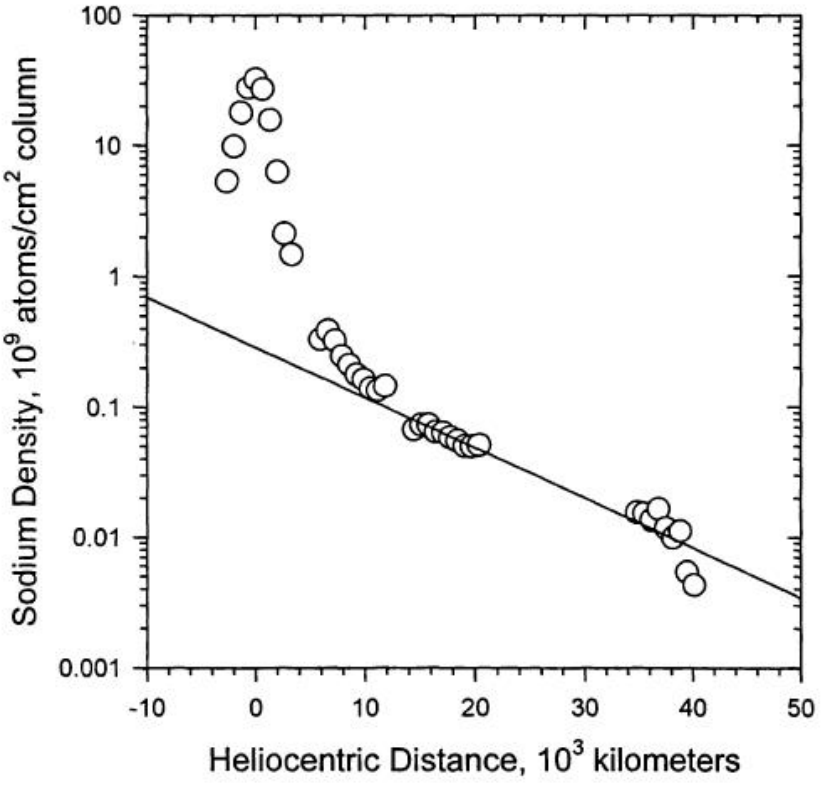

(b)

Figure 3.36: Top: column density projected in the anti-sunward direction. Bottom: observed column density in the Mercury sodium tail. The axis range for the two plots are comparable, being 16 $R_{\mathbb{Q}} \approx 40000\,km$.

approximately the same range in the anti-sunward direction ($16R_{\mercury} \approx 40000\,km$). My model predicts ~ 10 times more column density with respect to the observations, but the descending trend is fairly well reproduced. In both cases it follows a $1/b^2$ law, where b is the distance from the centre of the planet. The conversion in Rayleighs will be possible (and observations will be explained) once this 1-order-of-magnitude higher counts will be solved. Nevertheless, the fair agreement between observations and prediction seem to suggest that the problem lies in the conversion between number density ($atoms\,cm^{-3}$) and projected column density ($atoms\,cm^{-2}$) rather that in a severe bug of the routine, suggesting that it will be fixed soon.

3.10 Conclusions on the work on Mercury

In this part of the thesis I have illustrated the twofold approach I have used to study the innermost planet of the Solar System. On side, the observational work shed light on the interaction between magnetosphere and exosphere of Mercury: a change in the magnetospheric configuration induced by an abrupt increase of the solar activity causes an enhancement of sodium atoms sputtered by solar wind particles, which in turn led to an increase in the brightness of exospheric emission. This is an example of how a study of the interaction surface-exosphere-magnetosphere can be accomplished by observing the amount of light scattered by the escaping sodium atoms in the exosphere.

On the other hand, I've also adopted a theoretical approach to study the anti-sunward sodium tail of Mercury. Although not yet completed, the model is however at a good point of development, because it matches quite well the observed column densities in the tail. Another important result of the model is that it predicts a virtually non-existent sodium tail in the case atoms are emitted by processes other than solar wind sputtering. Once the model will be developed, it will serve as a tool to understand the observations.

4

Other Bodies of the Solar System

4.1 Lutetia

Lutetia has been chosen among a list of possible candidates for fly-by of Rosetta spacecraft on the basis of it interesting properties. With a diameter of roughly 100 km, Lutetia was the largest asteroid of the list. It was also the only object of the list which allowed the radio science experiment to measure the mass, and consequently to deduce the bulk density. Lutetia was classified as M-type asteroid, and supposed to be a parent body of iron meteorites, by several authors in the late 80s and early 90s because of the high IRAS (Infrared Astronomical Satellite) albedo of of 0.208 ± 0.025 (Mueller et al. 2006). However, its infrared spectrum is unusually flat compared to other M asteroid Burbine & Binzel (2002). The observations obtained at IRTF suggested a similarity with the carbonaceous chondrite spectra which characterize the C-type (CV3 or CO3) asteroid (Birlan et al. 2004). They suggested that these types of chondrites are characterised by low carbon contents, which could explain the relative high albedo compared to other types. All of of the info available for Lutetia were consistent with a primitive composition, except the high IRAS albedo value. These are the reasons that pushed Barucci et al. (2005) to suggest Lutetia as the best candidate for the flyby of Rosetta.

In view of this event, I have been involved by the Osiris Team in Padova in a modelization of the sodium exosphere of Lutetia, if there exist one. Aim of this work was also to establish the exposure times for OSIRIS-WAC instrument equipped with the Na filter.

4.1.1 The Rosetta spacecraft

Rosetta is an european spacecraft, launched in March 2004, which for the first time will enter orbit around the nucleus of a comet (67/P Churyumov-Gerasimenko, in August 2014) and release a lander (*Philae*) onto its surface, that

will operate for at least a week, sending back very high resolution pictures as well as information about the upper crust of the nucleus. Rosetta will continue its observations of the comet's nucleus for over a year, at least until December 2015, to monitor the "awakening" of the comet's activity as it comes closer to the Sun and reached its perihelion, in October 2015.

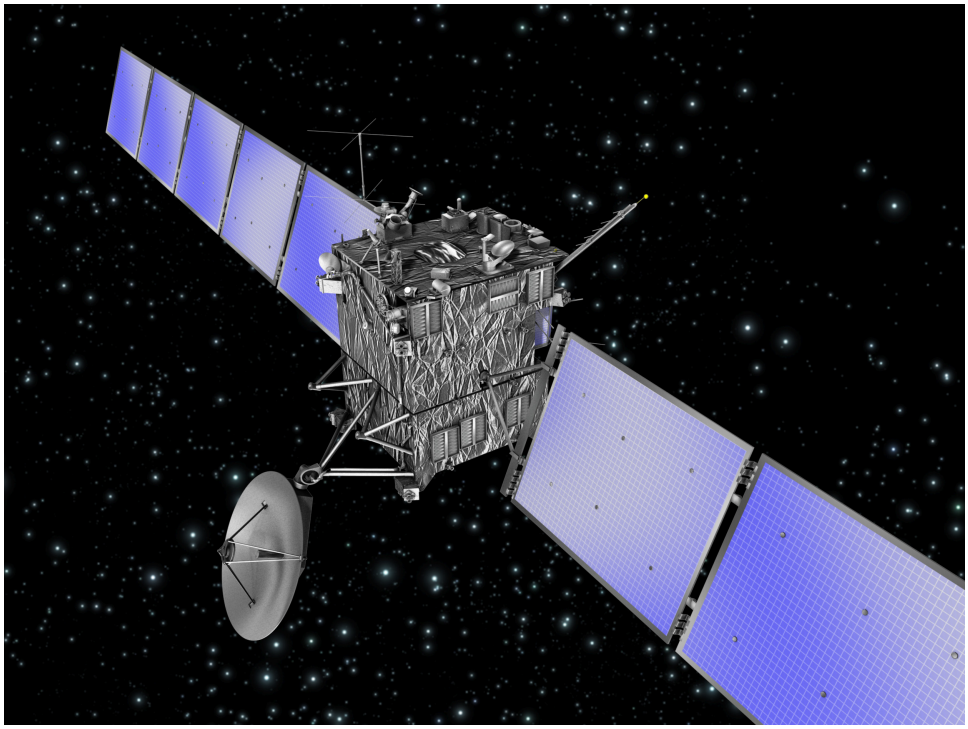

Figure 4.1: Artist's impression of the spacecraft Rosetta (courtesy ESA).

On its journey to the comet spacecraft Rosetta performed several flybys: at the Earth - Moon system (March 2005, November 2007, November 2009), Mars (February 2007, when it flew at only 200 km from the surface) and asteroids Steins (September 2008) and Lutetia (July 2010). Among its various instruments, the high-resolution camera OSIRIS (Optical Spectroscopic and Infrared Remote Imaging System) is the most suitable to study sodium exospheres. It consists of two different telescopes: the Wide Angle Camera (WAC) and the Narrow Angle Camera (NAC). This latter is designed for high spatial resolution while the former has a wide field of view (11°×12°). In particular, the WAC has a sodium filter mounted on one of its two filter wheels. The image scale of WAC is $7.4 mrad\, mm^{-1}$, that is 101 $\mu rad\, pix^{-1}$, and its wavelength range is $240 \div 720\, nm$. Parameters of the Na and Vis610 filters of WAC are summarized in tab. 4.1.

Table 4.1: Characteristics of Na and Vis610 filters of WAC

Parameter	Na	Vis610
Wavelength (nm)	590.7	612.6
Bandwidth (nm)	4.7	9.8
Peak Transmission (%)	59.0	83.4
Thickness at centre (mm)	4.75	4.65

4.1.2 The Lutetia exosphere model

I developed a model of exosphere of asteroid Lutetia starting from the formula for the density of a planetary exosphere:

$$\rho(d) = n_0 \cdot \frac{R_L^2}{d^2} \cdot \exp\left(\frac{-(d - R_L)}{\tau\, v}\right) \tag{4.1}$$

where n_0 is the exospheric surface density, R_L is the Lutetia Radius, v is the velocity of the expanding cloud, τ the ionization time (as an e-folding distance) d the position from the center of the asteroid.

Given a reference frame centred on Lutetia (see fig. 4.2, view from the Ecliptic North Pole), the y axis being in the Sun-Lutetia direction pointing away from the Sun (that is, the line-of-sight direction), the z axis towards the Ecliptic North Pole and the x axis accordingly, I've chosen several points in the x and y direction, and I calculated the distance as $d = \sqrt{x^2 + y^2}$.

I have then performed an integration of the calculated density in the y direction to get column density along the line of sight, as the spacecraft flew by having the Sun approximately behind it. I have taken into account the presence of the asteroid and therefore stopped the integration at Lutetia's disk.

I have chosen $n_0 = 10^7\, atoms\, m^{-3}$, which is the amount of sodium expected to be supplied by solar wind sputtering, probably the most efficient process in the supply of Na atoms (Schläppi et al. 2008). Different combinations of velocity and ionization time have been taken into account. I have chosen ionization lifetimes between 1 hours and 48 hours. Photo-ionization is weaker than for the case of Mercury, that's why I have chosen an upper limit so high. Concerning the velocity of the expanding cloud, I have chosen values between 1 and 4 $km\, s^{-1}$.

4.1.3 Results

Here I report results from the following combinations: 1 and 48 hours of ionization time, and an expanding velocity of 1 and 4 km/s. The column density so

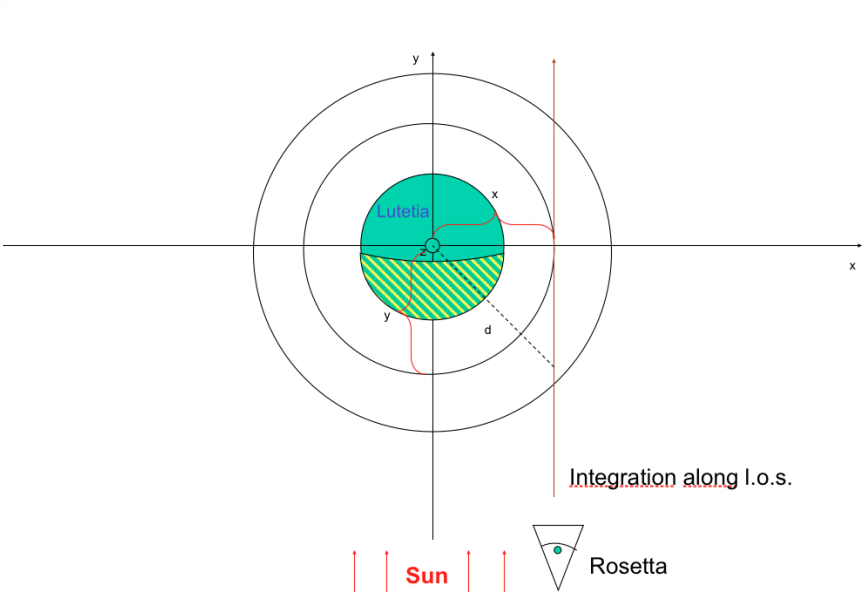

Figure 4.2: Scheme of the integration used in the Lutetia's exosphere model.

obtained has been multiplied by the g-factor in order to get brightness in Rayleighs: the used values of 2.97 AU and $-1.94\,km/s$ for the heliocentric distance and radial velocity, respectively, have been inferred from Horizons webpage and used to calculate g-factor (see section 2.3). A value of $7.87 \times 10^{-2}\ s^{-1}$ for the g-factor of the D2 line has been obtained. The brightness in Rayleighs has been plotted, for different combinations of velocity and ionization times, in fig. 4.3 and 4.4.

As the g-factor is considerably low, and the expected zenith column density for Lutetia, $4.5 \times 10^{-11}\ atoms\,m^{-2}$ (Schläppi et al. 2008) is roughly 2 orders of magnitude lower than that of the Moon (Killen & Ip 1999), the maximum predicted brightness on Lutetia never exceeds 1 Rayleigh, or 2-3 orders of magnitude lower than on the Moon (Sarantos et al. 2010), for all the combinations of ionization time and velocity taken in considerations. I proposed thus to use the largest available exospure time, that is 120 sec, available only at 9 hours before the closest approach.

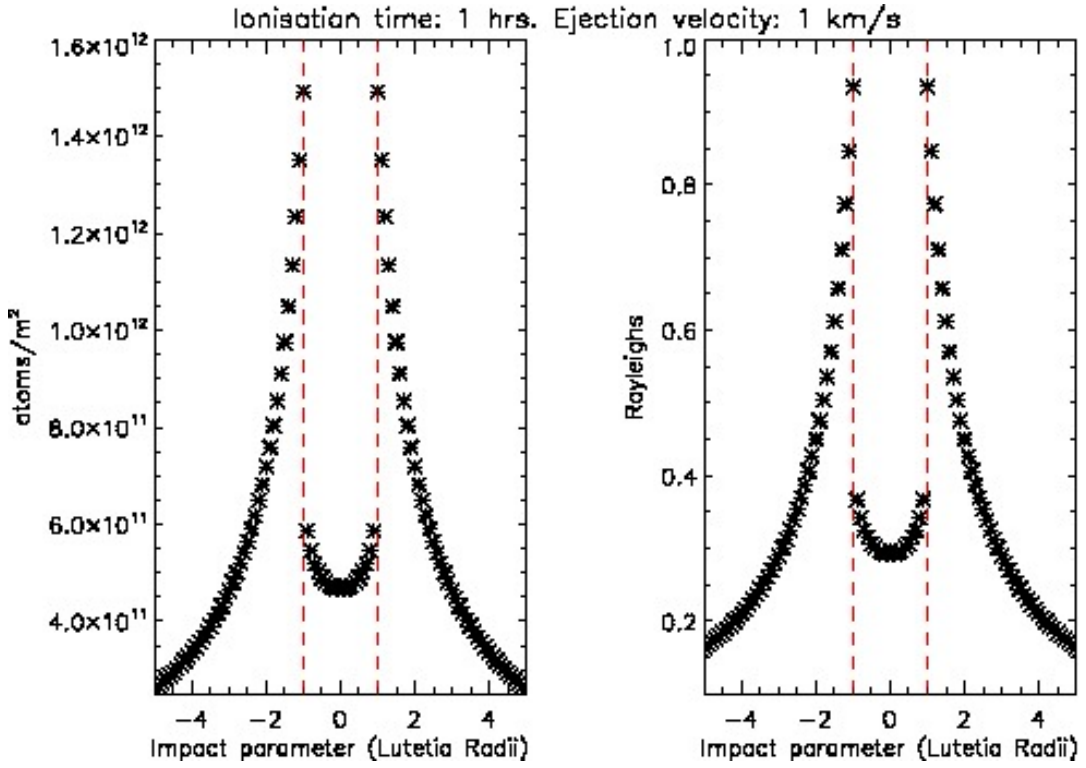

(a)

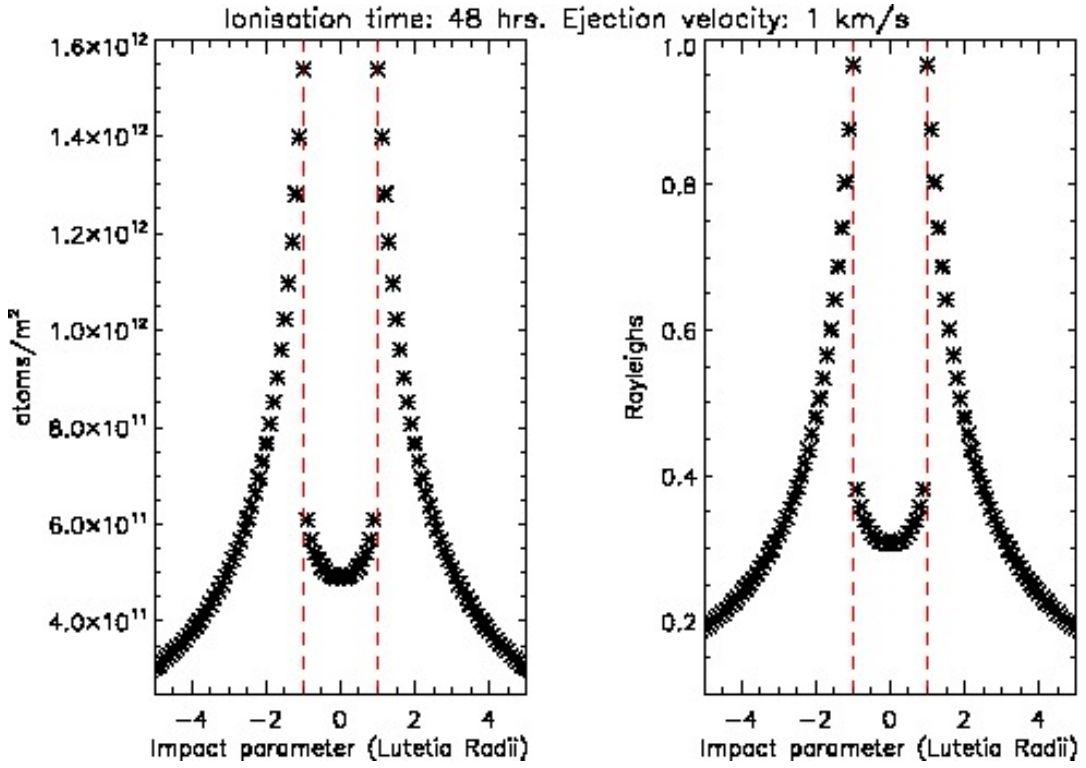

(b)

Figure 4.3: Lutetia's column density and brightness, ejection speed 1 km/s.

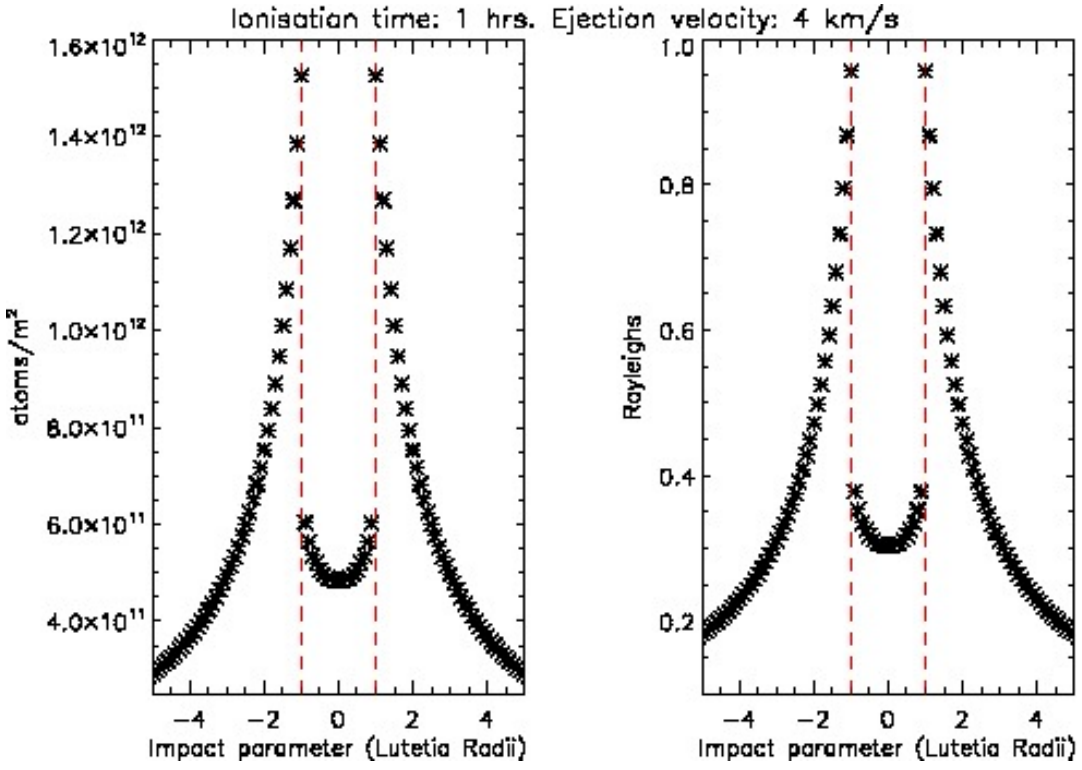

(a)

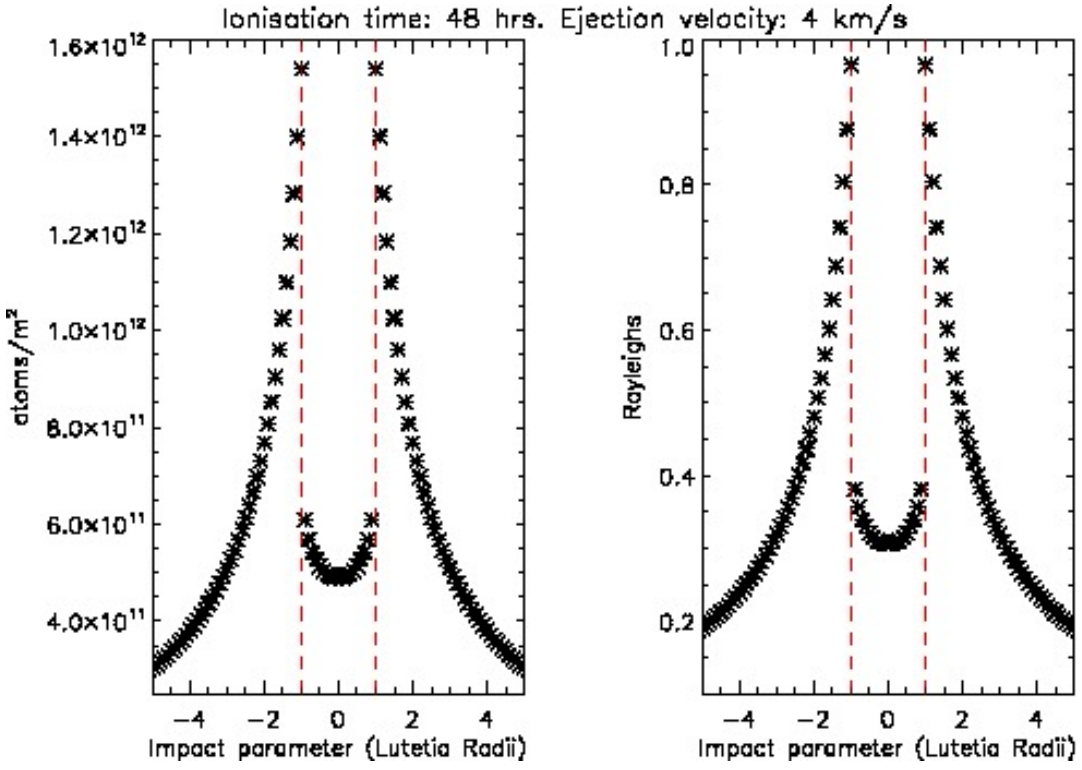

(b)

Figure 4.4: Lutetia's column density and brightness, ejection speed 4 km/s.

4.1.4 The fly-by of Rosetta spacecraft

Fly-by of asteroid Lutetia took place on July 10th 2010. The spacecraft flew at a distance of $3170\,km$ at a relative speed of $15\,km\,s^{-1}$, leaving the entire planetary community astonished by the quality of the images that were downloaded - see fig. 4.5. However, images taken with the WAC camera equipped with the Na filter

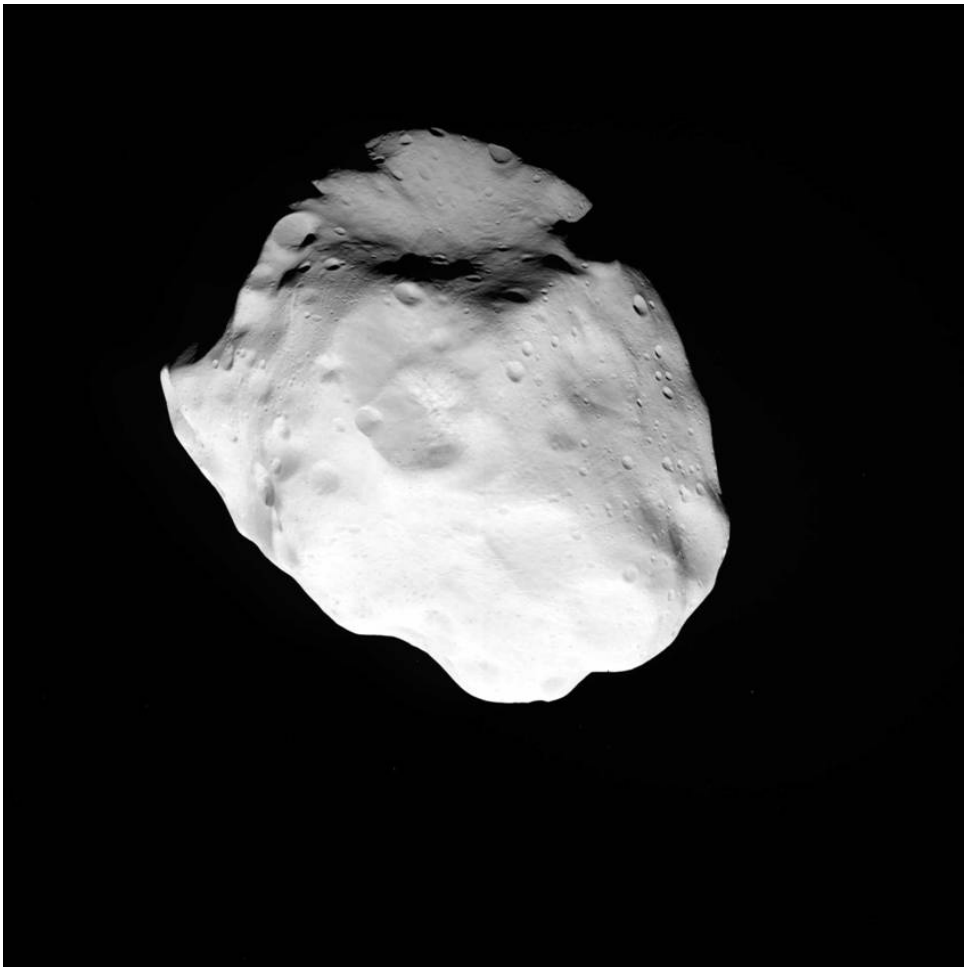

Figure 4.5: Lutetia as seen by Rosetta's spacecraft.

that were sufficiently longer for detection of exospheric sodium were obtained 9 hours before closest approach, when the spacecraft was at $\sim 5 \times 10^5\,km$ of distance and the asteroid occupied few pixels on the detector.

The analysis consisted in the subtraction of the continuum by using the Vis610 filter of WAC. This has to be scaled to Na filter images by multiplying it for a constant factor, 1.03, which takes into account the different bandwidth of the fil-

ters, the different transmission efficiency and the different exposure times. Once I removed the continuum from the Na images, I faced the same problems encountered in the reduction of same data of the Moon (see section 4.3.1): diffuse light, ghosts, diffraction rays overwhelmed the light coming from the asteroid - see fig. 4.6.

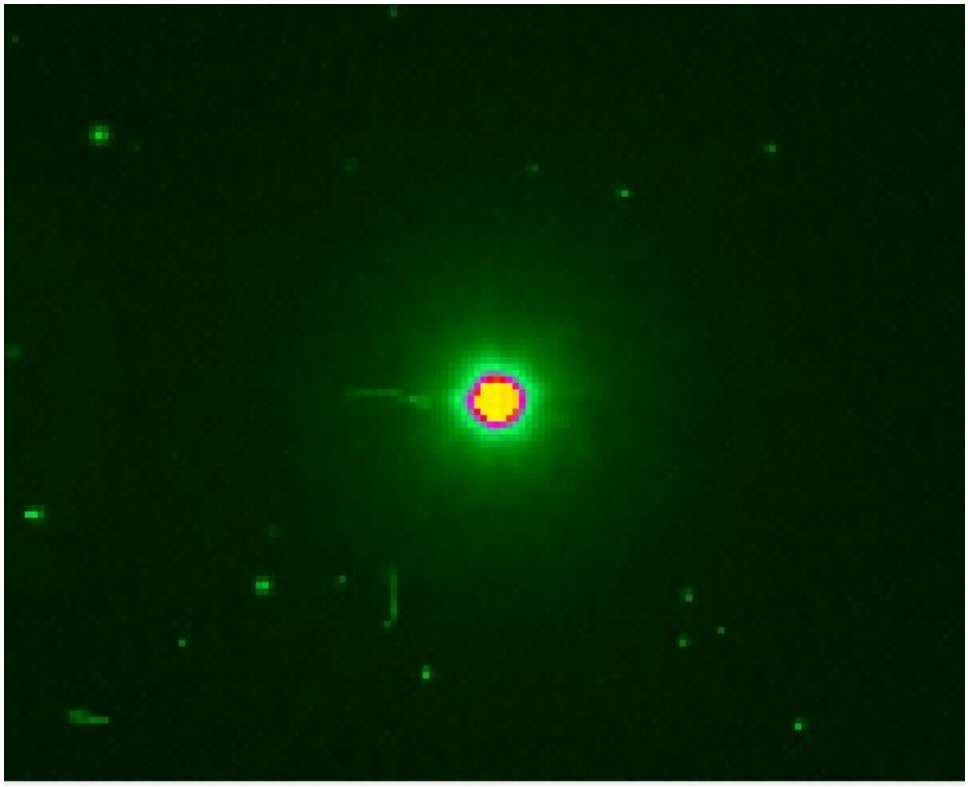

Figure 4.6: Ghost images and diffuse straylight at Lutetia.

I then tried to remove light around the asteroid using a mask around the disk, in order to get light only from a corona encircling the object - see fig. 4.7. But when the subtraction has been performed, diffuse light was present also here - see fig. 4.8.

The yellow features just northwards of the asteroid's disk in fig. 4.8 could have been indicative of sodium detection, however when I performed the calibration in Rayleighs I found that these features are caused by diffuse straylight not properly subtracted, given its count 3 orders of magnitude greater than the expected - see fig. 4.9. The images will be re-analyzed as soon as the team devoted to subtraction of straylight will manage to fix these severe problems. Anyway, the estimate of brightness of asteroid Lutetia has been calculated for the first time.

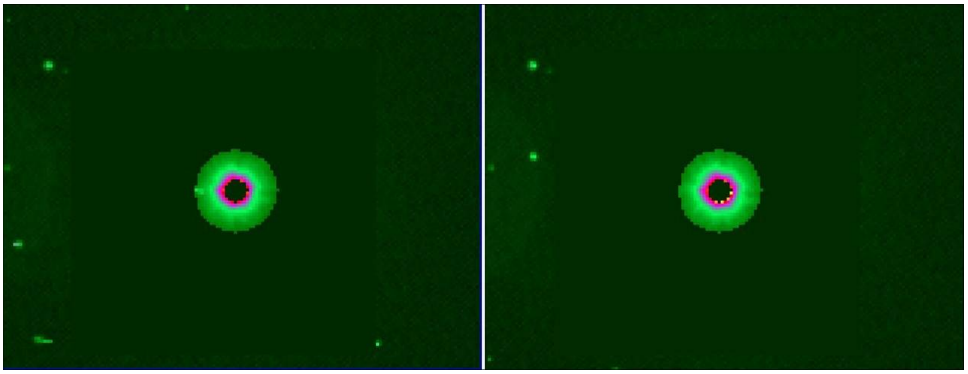

Figure 4.7: A mask is superimposed on Lutetia's disk, in an attempt to decrease contribution from straylight. Images taken at 9 hours from the closest approach. The left image is taken with the Na filter, exposure time 120 sec. The right image is taken with the Vis610 filter, exposure time 44 sec.

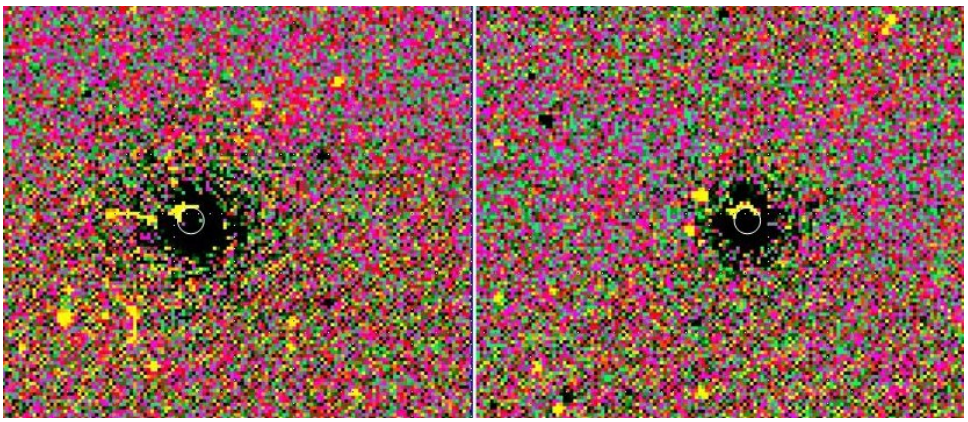

Figure 4.8: Subtraction Na-Vis610 leaves anyway spurious features, even with a mask superimposed on the asteroid's disk (white circle). Left image: greatest exposure time (120 sec); right image: shortest exposure time (60 sec).

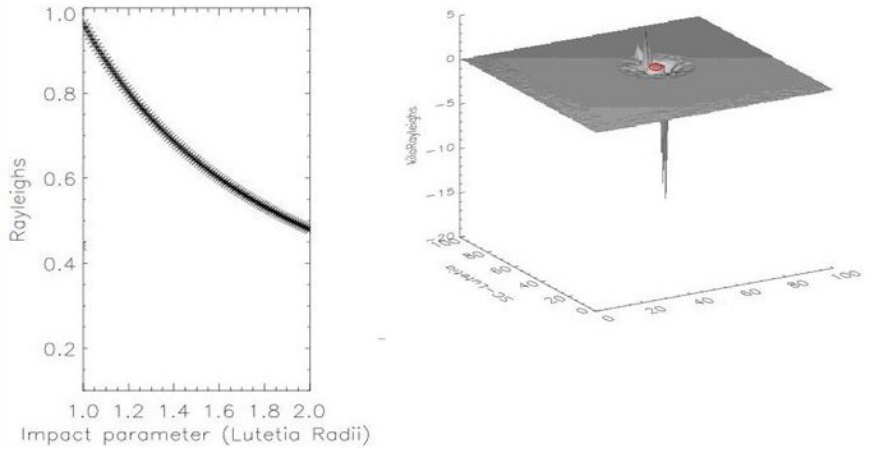

Figure 4.9: Right: a surface plot of the counts from subtracted image Na-Vis610, exposure time 120 sec (left image in fig. 4.8). The position of the asteroid (masked) disk is indicated by a red circle. The counts from the upper part of the mask are of the orders of 5 kiloRayleighs. Too much if compared to the predicted emission at Lutetia (left plot). The highly negative peak is also indicative of poor subtraction, due to the diffuse straylight.

4.2 Europa

Europa has its own extended atmosphere too. The sodium corona was discovered by Brown & Hill (1996). They showed that Europa atmosphere contains a significant escaping component in addition to the previously known bound component. It was observed up to 25 R_E (1 R_E = 1569 km). They suggested that this sodium is originally released by Io's volcanoes, after which it is ionized in the magnetosphere and implanted into Europa's surface ice. Subsequent sputtering of the ice by magnetospheric ions releases the sodium to form the extended atmosphere. They found that the ratio D2/D1 is 1.70 ± 0.05, consistent with the expected value of 1.66 of optically thin emission. Therefore column density is directly proportional to the emission intensity. The density at Europa's surface is $\sim$ 70 $atoms\,cm^{-3}$, 100 times smaller than the extrapolated surface density of sodium at Io (Schneider et al. 1991a), and its column density is 10^{10} cm^{-2}. The extent of sodium distribution implies that atoms are leaving the surface at high velocity: 2 km/s to reach a height of 25 R_E. Since sublimation at Europa surface temperature of 95 K will produce typical velocities of only 0.3 $km\,s^{-1}$, the most likely mechanism for generating the required high velocities is **sputtering** by energetic magnetospheric particles. Nowadays, however, it is not sure at all

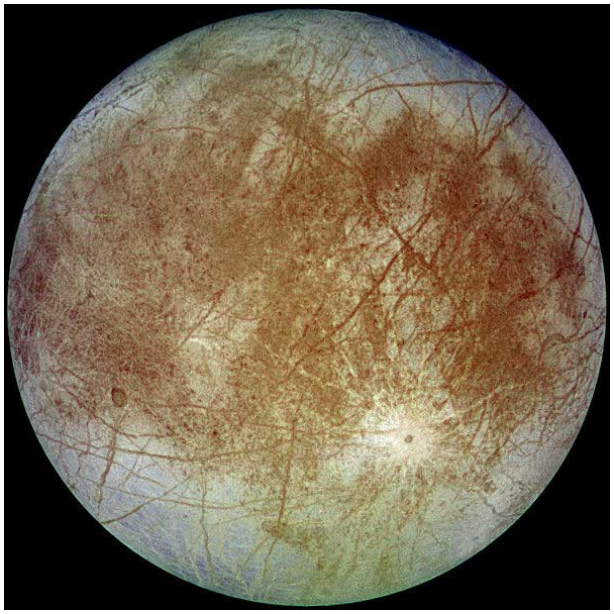

Figure 4.10: Europa moon as seen from Galileo spacecracft.

that sodium is brought there from Io. In fact, it has been argued that sodium might be endogenic at Europa. Its surface is exposed to an intense flux of energetic ions and electrons trapped in Jupiter's magnetic field (Paranicas et al. 2001). Therefore, the ultimate source of sodium and potassium for Europa's atmosphere could also be the radiation-induced decomposition of a surface brine (Johnson et al. 2002). This is thought to be material from Europa's putative underground ocean which may have reached the surface at various times in the past. If this is the case, then the sputter-produced atmosphere should contain other species from this ocean which might be detected by remote sensing (Johnson et al. 1998). The observation of alkalis at Europa is consistent with models suggesting that Europa has frozen, hydrated salts on its surface (Zolotov & Shock 2001). Charged particle irradiation can preferentially deplete such materials of sodium (Madey et al. 1998), leaving behind, for instance, the frozen hydrated sulfuric acid suggested by Galileo spacecraft data (Carlson et al. 1999).

One primary clue for the origin of Europa's sodium cloud is the column abundance variation around the orbit. Previous observations centered in the four quadrants of Europa's orbit found a variation factor of 5 of the sodium emission intensity: Leblanc et al. (2005) inferred a net sodium source at Europa by combining observations with modeling of the interaction between Jupiter magnetospheric plasma and Europa surface. They found that the net ejection from Europa exceeded the possible supply from Io, and inferred a Europa source. Later, Cipriani

et al. (2008) modeled the same data and proposed that a transient plasma event in Jupiter magnetosphere caused the observed variability. They showed that a minimal sodium source of $3 \times 10^6\, cm^{-2}\, s^{-1}$ is required to produce the average emission intensities observed by Leblanc et al. (2005). Both hypotheses are consistent with the observations, therefore new, specific observations are required to try to clear up this ambiguity.

4.2.1 Observations

I therefore decided to exploit the new observing time allocated following the discovery of the new unexpected emission (see section 2.9) to study also Europa. This time a non-standard observing mode has been chosen, i.e. withouth the sodium filter. This technique, which has disadvantage in that light from adjacent orders can affect the orders of interest, has on the other hand unique capabilities to detect simultaneous emissions from other elements. The full spectral range of spectrograph SARG covers the wavelengths from 4534 to 7918 Å, so multi-species detetion is possible, allowing for example to map for the first time the sodium and oxygen spatial distribution on Io and Europa during their orbit. I performed observations of all medicean satellites, this time with the consciousness that Europa was at the same time reference object (to subtract sunlight from Io) and target (to study temporal variability of its sodium cloud). Moreover, with 7 consecutive (half) nights that were granted, I could observe the satellites in all four possibile quadrants during their orbit, allowing detection of temporal variability of their sodium clouds. See tables 4.2 and 4.3 for the orbital parameters of Io and Europa, respectively, and figures 4.11 and 4.12. for the geometry of observations.

4.2.2 Preliminary Results

Reduction steps have been concluded only recently, however some preliminary results have been presented. In fig. 4.13 (Schneider et al. 2010) I report the sodium brightness at Io and at Europa in the four quadrants where they have been observed. These showed temporal variability of a factor of 5 during the orbit of Europa, confirming that there exists "season" at this satellite. In the figure the value relative to the offsets north and south of the target are also reported, as we performed such scans with an exposure time identical than that for the satellites. Moreover, the possibility to detect K simultaneously allowed us to compute the Na/K ratio. In fact, this is the main indicator to state whether sodium is endogenic at Europa or not. Preliminary analysis showed that this turned out to be from 19 to 50 at Europa and from 8 to 70 at Io. The discrepancy between the two ranges seems to confirm that sodium is endogenic at Europa.

Table 4.2: Io orbital parameters for observations at TNG in 2009.

Sep. 7^{th}											
Spectrum:	# 1	# 2	# 3	# 4							
Orbital long. (deg)	235	249	251	253							
Hel. rad. vel. (km/s)	13.57	15.62	15.83	16.01							
Earth-Io vel. (km/s)	26.55	28.46	28.65	28.81							
Sep. 8^{th}											
Spectrum:	# 1	# 2	# 3	# 4							
Orbital long. (deg)	93	95	97	99							
Hel. rad. vel. (km/s)	-17.78	-17.73	-17.68	-17.60							
Earth-Io vel. (km/s)	-4.85	-4.71	-4.59	-4.42							
Sep. 9^{th}											
Spectrum:	# 1	# 2	# 3	# 4	# 5	# 6	# 7	# 8			
Orbital long. (deg)	268	270	271	273	278	286	288	289			
Hel. rad. vel. (km/s)	16.83	16.85	16.85	16.84	16.71	16.26	16.12	15.95			
Earth-Io vel. (km/s)	29.72	29.70	29.68	29.63	29.42	28.86	28.70	28.50			
Sep. 10^{th}											
Spectrum:	# 1										
Orbital long. (deg)	157										
Hel. rad. vel. (km/s)	-8.77										
Earth-Io vel. (km/s)	6.62										
Sep. 11^{th}: bad weather											
Sep. 12^{th}											
Spectrum:	# 1	# 2	# 3	# 4							
Orbital long. (deg)	187	189	191	193							
Hel. rad. vel. (km/s)	1.39	1.98	2.57	3.11							
Earth-Io vel. (km/s)	17.78	18.38	18.98	19.54							
Sep. 13^{th}											
Spectrum:	# 1	# 2	# 3	# 4	#5	#6	# 7	# 8	# 9	#10	#11
Orbital long. (deg)	12	14	16	19	26	28	31	35	36	39	45
Hel. rad. vel. (km/s)	-3.95	-4.75	-5.20	-5.98	-7.97	-8.51	-9.26	-10.28	-10.76	-11.31	-12.74
Earth-Io vel. (km/s)	4.16	8.25	7.83	7.12	5.32	4.84	4.18	3.30	2.87	2.41	1.20

Table 4.3: Europa orbital parameters for observations at TNG in 2009

Sep. 7^{th}				
Spectrum:	# 1			
Orbital long. (deg)	299			
Hel. rad. vel. (km/s)	12.11			
Earth-Europa vel. (km/s)	23.78			
Sep. 8^{th}				
Spectrum:	# 1	# 2	# 3	
Orbital long. (deg)	34	36	37	
Hel. rad. vel. (km/s)	-6.61	-7.16	-7.36	
Earth-Europa vel. (km/s)	4.74	4.28	4.11	
Sep. 9^{th}				
Spectrum:	# 1	# 2		
Orbital long. (deg)	148	149		
Hel. rad. vel. (km/s)	-9.15	-8.97		
Earth-Europa vel. (km/s)	5.18	5.39		
Sep. 10^{th}				
Spectrum:	# 1	# 2	# 3	
Orbital long. (deg)	243	247	252	
Hel. rad. vel. (km/s)	10.90	11.40	12.01	
Earth-Europa vel. (km/s)	25.13	25.67	26.31	
Sep. 11^{th}: bad weather				
Sep. 12^{th}				
Spectrum:	# 1	# 2	# 3	# 4
Orbital long. (deg)	83	88	91	96
Hel. rad. vel. (km/s)	-13.72	-14.03	-14.14	-14.25
Earth-Europa vel. (km/s)	0.25	0.24	0.29	0.46
Sep. 13^{th}				
Spectrum:	# 1	# 2		
Orbital long. (deg)	195	202		
Hel. rad. vel. (km/s)	1.26	3.08		
Earth-Europa vel. (km/s)	17.80	19.76		

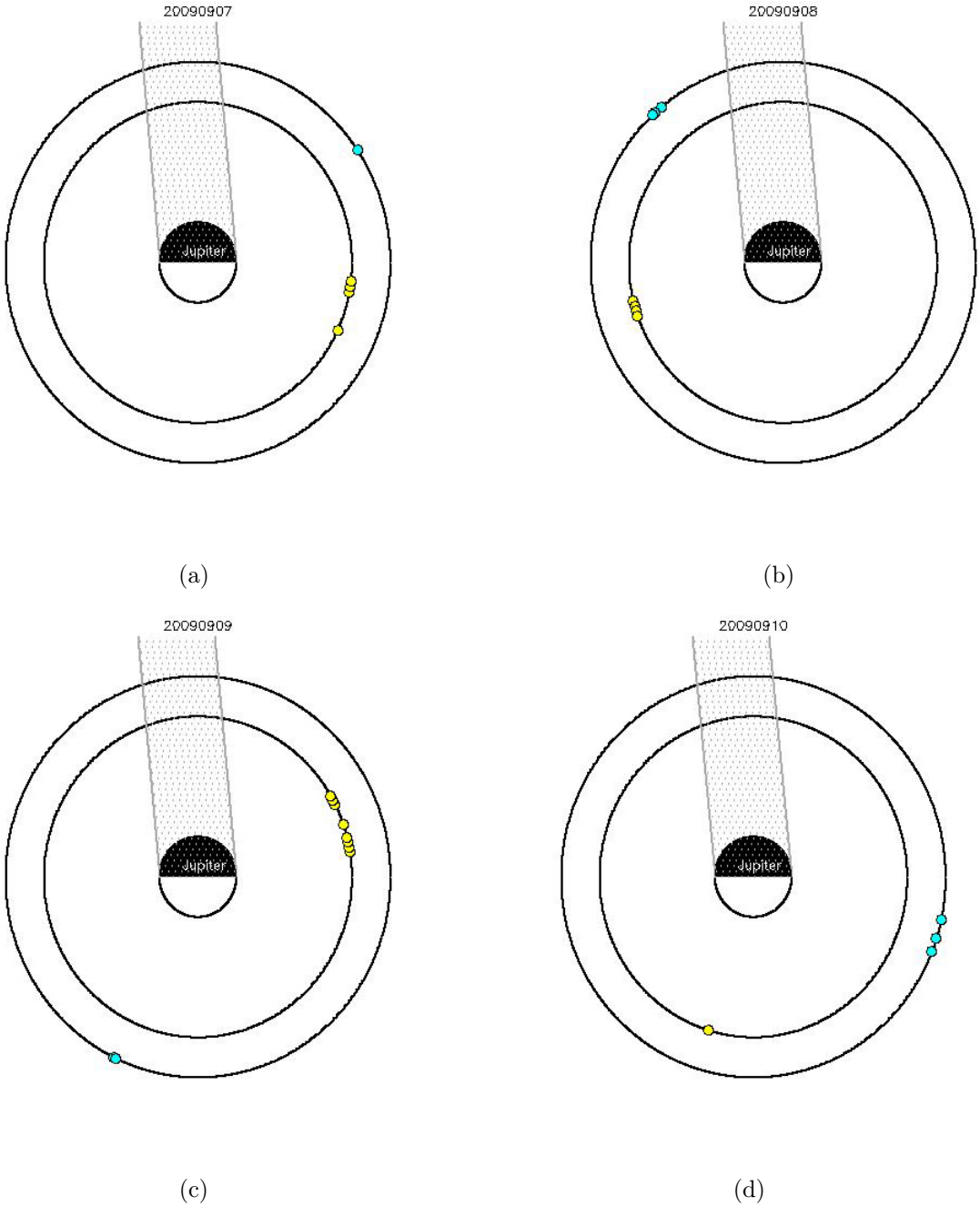

Figure 4.11: The geometry of observations of Io (yellow) and Europa (cyan) for the first four nights in 2009.

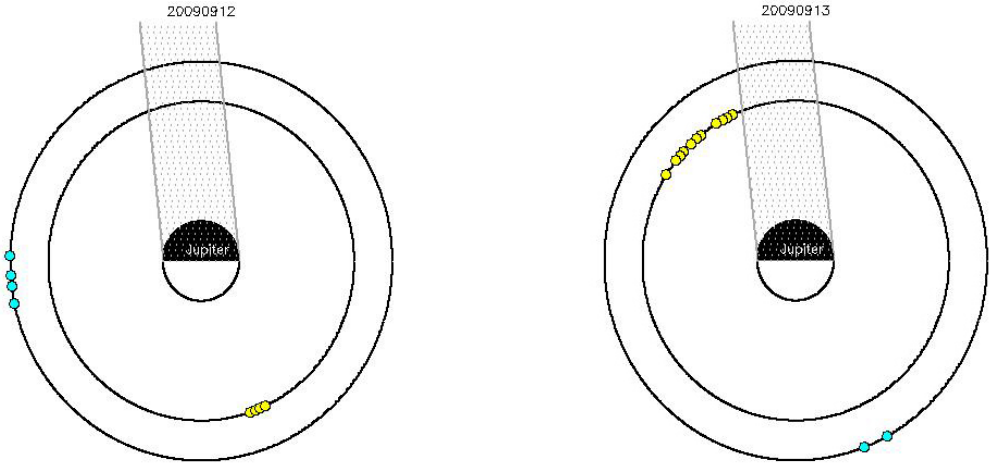

Figure 4.12: The geometry of observations of Io (yellow) and Europa (cyan) for the last two nights in 2009.

We went at TNG also to further investigate the new, unexpected features discovered during my work on Io (section 2.9). Unfortunately, the night when Io was coming out from Jupiter's eclipse (Sep. 11^{th}) was affected by bad weather, and the other night when Io was at the same quadrant of past observations (i.e., orbital longitude from 90°to 180°) only the first half night was assigned to us, and we could observe Io when it was closer to western elongation rather than superior conjunction (see fig. 4.11(c)). We did not detect the blueshifted emission during that night. Instead, we were puzzled to detect a redshifted feature, still in the Jupiter-side hemisphere, when Io was in inferior conjunction - see fig. 4.14. Observations clearly revealed that we are missing some pieces in the comprehension of the interaction between plasma torus and Io's atmosphere. The models we started to develope will have to take into consideration also this new element in order to explain these observations.

One of the key aspects of these "non-standard" observations, as already mentioned, is the possibility of multi-species detection. After having used the K emission to investigate the Na/K ratio, we searched for the emission of oxygen at Io's rest reference. Indeed, I've found an emission feature right at the exact position predicted for the forbidden "red" atomic oxygen emission at the Doppler shift of Io - see fig. 4.15. It is visible when Io was at western elongation (figure 4.11(c)), i.e. has an enough high Doppler shift to move the emission out of the telluric emission at 6300.29 Å. A spectral profile is provided in fig. 4.16. In the plot is

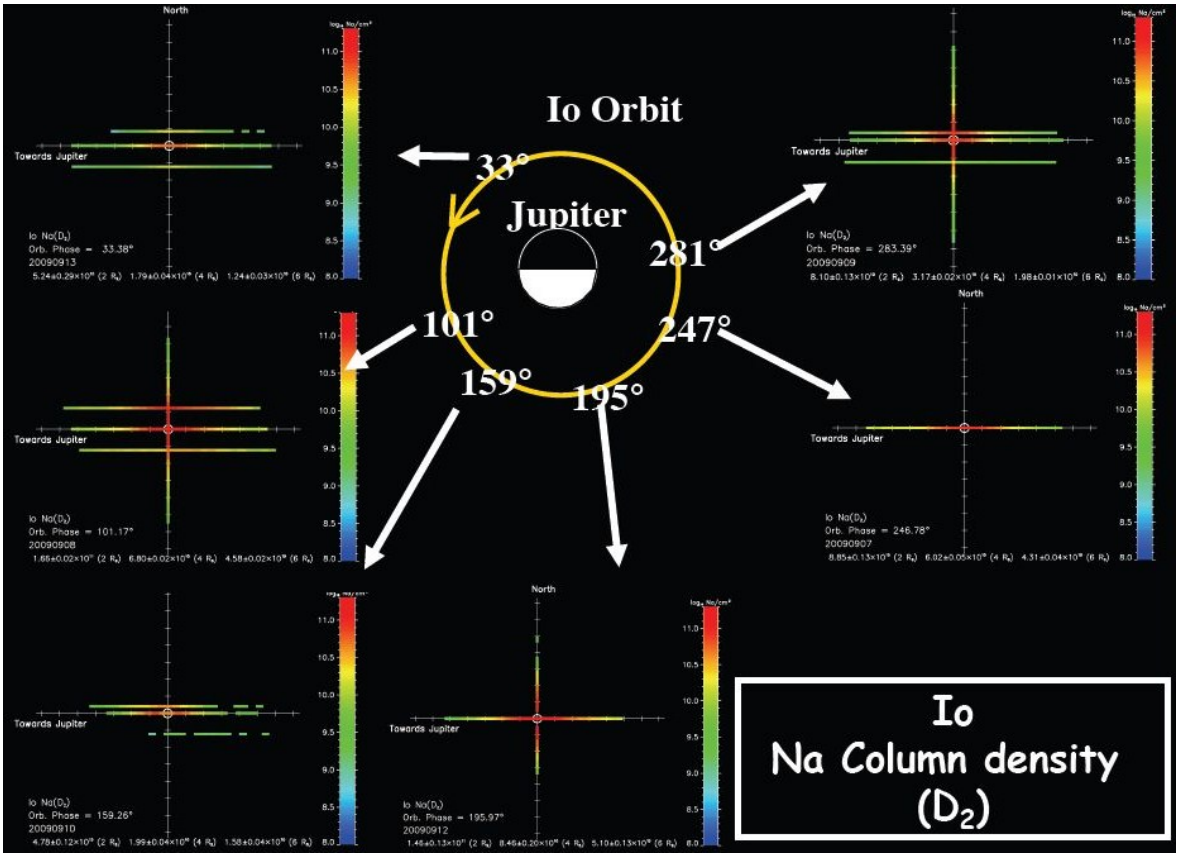

(a)

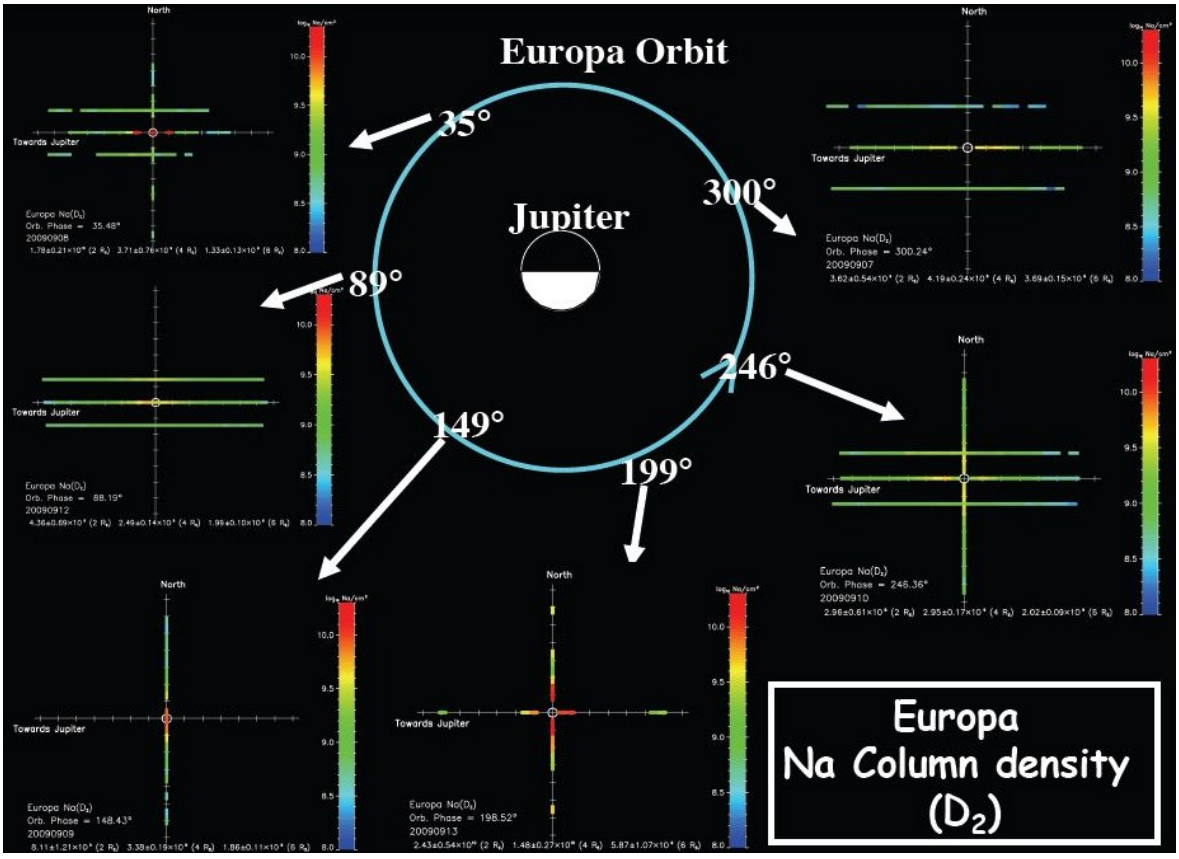

(b)

Figure 4.13: The sodium emission of Io (top) and Europa (bottom) is seen to vary with orbital longitude.

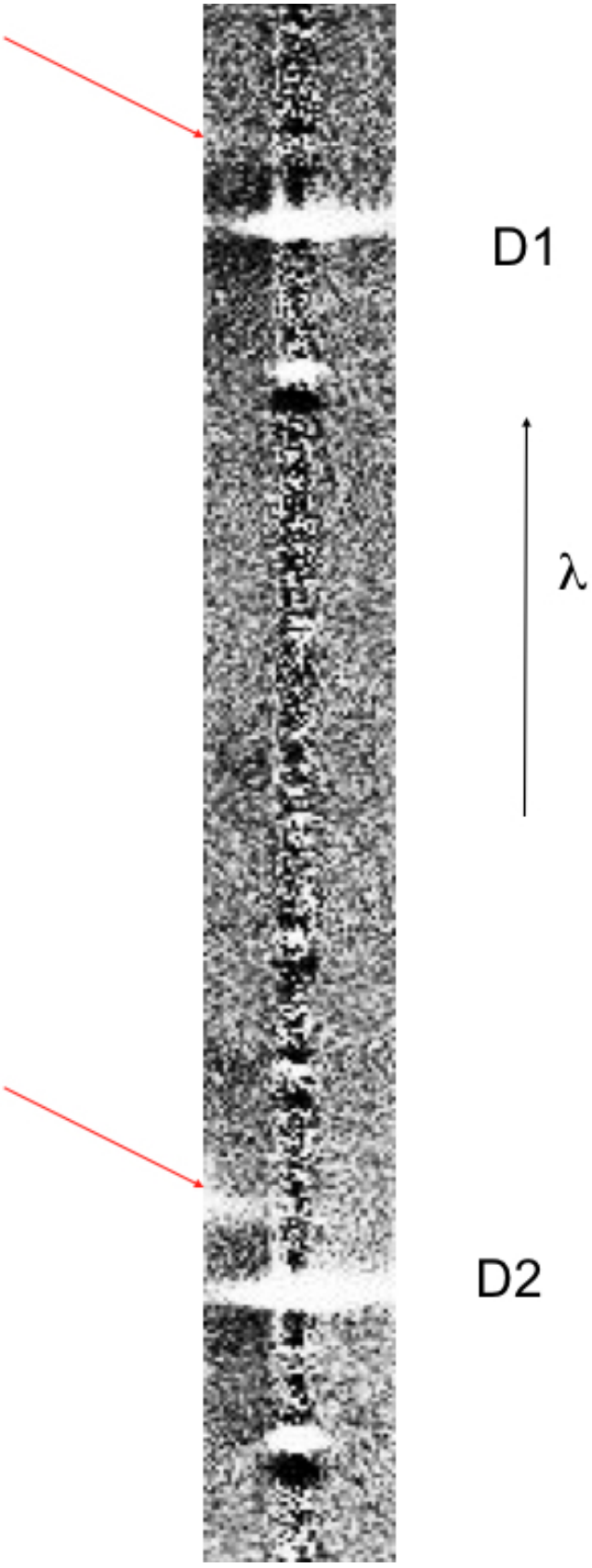

Figure 4.14: The redshifted feature appears upwards of the principal exospheric emission and leftwards (i.e. Jupiterwards). It is indicated by the red arrows. This is last Io spectrum of 6^{th} night - fig. 4.12 left panel.

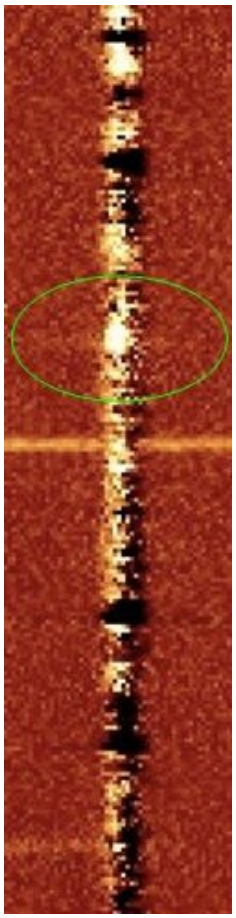

Figure 4.15: First spectrum of the third observing run (geometry in figure 4.11(c)) around the region of atomic oxygen. The emission, possibly iogenic, is encircled by the green ellipse. The bright, narrow and extended emission that fills the slit width bluewards of the iogenic emission is the telluric atomic oxygen. Jupiter is on the left side. At the bottom of the spectrum another telluric emission from an adjacent order is visible in the left side (atomic oxygen, at 6363 Å).

indicated the telluric emission (red, dashed line) together with the position predicted at Io for the emission of OI (purple, dotted line at 6300.93 Å). If confirmed,

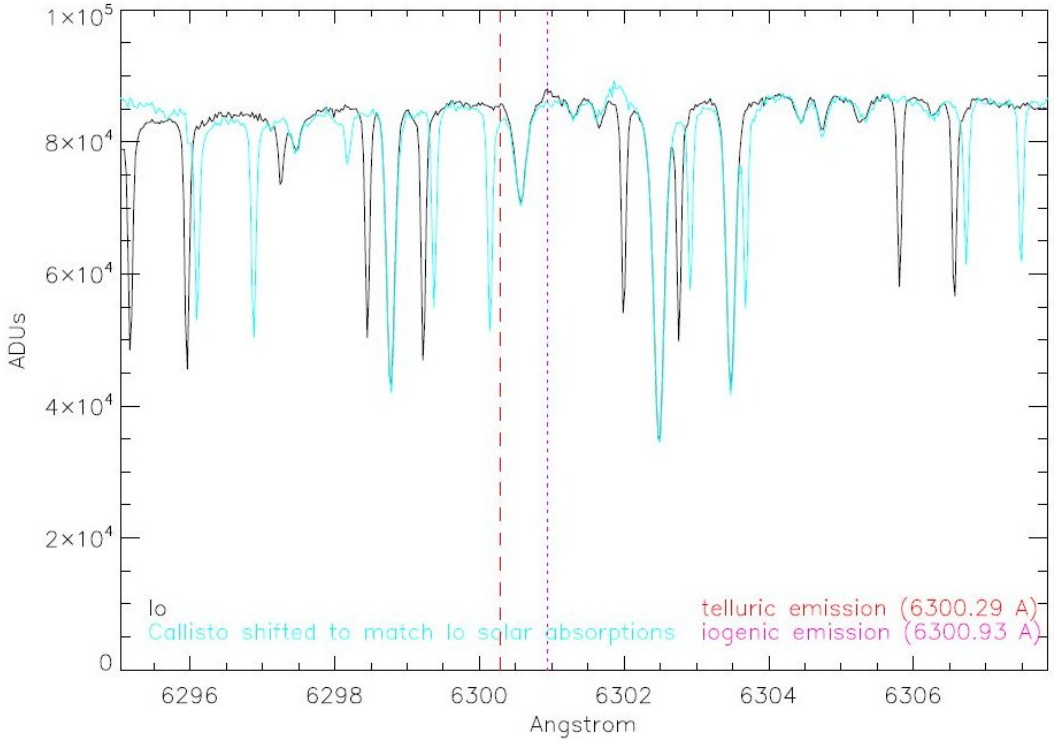

Figure 4.16: The spectral profile of Io (black) and Callisto (cyan) around the region of red line of atomic oxygen (OI, 6300.29 Å). The satellite has been shifted by the correct Doppler shift in order to match solar spectrum reflected at Io, and scaled to compare the two continua.

this would be the first time that atomic oxygen is observed both at the disk and in the corona. Oliversen et al. (2001) have seen it only at Io's disk, while other groups (e.g. Schneider et al. 2002) have observed it only away from Io's disk. Atomic oxygen emission is a key element to study the Io atmosphere-plasma torus interaction, since neutral oxygen, contrary to sodium, is a dominant component of Io's atmosphere. The relatively short lifetime ($\sim 130\,s$) of the $O(^1D)$ state menas that the emission is near its source of excitation, and therefore is a diagnostic of plasma conditions. A detailed analysis is currently performing in order to exclude that this is caused by artifacts.

As already stated, because of the difficulty of treating "non-standard" data, the reduction steps have just been accomplished. In the following months these data, together with the models that are currently developing, will provide us pre-

cious information on the extended exospheres of Io and Europa, on the nature of Europa's sodium, on the possible detection of atomic oxygen at Io and on the unexplained features that appeared at Io (both in absorption and in emission, at distinct Doppler shifts). Last but not least, given the multi-species detection capabilities, it is not excluded that in the future interesting "discoveries" will not occur.

4.3 The Moon

Our own natural satellite resembles in many aspects the planet Mercury, not only for the presence, at their surface, of similar craters, scarps, faults and for the fact that they are both geologically dead bodies, but also for the tenuous atmosphere, that shares many elements with the hermean one as well as the source and sink processes and the anti-sunward tail. Elements detected at the Moon are He, Na, K, in common with Mercury, and Ar. Hydrogen, instead, has not been detected in the lunar exosphere, probably because of its reduction on the surface. Column densities are 2 orders of magnitude lower than those for Mercury: $10^8 \div 10^9\, atoms\, cm^{-2}$ for Na and $10^7 \div 10^8\, atoms\, cm^2$ for K (Hunten & Sprague 1997). It is proved that the Moon has an exosphere spanning from 5 to 20 Moon Radii ($1R_{\leftmoon} = 1737\, km$). The first time that the anti-sunward sodium tail was detected was 20 years ago: Mendillo et al. (1991) obtained the first imaging observations

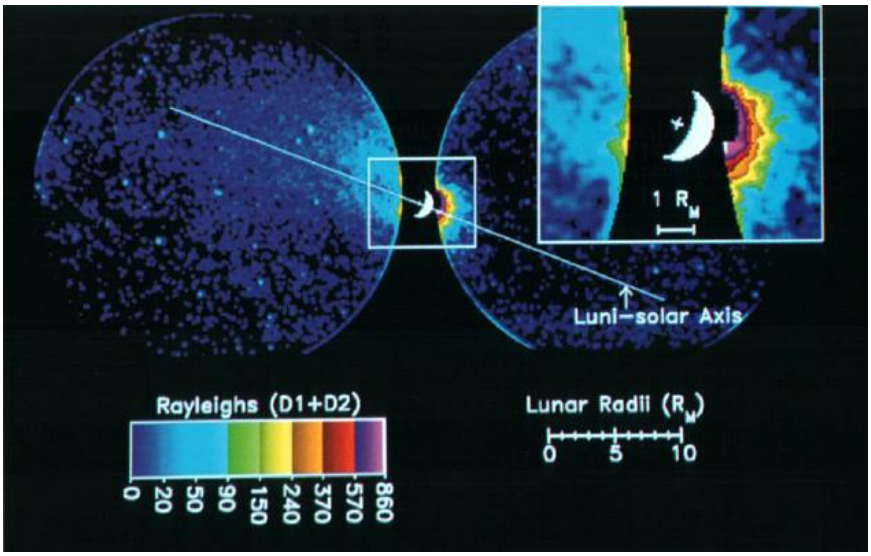

Figure 4.17: The anti-sunward sodium tail of the Moon.

of the extended lunar sodium atmosphere (see fig. 4.17), observing emission out to $\sim 5\, R_{\leftmoon}$ on the dayside, and out to $15 \div 20\, R_{\leftmoon}$ in a tail-like structure on the nightside. They qualitatively describe the morphology of the lunar sodium atmosphere much like that of a comet, with a bright coma centered on the Moon and an extended tail extending away in the antisunward direction. Wilson et al. (1999) showed that sodium tail extends until $230\, R_{\leftmoon}$, and it seemed correlated with the Leonid shower of November 1998. Matta et al. (2009) managed to track the tail even further, up to $440\, R_{\leftmoon}$, thanks to the position of the satellite, near

new Moon phases.

Many of the sources and sinks of sodium in lunar exosphere are in common with Mercury. Sources of sodium for lunar exosphere are thermal desorption, PSD, meteoric impact, charged particles sputtering. Losses of sodium are gravitational escape, SRP, photo-ionization with subsequent plasma pick-up by the solar wind. These atoms have sufficient energy to escape the weak gravity of the Moon and form a tail. At 1 AU, a sodium atom at rest relative to the Sun experiences an acceleration of $\sim 2.5\, cm\, s^{-2}$. For atoms in highly eccentric trajectories above the Moon, for example, this acceleration is sufficient to strip some of these atoms from the Moon's gravity field and start them on their way down the tail. For a few days around new moon phase, this lunar sodium tail can be imaged by ground-based observers as a small ($\sim$ 5 degrees diameter) patch of emission near the anti-sunward direction (Smith et al. 2001). Fabry-Perot methods report down-tail velocities averaging $12.4 km\, s^{-1}$ near the center of the tail (Mierkiewicz et al. 2006).

Employing a wide-angle imaging system, Wilson et al. (2003) observed the full coma of the lunar sodium exosphere (during a lunar eclipse) out to $\sim 20\, R_{\leftmoon}$, and used these observations to constrain the high-end speed distribution of lunar sodium exosphere source processes. Their model-data comparison indicate that $\sim 20\%$ of the escaping sodium atoms are ejected from the lunar surface with speeds greater than the lunar escape velocity ($2.4\, km\, s^{-1}$) and therefore, solar radiation pressure is largely responsible for most of the sodium escape into the Moon's outer exosphere and sodium tail. If there is no doubt on the role of the solar radiation pressure, on the source that emits these atoms to the tail there is still controversy. They are either solar wind sputtering or PDS. Concerning the former, observations proved contraddictory. In some instances the sodium levels appeared to be very low (Potter & Morgan 1994), while in other studies enhanced brightness was observed despite the presumed shielding of ions by the magnetosphere (Mendillo et al. 1999). Wilson et al. (2006) has observed Moon sodium exosphere to test the effect of **shielding** of lunar surface from the solar wind plasma by the Earth's magnetosphere. They found that the brightness of the lunar sodium exosphere at full Moon is correlated with the Moon's passage through the Earth's magnetotail plasma sheet. This suggests that omnipresent exospheric sources (sunlight or micrometeors) are augmented by variable plasma impact sources in the solar wind and Earth's magnetotail. Plasma sheet constituents impacting the lunar surface increase the rate of sodium outgassing from the lunar surface into the exosphere. They found that up to 15 hours after the plasma sheet passage, the exosphere is still significantly brighter than 30 hours later. This means that ion sputtering/electron desorption followed by *immediate* escape does not fully describe the effect of the plasma sheet.

A sodium transport modeling by Sarantos et al. (2010) showed that the primary

effect of ion impact on the surface of the Moon is not direct sputtering but rather an enhancement of the PSD efficiency. It is inferred that the ion-induced effects must double the PSD efficiency for flux typical of the solar wind at 1 AU. The enhancement in relative efficiency of PSD due to the bombardment of the lunar surface by the plasma sheet ions during passages through the Earth's magnetotail is shown to be approximately two times higher than when it is due to solar wind ions. This leads to the conclusion that the ion-enhanced diffusion (or *priming* of the surface) is more efficiently carried out by the energetic plasma sheet ions during certain phases of the lunar orbit.

Finally, to test the effect of micro-meteoroid impact vaporization, Wilson et al. (1999) performed observations two days after the peak of the Leonid shower. These observations indicate that the lunar spot was enhanced by as much as a factor of five during the meteor storm, presumably due to micro-meteor impacts on the Moon which led to an increase in the lunar sodium escape flux. Subsequent observations Smith et al. (2001) indicate that this feature is a regular occurrence in the night sky near the time of new Moon, with a maximum brightness ($D_1 + D_2$) between 15 and 90 Rayleighs. Micro-meteoritic impact vaporization is considered to contribute to the exosphere even less than sputtering but will important on the night side of the Moon because of the absence of other processes.

Recently, Kagitani et al. (2010) measured brightness of lunar sodium exosphere with lunar orbiter SELENE (Kaguya). Variations in line-of-sight integrated intensity measured on the night-side hemisphere of the Moon could be described as a spherical symmetric distribution of the sodium exosphere with a temperature of 2400-6000K. A clear variation in surface density related to the Moon's passage across the Earth's magnetotail could not be seen, although sodium density gradually decreased (by $20 \pm 8\%$) during periods from the first through the last quarter of two lunar cycles. These results suggest that the supra-thermal components of the sodium exosphere are not mainly produced by classical sputtering of solar wind. The variation in sodium density (which depends on lunar-phase angle) is possibly explained by the presence of an inhomogeneous source distribution of photon-stimulated desorption(PSD) on the surface.

4.3.1 The observations of Rosetta spacecraft

Rosetta spacecraft flew by the Earth-Moon system three times (March 2005, November 2007 and November 2009) during its journey to the comet 67P/Churyumov-Gerasimenko. We wanted to use the images taken with the WAC camera of OSIRIS instrument, equipped with the sodium filter, in order to test the capability of this instrument in view of the then forthcoming flyby with asteroid Lutetia, on July 2010. Given that the Moon's exosphere brightness is pretty well known, it could have permitted to us to assess the exposures times for the same instrument when

the asteroid would have been reached, and possibly to further study the Moon's exosphere.

Unfortunately, before we tried to calibrate the Moon spectra, it was clear that ghosts in the images were too big, and this prevented any further image analysis. See fig. 4.18.

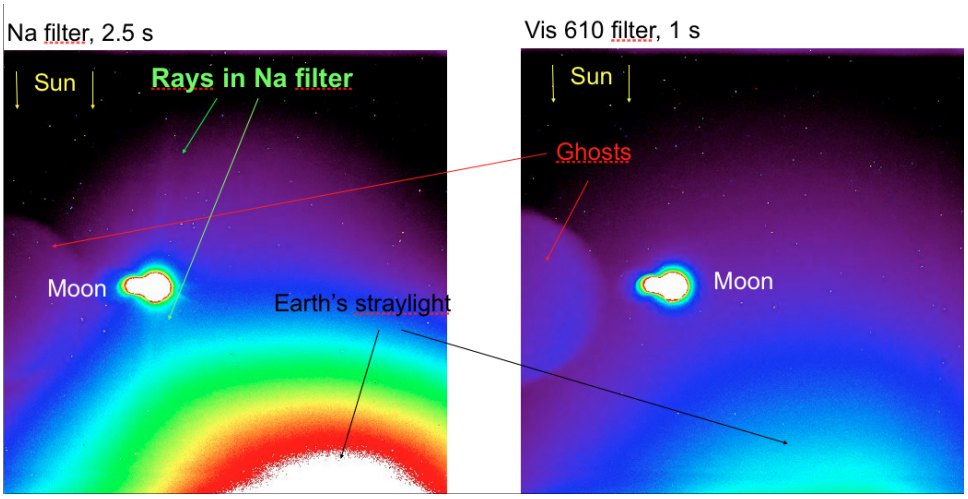

Figure 4.18: Images taken with the WAC, Na-filtered (left, exposure time 2.5 s) and Vis610-filtered (right, exposure time 1 s). Ghosts and diffuse straylight are present in both images. Diffraction rays are visible in the Na-filtered image.

Just to try, I calibrated the subtraction Na-Vis610 in order to check qualitatively the amount of diffuse straylight. The result is reported in fig. 4.19(a). Counts are far greater than those reported in literature - see 4.19(b), from Wilson et al. (2006).

As for Lutetia, images will be re-considered once the team devoted to subtraction of diffuse straylight will manage to properly correct for this severe problem.

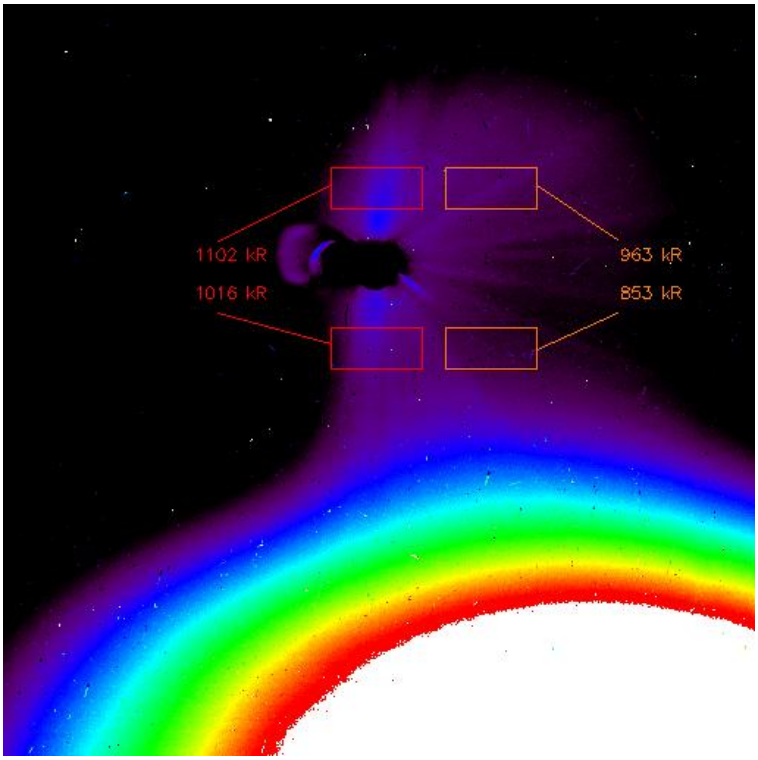

(a)

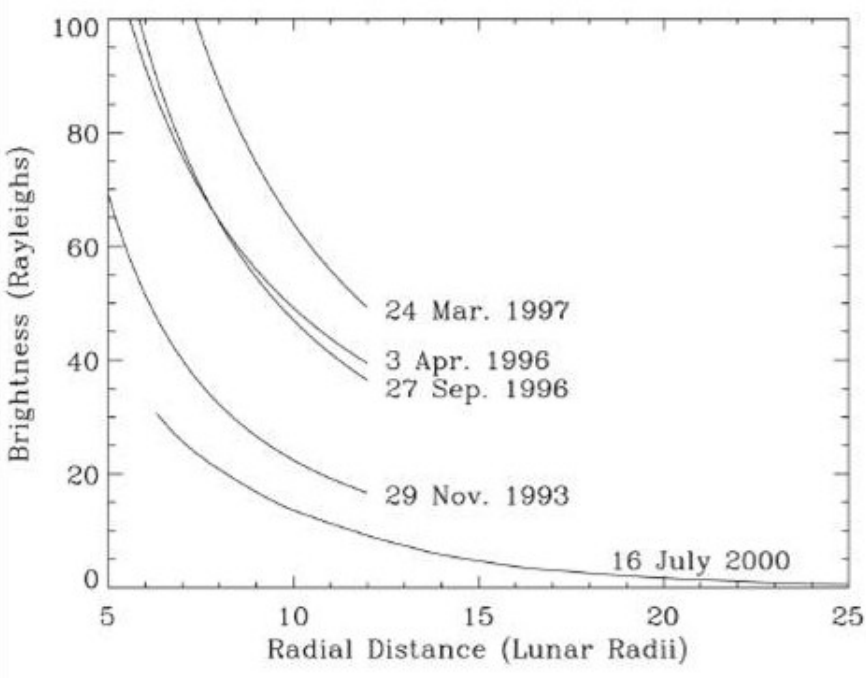

(b)

Figure 4.19: Top: subtraction Na-Vis610 calibrated in Rayleighs. The Sun is directed upwards. Counts (expressed in kiloRayleighs) are reported as mean over the box region. They are far greater than those reported in literature. Moreover, they are slightly higher in the sunward direction, contrary to the expected. Bottom: Reported observations of the brightness of the lunar exosphere.

5

General Conclusions

During my three-years PhD I've studied different kind of exospheres: surface-bounded and interacting with the planetary magnetic field (Mercury) or with Jupiter's magnetosphere (Europa), surface-bounded and interacting with only the solar wind (Lutetia), atmosphere-bounded and interacting with an external magnetosphere (Io). I used different approaches, both observational and theoretical.

Concerning Io, I contributed to study the role of the optically thick atmosphere of Io plays in the supply and transport of sodium atoms to the optically thin exosphere, through the variation of brightness with the orbital longitude observed with Telescopio Nazionale Galileo (TNG). The work I carried on revelead a behavior of the post-eclipse neutral cloud that is inconsistent with constant column density. This in turn reveals that condensation of Io atmosphere takes places during the 2.5-hours-long eclipse behind Jupiter's shadow, preventing sodium-bearing molecules such as $NaCl$ to be released. And this is the first time that a similar behaviour is clearly observed. During this work, new, intriguing, exospheric emissions and absorption have been discovered where they weren't expected. They are present both at Io's disk (in absorption) and at the neutral cloud (in emission) at slightly different Doppler shifts and thus velocities. The nature of these features seems to suggest some radiative transfer process that is not clearly understood. A detailed modeling has already started, and new observations will be required.

Concerning Mercury, the data that I have treated proved decisive to show a southern enhancement of sodium brightness which is related to the sign of the B_x component of the interplanetary magnetic field. This strongly supports the hypothesis that sudden increases in the sodium brightness are related to an enhanced ion flux at areas at the surface where these are open to solar wind ion sputtering through the magnetospheric cusps.

I have also started a modelization of Mercury's anti-sunward sodium tail, since no complete models have been developed so far after its discovery nearly 10 years ago, and there is a need to explain the observations. I managed to develope a

Fortran code, which uses a 4th order Runge-Kutta algorithm to follow the trajectory of test particles ejected from the planetary surface and that experience only Mercury's gravity and solar radiation pressure. A first result is that thermal desorption and photon-stimulated desorption are not great contributors to the tail. This confirms what suspected by the "hermean community", i.e. that the majority of atoms are emitted by solar wind sputtering. Concerning the spatial distribution of the sodium tail, the model matched quite well the trend of the observed column densities up to 16 Mercury Radii, although some small adjustment is required in order to lower by 1 order of magnitude the column densities. The problem arises during the conversion from number density. If so, it won't take much time before it will be fixed. Once this model will be completed, it will permit to compare observed intensities (obtained from column density by multiplying this latter for the g-factor, since Mercury's sodium tail is optically thin) and to infer to which extent each emission process contributes to the escaping tail.

I also developed a model to estimate, for the first time, the intensity of Lutetia's brightness, in view of the then forthcoming fly-by of Rosetta spacecraft. This predicted a brightness of 2 orders of magnitudes lower than that of the Moon. A comparison with observations of WAC-OSIRIS instrument onboard Rosetta will be possibile once the problems due to the diffuse straylight and ghosts will be fixed by the responsible Osiris Team. Images of the Earth-Moon system have also been taken by the same instruments of Rosetta spacecraft during three flybys. I tried to use these data in order to have an estimate of the exposure times for the then forthcoming fly-by of Lutetia, and to possibly study Moon's exosphere. However, the problems related to the diffuse straylight and ghost images were accordingly worst, due to the extra brightness of the Moon compared to Lutetia. I tried to remove the continuum from Na-filter images, but a calibration were not possibile.

Finally, I observed Jupiter's Medicean moons a second time, in order to both further investigate the unexpected features discovered at Io and to study variation with orbital position of Io and Europa. During this second run at TNG, observations have been carried in a non-standard mode, allowing simulaneous detection of several species. For this reason, the reduction steps were more complex and have been just finished. However, the preliminary results seem to confirm that sodium at Europa is endogenic and not brought there by Io, and this would solve a controversy born since the discovery of sodium at Europa 15 years ago. These observations have shown the intensity of sodium at Io and Europa to vary up to a factor of 5 in the orbital longitude, suggesting the presence of "seasons". New, unexpected features were present also this time, with a different Doppler shift. A possible detection of atomic oxygen needs to be further investigated. If confirmed, this would be the first time that this emission if found both at Io's disk and away from it.

the broader topic of planetary atmospheres, are essential in understanding the formation of the Solar System and not only, since exospheres have been discovered also in exoplanets. After all, this is also a study on the formation of the life on Earth.

Bibliography

Barbieri, C., Verani, S., Cremonese, G., et al. 2004, Planet. Space Sci., 52, 1169

Barucci, M. A., Fulchignoni, M., Fornasier, S., et al. 2005, A&A, 430, 313

Baumgardner, J., Wilson, J., & Mendillo, M. 2008, Geophys. Res. Lett., 35, 3201

Bevington, P. R. & Robinson, D. K. 2003, Data reduction and error analysis for the physical sciences, ed. Bevington, P. R. & Robinson, D. K.

Bigg, E. K. 1964, Nature, 203, 1008

Binder, A. B. & Cruikshank, D. P. 1964, Icarus, 3, 299

Birlan, M., Barucci, M. A., Vernazza, P., et al. 2004, New A, 9, 343

Brown, M. E. 2001, Icarus, 151, 190

Brown, M. E. & Hill, R. E. 1996, Nature, 380, 229

Brown, R. 1974a, New Scientist, 64, 484

Brown, R. A. 1974b, in IAU Symposium, Vol. 65, Exploration of the Planetary System, ed. A. Woszczyk & C. Iwaniszewska, 527–531

Brown, R. A. & Yung, Y. L. 1976, in IAU Colloq. 30: Jupiter: Studies of the Interior, Atmosp here, Magnetosphere and Satellites, ed. T. Gehrels, 1102–1145

Burbine, T. H. & Binzel, R. P. 2002, Icarus, 159, 468

Burger, M. H., Schneider, N. M., & Wilson, J. K. 1999, Geophys. Res. Lett., 26, 3333

Butler, B. J. 1997, J. Geophys. Res., 102, 19283

Carlson, R. W., Johnson, R. E., & Anderson, M. S. 1999, Science, 286, 97

Chamberlain, J. W. & Hunten, D. M. 1987, Theory of planetary atmospheres. An introduction to their physics andchemistry., ed. Chamberlain, J. W. & Hunten, D. M.

Chapman, S. 1960, in Physics of the Upper Atmosphere, ed. J. A. Ratcliffe, 1–+

Cintala, M. J. 1992, J. Geophys. Res., 97, 947

Cipriani, F., Leblanc, F., Witasse, O., & Johnson, R. E. 2008, Geophys. Res. Lett., 35, L19201

Cremonese, G., Boehnhardt, H., Crovisier, J., et al. 1997, ApJ, 490, L199+

Cruikshank, D. P., Emery, J. P., Kornei, K. A., Bellucci, G., & D'Aversa, E. 2010, Icarus, 205, 516

Dessler, A. J. 1980, Icarus, 44, 291

Divine, N. 1993, J. Geophys. Res., 98, 17029

Eichhorn, G. 1978, Planet. Space Sci., 26, 463

Feldman, P. D., Strobel, D. F., Moos, H. W., et al. 2000, Geophys. Res. Lett., 27, 1787

Fox, J. L. 1993, J. Geophys. Res., 98, 3297

Fox, J. L. & Bakalian, F. M. 2001, J. Geophys. Res., 106, 28785

Fox, J. L. & Dalgarno, A. 1983, J. Geophys. Res., 88, 9027

Frank, L. A., Paterson, W. R., Ackerson, K. L., et al. 1996, Science, 274, 394

Goldberg, B. A., Garneau, G. W., & Lavoie, S. K. 1984, Science, 226, 512

Goldstein, R. M. 1970, Science, 168, 467

Grava, C., Schneider, N. M., & Barbieri, C. 2010, in IAU Symposium, Vol. 269, IAU Symposium, 224–228

Hapke, B. 1993, Theory of reflectance and emittance spectroscopy, ed. B. Hapke

Harmon, J. K. & Slade, M. A. 1992, Science, 258, 640

Hinson, D. P., Kliore, A. J., Flasar, F. M., et al. 1998, J. Geophys. Res., 103, 29343

Hodges, R. R. 1980, J. Geophys. Res., 85, 164

Holmlid, L. 2006, Planet. Space Sci., 54, 101

Huebner, W. F., Keady, J. J., & Lyon, S. P. 1992, Ap&SS, 195, 1

Hunten, D. M., Shemansky, D. E., & Morgan, T. H. 1988, The Mercury atmosphere, ed. Vilas, F., Chapman, C. R., & Matthews, M. S., 562–612

Hunten, D. M. & Sprague, A. L. 1997, Advances in Space Research, 19, 1551

Hunten, D. M. & Sprague, A. L. 2002, Meteoritics and Planetary Science, 37, 1191

Ip, W. 1986, Geophys. Res. Lett., 13, 423

Ip, W.-H. 1990, ApJ, 356, 675

Johnson, R. E. 1994, Icarus, 111, 65

Johnson, R. E., Combi, M. R., Fox, J. L., et al. 2008, Space Sci. Rev., 139, 355

Johnson, R. E., Killen, R. M., Waite, J. H., & Lewis, W. S. 1998, Geophys. Res. Lett., 25, 3257

Johnson, R. E., Leblanc, F., Yakshinskiy, B. V., & Madey, T. E. 2002, Icarus, 156, 136

Kagitani, M., Taguchi, M., Yamazaki, A., et al. 2010, Planet. Space Sci., 58, 1660

Killen, R., Cremonese, G., Lammer, H., et al. 2007, Space Sci. Rev., 132, 433

Killen, R. M. & Ip, W.-H. 1999, Reviews of Geophysics, 37, 361

Killen, R. M., Potter, A. E., Reiff, P., et al. 2001, J. Geophys. Res., 106, 20509

Killen, R. M., Sarantos, M., Potter, A. E., & Reiff, P. 2004a, Icarus, 171, 1

Killen, R. M., Sarantos, M., & Reiff, P. H. 2004b, Advances in Space Research, 33, 1899

Kliore, A. J., Fjeldbo, G., Seidel, B. L., et al. 1975, Icarus, 24, 407

Küppers, M. & Schneider, N. M. 2000, Geophys. Res. Lett., 27, 513

Lammer, H., Wurz, P., Patel, M. R., et al. 2003, Icarus, 166, 238

Leblanc, F., Doressoundiram, A., Schneider, N., et al. 2008, Geophys. Res. Lett., 35, L18204

Leblanc, F., Doressoundiram, A., Schneider, N., et al. 2009, Geophys. Res. Lett., 36, 7201

Leblanc, F. & Johnson, R. E. 2003, Icarus, 164, 261

Leblanc, F. & Johnson, R. E. 2010, Icarus, 209, 280

Leblanc, F., Potter, A. E., Killen, R. M., & Johnson, R. E. 2005, Icarus, 178, 367

Lellouch, E. 1996, Icarus, 124, 1

Macy, Jr., W. & Trafton, L. 1975, ApJ, 200, 510

Madey, T. E., Yakshinskiy, B. V., Ageev, V. N., & Johnson, R. E. 1998, J. Geophys. Res., 103, 5873

Mangano, V., Leblanc, F., Barbieri, C., et al. 2009, Icarus, 201, 424

Massetti, S., Orsini, S., Milillo, A., et al. 2003, Icarus, 166, 229

Matson, D. L., Goldberg, B. A., Johnson, T. V., & Carlson, R. W. 1978, Science, 199, 531

Matta, M., Smith, S., Baumgardner, J., et al. 2009, Icarus, 204, 409

McElroy, M. B., Kong, T. Y., & Yung, Y. L. 1977, J. Geophys. Res., 82, 4379

McGrath, M. A., Johnson, R. E., & Lanzerotti, L. J. 1986, Nature, 323, 694

Mendillo, M., Baumgardner, J., & Flynn, B. 1991, Geophys. Res. Lett., 18, 2097

Mendillo, M., Baumgardner, J., Flynn, B., & Hughes, W. J. 1990, Nature, 348, 312

Mendillo, M., Baumgardner, J., & Wilson, J. 1999, Icarus, 137, 13

Mierkiewicz, E. J., Line, M., Roesler, F. L., & Oliversen, R. J. 2006, Geophys. Res. Lett., 33, 20106

Morgan, T. H. & Killen, R. M. 1997, Planet. Space Sci., 45, 81

Morgan, T. H., Potter, A. E., Corliss, J. B., et al. 2004, in Bulletin of the American Astronomical Society, Vol. 36, AAS/Division for Planetary Sciences Meeting Abstracts #36, 1099–+

Moses, J. I., Zolotov, M. Y., & Fegley, Jr., B. 2000, in Bulletin of the American Astronomical Society, Vol. 32, AAS/Division for Planetary Sciences Meeting Abstracts #32, 1057–+

Mueller, M., Harris, A. W., Bus, S. J., et al. 2006, A&A, 447, 1153

Mura, A., Orsini, S., Milillo, A., et al. 2005, Icarus, 175, 305

Oliversen, R. J., Scherb, F., Smyth, W. H., et al. 2001, J. Geophys. Res., 106, 26183

Paranicas, C., Carlson, R. W., & Johnson, R. E. 2001, Geophys. Res. Lett., 28, 673

Pearl, J., Hanel, R., Kunde, V., et al. 1979, Nature, 280, 755

Potter, A. E. 1995, Geophys. Res. Lett., 22, 3289

Potter, A. E., Killen, R. M., & Morgan, T. H. 1999, Planet. Space Sci., 47, 1441

Potter, A. E., Killen, R. M., & Morgan, T. H. 2000, J. Geophys. Res., 105, 15073

Potter, A. E., Killen, R. M., & Morgan, T. H. 2002, Meteoritics and Planetary Science, 37, 1165

Potter, A. E., Killen, R. M., & Morgan, T. H. 2007, Icarus, 186, 571

Potter, A. E., Killen, R. M., & Sarantos, M. 2006, Icarus, 181, 1

Potter, A. E. & Morgan, T. H. 1990, Science, 248, 835

Potter, A. E. & Morgan, T. H. 1994, Geophys. Res. Lett., 21, 2263

Press, W., Teukolsky, S., Vetterling, W., & Flannery, B. 2007, Numerical Recipes, 3rd edn. (Cambridge)

Retherford, K. D. 2003, PhD thesis, THE JOHNS HOPKINS UNIVERSITY

Retherford, K. D., Moos, H. W., Strobel, D. F., Wolven, B. C., & Roesler, F. L. 2000, J. Geophys. Res., 105, 27157

Sarantos, M., Killen, R. M., Surjalal Sharma, A., & Slavin, J. A. 2010, Icarus, 205, 364

Saur, J., Neubauer, F. M., Connerney, J. E. P., Zarka, P., & Kivelson, M. G. 2004, Plasma interaction of Io with its plasma torus, ed. Bagenal, F., Dowling, T. E., & McKinnon, W. B., 537–560

Schläppi, B., Altwegg, K., & Wurz, P. 2008, Icarus, 195, 674

Schleicher, H., Wiedemann, G., Wöhl, H., Berkefeld, T., & Soltau, D. 2004, A&A, 425, 1119

Schneider, N. M. & Bagenal, F. 2007, Io's neutral clouds, plasma torus, and magnetospheric interaction (Springer Praxis Books / Geophysical Sciences), 265–286

Schneider, N. M., Burger, M. H., & Thomas, N. 2002, in Bulletin of the American Astronomical Society, Vol. 34, AAS/Division for Planetary Sciences Meeting Abstracts #34, 913–+

Schneider, N. M., Grava, C., & Barbieri, C. 2008, in Bulletin of the American Astronomical Society, Vol. 40, AAS/Division for Planetary Sciences Meeting Abstracts #40, 507–+

Schneider, N. M., Hunten, D. M., Wells, W. K., Schultz, A. B., & Fink, U. 1991a, ApJ, 368, 298

Schneider, N. M., Leblanc, F., Grava, C., et al. 2010, in Bulletin of the American Astronomical Society, Vol. 42, Bulletin of the American Astronomical Society, 1026–+

Schneider, N. M., Wilson, J. K., Trauger, J. T., et al. 1991b, Science, 253, 1394

Sigmund, P. 1969, Physical Review, 184, 383

Smith, S. M., Mendillo, M., Wilson, J. K., & Baumgardner, J. 2001, Advances in Space Research, 27, 1181

Smyth, W. H. 1986, Nature, 323, 696

Smyth, W. H. 1992, Advances in Space Research, 12, 337

Smyth, W. H. & Combi, M. R. 1988, ApJ, 328, 888

Smyth, W. H. & Marconi, M. L. 1995, ApJ, 441, 839

Spencer, J. R. & Schneider, N. M. 1996, Annual Review of Earth and Planetary Sciences, 24, 125

Sprague, A. L., Kozlowski, R. W. H., Hunten, D. M., et al. 1997, Icarus, 129, 506

Sprague, A. L., Schmitt, W. J., & Hill, R. E. 1998, Icarus, 136, 60

Starukhina, L. V. 2000, in Lunar and Planetary Institute Science Conference Abstracts, Vol. 31, Lunar and Planetary Institute Science Conference Abstracts, 1301–+

Strobel, D. F. 2002, Aeronomic Systems on Planets, Moons, and Comets, ed. Mendillo, M., Nagy, A., & Waite, J. H., 7–+

Thomas, N., Bagenal, F., Hill, T. W., & Wilson, J. K. 2004, The Io neutral clouds and plasma torus, ed. Bagenal, F., Dowling, T. E., & McKinnon, W. B., 561–591

Trafton, L. 1975, Nature, 258, 690

Trafton, L., Parkinson, T., & Macy, Jr., W. 1974, ApJ, 190, L85+

Wiens, R. C., Burnett, D. S., Calaway, W. F., et al. 1997, Icarus, 128, 386

Wilson, J. K., Baumgardner, J., & Mendillo, M. 2003, Geophys. Res. Lett., 30, 1649

Wilson, J. K., Mendillo, M., Baumgardner, J., et al. 2002, Icarus, 157, 476

Wilson, J. K., Mendillo, M., & Spence, H. E. 2006, Journal of Geophysical Research (Space Physics), 111, 7207

Wilson, J. K. & Schneider, N. M. 1994, Icarus, 111, 31

Wilson, J. K., Smith, S. M., Baumgardner, J., & Mendillo, M. 1999, Geophys. Res. Lett., 26, 1645

Wurz, P. & Lammer, H. 2003, Icarus, 164, 1

Yakshinskiy, B. V. & Madey, T. E. 1999, Nature, 400, 642

Yakshinskiy, B. V. & Madey, T. E. 2000, Surface Science, 451, 160

Yakshinskiy, B. V. & Madey, T. E. 2001, J. Geophys. Res., 106, 33303

Yakshinskiy, B. V. & Madey, T. E. 2004, Icarus, 168, 53

Zolotov, M. Y. & Shock, E. L. 2001, J. Geophys. Res., 106, 32815

Ringraziamenti

Desidero qui ringraziare tutti coloro che hanno contribuito in un modo o nell'altro nella stesura di questa tesi.

Innanzitutto, il Prof. Cesare Barbieri, senza il quale non avrei potuto intraprendere questo percorso. A lui va il mio più sincero ringraziamento per avermi introdotto all'affascinante mondo delle atmosfere planetarie. Desidero ringraziare il mio supervisore esterno e amico Nick Schneider, per il suo costante supporto a questa tesi e per avermi insegnato ad usare uno sguardo critico per affrontare i problemi, non solo di tipo astronomico, e per avermi dato la possibilità di passare sei mesi del mio dottorato a Boulder, Colorado.

Desidero inoltre ringraziare François Leblanc per i consigli su come sviluppare un modello in Fortran, Gabriele Mainetti per avermi risolto innumerevoli piccoli e grandi problemi di informatica e non solo, permettendomi di risparmiare molto tempo, Valeria Mangano per l'aiuto che mi ha fornito specialmente durante la prima parte di questo dottorato, ed Umberto Buonomo per avermi introdotto al metodo di parallelizzazione Openmp .

Desidero infine ringraziare Amarilli, alla quale questa tesi è dedicata, per essermi stata vicina sopportandone il peso insieme a me per ben tre anni e per avermi aiutato in tutto. Grazie di cuore.